Controllable Transformation Matching Networks for Efficient RF Impedance Matching

by

Khandoker N. Rafa Islam

Submitted to the Department of Electrical Engineering and Computer Science
in partial fulfillment of the requirements for the degree of

MASTER OF SCIENCE

at the

MASSACHUSETTS INSTITUTE OF TECHNOLOGY

February 2024

Authored by: Khandoker N. Rafa Islam
Department of Electrical Engineering and Computer Science
January 24, 2024

Certified by: David J. Perreault
Ford Professor of Electrical Engineering, Thesis Supervisor

Accepted by: Leslie A. Kolodziejski
Professor of Electrical Engineering and Computer Science
Department Committee on Graduate Students

Controllable Transformation Matching Networks for Efficient RF Impedance Matching

by

Khandoker Nuzhat Rafa Islam

Submitted to the Department of Electrical Engineering and Computer Science
on January 24, 2024, in partial fulfillment of the
requirements for the degree of
Master of Science in Electrical Engineering and Computer Science

Abstract

Efficient and controlled delivery of radio-frequency (rf) power for semiconductor plasma processing typically relies upon tunable matching networks to transform the variable plasma load impedance to a fixed impedance suitable for most rf power amplifiers. Plasma applications require fast tuning speed with precise control from the matching networks while operating at a high frequency range. However, it is difficult to meet the requirements for many semiconductor plasma applications with conventional impedance matching solutions due to their limited response speeds. This slow speed comes from the presence of mechanical components in the matching network, since they can be tuned only mechanically. This work introduces a novel controllable transformation matching network (CTMN) intended to address the need for high-speed, tunable impedance matching.

The design of the CTMN employs a two-port controllable switching network coupled with a high-Q passive network, enabling rapid voltage modulation and dynamic reactance tuning (dynamic frequency tuning) to swiftly accommodate both resistive and reactive load variations. Control strategies are introduced to maintain zero-voltage switching as needed to minimize switching losses. This approach is substantiated through simulations, which indicate the CTMN's capability to achieve precise impedance matching with the potential for substantially faster response times (in the μ s range) than traditional systems. It is anticipated that the proposed approach will enable ultra-fast, high-efficiency tunable impedance matching to address the needs of modern plasma systems.

Thesis Supervisor: David J. Perreault
Title: Ford Professor of Electrical Engineering

Acknowledgments

Reflecting on my master's journey at MIT, these past two years have been indescribable. Even today, I remain amazed to be a part of this incredible community. My heartfelt appreciation to everyone who has contributed to enriching both my academic and personal life.

I am deeply grateful to my advisor, Prof. David Perreault, for welcoming me into MIT and profoundly influencing both my professional and personal growth. Your extensive knowledge in electrical engineering and supportive mentorship have been my biggest sources of encouragement during this transformative chapter of my life. Thank you for the invaluable experiences that encouraged me to choose challenges as learning opportunities and instilled confidence in me.

I want to thank my academic advisor, Leslie Kolodziejski, for being the kindest, most supportive, and most authentic mentor. Your words, 'Rafa, remember, even if this is the first pivot in your life, it is not going to be the last,' have truly kept me going many times. Chris Featherman and Deanna Montgomery, your insights into the 'non-typical' process of my technical writing and how to streamline it have been invaluable. My gratitude extends to Di Ye for all the career and academic advice and to Amit Sinha for the MIT Presidential Fellowship that supported me in my first year.

To the LEEs community (forgive me if I haven't mentioned you here; you know how forgetful I am) : Tommy, Dan, Aaron, Amanda, Julia, Mansi, Rachel, Mohamed, Xin, Mihir, Dave Otten, Daisy, Elaine, Josh, Tony, Mario, Ahmad, Yiou, Mathhew, and Rod, your friendship and collaboration have deeply affected my experience in the lab. Quang, thank you for your unwavering support, even during last-minute crunches. I'm particularly grateful to Alex Jurkov and Jessica Boles for their invaluable mentorship and friendship. Jessica, thanks for the research discussions within the lab and out on the highway. And Alex, thank you for tolerating my relentless questions the moment you are back in the lab.

The past year was extremely challenging, particularly with getting COVID three times. But I am healthy and sound, thanks to my caring 'apus'- Munni, Shathi, Xisan, and Faria, among many others. I am also lucky to have the 'baby' stress relievers : Chingyu, Abeeda, and Gullu-Pullu. My friends Aparna, Mohamed Amin, Ikra, Raph, Laurie have been very supportive from day one. Oh, and the most thanks go to my decade-long best friends, Shuprova, Ibnat, and Mrittika, for their unconditional support.

A special tribute to the iron lady of my life, my mother, who instilled in me the values of persistence, patience, and the pursuit of education. Then there's the 'N-series'—my 5 sisters: Nice, Namera, Nupur, Nipun, and Nayani, and my only brother, Life. Thank you for the compromises and support from you all.

This thesis is dedicated to my father, whose memories are scarce but whose influence remains profound.

Lastly, all praise is due to God for the blessings and opportunities bestowed upon me.

بسم الله الرحمن الرحيم

وَقُل رَب زِدْنِي عِلْمًا

And say,'My Lord, increase me in knowledge.'

Quran [20:114]

Contents

List of Figures

List of Tables

Chapter 1

Introduction

Efficient radio-frequency (rf) power delivery is fundamental to a wide range of applications. These range from wireless power transfer (WPT) [1–3] and radar communication systems [4] to medical devices such as MRI [5, 6], rf induction heating [7], semiconductor manufacturing, among others. These applications present a range of requirements for power generation systems, including but not limited to limitations on power, frequency, and load impedance range.

The combination of power level and efficiency requirements, often alongside the need for adaptability to variable load characteristics, presents significant challenges in efficient rf power generation and delivery. Advances in industrial applications such as rf plasma drives for semiconductor processing are posing increased challenges in terms of load impedance variations. This, in turn, makes achieving efficient power delivery more challenging in these applications. In this chapter, we will review the challenges of rf power amplifiers (PAs) to handle variable loads, motivating the need for new impedance matching techniques to overcome these challenges.

1.1 Challenges of RF PAs

A significant challenge with traditional PAs in applications with variable load impedances is that they are primarily designed to deliver power into nearly-fixed impedances (typically $50\,\Omega$ resistive termination for industry applications) [8–14]. The load impedance requirement is typically closely linked to the design of a power amplifier. When the load impedance deviates from the design specifications, it can induce increased voltage and current stresses on the devices of the PA, elevate system losses, and incur device failures due to exceeding safe voltage or current limits. Loading rf PAs with impedances outside their designed load range can also lead to waveform distortion, inefficient delivery of rf power [15, 16] and a lack of control over the delivered power.

1.2 Load Variation Handling Methods

There are multiple strategies to handle rf load variations between an rf source and an rf load. One approach is to seek to design an rf power source (i.e., a power amplifier) that directly drives a variable load impedance. Other approaches focus on modifying the rf load structure to achieve an acceptable variation in the load impedance range. Perhaps the most commonly used approach is inserting an intermediate circuit stage called a tunable matching network between the rf PA and rf load. We summarize each of these approaches below.

1.2.1 Variable Load Inverters

One approach to driving dynamically-varying load impedances is known as a variable load inverter (VLI). This is a switched-mode power amplifier (or rf inverter) that is designed to operate for a range of load impedances [17–20]. One class of approaches towards this, as illustrated in [18, 21], involves using interactions among multiple high-frequency inverters to compensate for a variable load impedance. Zero-voltage switching (ZVS) is maintained across a wide variety of load impedances by controlling the amplitudes and phases of the high-frequency inverters. A limitation of this general approach is the relatively large rating (kVA) of an inverter to drive a wide load impedance range, especially for large variations in load reactance. Another, more recent approach [19] uses a single inverter structure, providing additional degrees of control freedom to handle variations in load impedance. This approach is promising but has yet to be fully validated in hardware.

While such technologies have significant potential, the higher peak voltages and current stresses on a variable-load inverter are a challenge. For applications that require both high output power levels and a broad range of load impedances, this method may fall short [16].

1.2.2 Resistance Compression Networks

Load structural transformation networks have the capability to alter load configurations in order to guarantee an rf amplifier's impedance to be almost constant for particular applications. By compressing numerous numbers of varying load impedances into a more constrained range, resistance compression networks (RCNs) ensure that the impedances meet the loading criteria of the power amplifier [22–24]. However, this method has limited ability to deal with reactive load variation and requires a setup with a pair of matched (but variable) load impedances. Consequently, while it has been utilized in applications such as rf plasma-drive systems [25], it is perhaps better suited to applications such as dc-dc conversion.

1.2.3 Non-Reciprocal Component Networks

To ensure a constant load impedance for the power amplifier, non-reciprocal components, such as circulators or isolators, can be used with the PAs. An example isolator can be implemented by connecting a suitable isolation resistor to a circulator, which prevents unwanted power reflection back to the PA even when the rf output changes [26, 27]. However, if the rf load impedance fluctuates too much, considerable power loss can occur in the isolation resistor, resulting in poor efficiencies [27]. Moreover, because power from the amplifier is delivered to the isolation resistor instead of the load, this approach does not provide the ability to efficiently control power to the load.

1.2.4 Tunable Matching Networks

Perhaps the most effective approach to managing variations in load impedance is to use a tunable matching network (TMN) to transform the varying load impedance to a fixed value, as seen by the inverter or power amplifier. This is typically accomplished by using a reactive matching network between the PA and the load, where the reactive components used to realize impedance matching may be dynamically adjusted based on the value of the load impedance [28–34]. A standard rf power system that utilizes this approach is illustrated in

Fig. 1-1. It typically includes an rf power source, often a power amplifier (or an rf inverter), and a load (e.g., rf plasma load) that consumes the generated rf power. This approach is By appropriately choosing the values of the reactive elements, the impedance seen by the PA appears constant (e.g., at 50 Ω). TMNs offer considerable advantages, enhancing

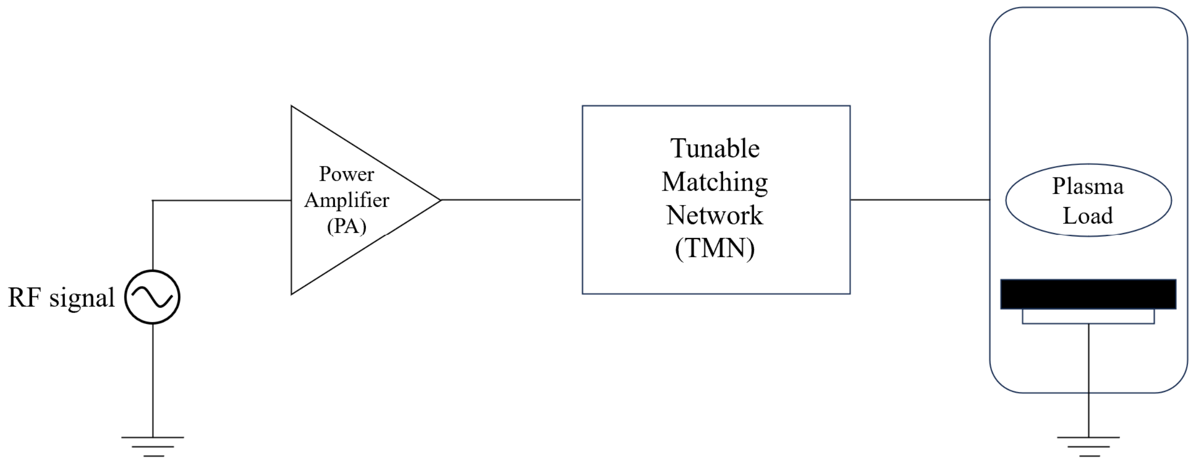

Figure 1-1: A high-level block diagram of a standard rf power generation and delivery system. It includes a tunable matching network (TMN) placed between a power amplifier (PA) and a plasma load. The TMN is used to match the variable impedance of the plasma load to a fixed impedance value preferred by the PA.

the adaptability and implementation of PAs in rf systems. Utilizing a TMN with a linear amplifier, such as Class A, AB, B, etc., facilitates genuine impedance matching between the source and the load, ensuring maximum power transfer. For a switched-mode power amplifier (or inverter), a tunable matching network can ensure that the inverter sees the correct load to maintain high efficiency (e.g., preserving zero-voltage switching and other necessary operating characteristics).

1.2.5 Limitations of Existing TMNs

While existing tunable matching networks (TMNs) offer solutions for impedance matching, they come with distinct limitations depending on their specific implementations. These limitations become particularly problematic in applications with dynamically variable loads, such as in rf systems.

Mechanical Matching Systems:

One common implementation involves the use of stepper-motor-positioned variable vacuum capacitors to create variable reactances. This method can achieve a high degree of matching precision thanks to the fine control over the capacitor values. However, the major drawback of this system is its slow tuning response. The mechanical nature of the stepper motors inherently limits the speed at which the impedance can be adjusted, leading to a significant mismatch in applications requiring rapid response [35–40].

Switched Capacitor Banks:

Another approach employs switched banks of capacitors for impedance tuning. This method can theoretically adjust impedance values quickly, addressing the speed limitations of mechanical systems [3, 31]. However, achieving precise matching with switched capacitor banks is challenging. The discrete steps in which the capacitors are switched can lead to less accurate impedance matching compared to continuously variable systems [2, 18, 21]. This results in a compromise between matching precision and response speed.

In contrast, the phase-switched impedance modulation (PSIM) technique offers a promising solution by providing both high matching speed and high precision. However, the application of PSIM is restricted due to patent constraints[25, 41, 42].

1.3 Load Characteristics in RF Plasma

A popular method to create semiconductor plasmas involves using an rf power amplifier to transfer inductive coupling energy into a chamber filled with the gas meant for ionization. This is typically achieved by channeling rf current through a coil encircling the chamber, typically within the industrial, scientific, and medical (ISM) operating frequencies, such as 13.56 MHz, 27.12 MHz, and 40.68 MHz.

The effective impedance of the load in inductively coupled plasma (ICP) systems changes based on their operating conditions, temperature, gas type and pressure, power levels, etc. This variability often results in significant fluctuations in both the real and reactive components of the effective load impedance, making it a highly variable rf loading system. Moreover, plasma processing in many applications often produces rapid variations among different parameters, causing the plasma impedance to fluctuate rapidly (e.g., within a few microseconds) [35–38, 40].

This introduces loss and distortions in the power amplifier that cannot be adequately compensated for using standard TMNs due to their slow response times that typically span several seconds. Thus, standard rf PAs suffer greatly in generating and delivering power to the variable plasma load. Tunable matching systems that offer both precision and much faster matching are necessary to meet the demands of such plasma processing systems.

1.4 Motivation

Efficient rf power delivery within a narrow frequency range (e.g., several kHz around 13.56 MHz [43]) is required in many industrial applications where the rf loads vary dynamically with time. The need for a wide power range of the loading system, as well as the requirement for high peak power levels (such as peak power in kWs) and quick dynamic response (such as μs level), further complicate the situation. In addition, the ability to quickly adapt to changes in the rf loads is essential to ensuring stable and reliable operation of the plasma system.

These kinds of requirements are especially hard to meet in situations like plasma etching [44, 45], where the load characteristics change extremely rapidly. This poses a significant challenge to the PAs to efficiently deliver power to the plasma system, severely limiting their stability and efficiency [36, 39, 46, 47]. The rapidly changing operating conditions often compromise the performance and speed of existing rf power amplifiers, motivating the need for more adaptable solutions. One possible solution to address this challenge is the use of tunable matching networks that can dynamically adjust their operating parameters based on changing load characteristics within a short timescale. By continuously monitoring and adapting to load impedance variations, these amplifiers can maintain stability and efficiency even in rapidly changing operating conditions.

1.5 Thesis Objective

The objective of this thesis is to develop improved matching techniques that can provide both high precision and fast-response matching control for dynamically variable loads in radio frequency applications. This thesis investigates an entirely different matching approach to a conventional TMN that enables efficient impedance matching with both high-bandwidth matching precision and fast matching resolution over a wide matching range. The investigated matching system, termed a controllable transformation matching network (CTMN), leverages a switching network operated at the rf frequency to offer fast tuning responses for impedance matching. This allows for efficient and seamless matching of impedance between different components or systems.

1.6 Thesis Organization

This thesis is organized into five main chapters. Chapter 2 discusses the concepts of achieving dynamic transformations utilizing switching networks that are controllable. Chapter 3 presents the theory and development of a tunable matching network, termed a controllable transformation matching network (CTMN), utilizing the controllable switching network from Chapter 2. In addition, chapter 2 and 3 provide theoretical derivations and a thorough discussion of the design process Chapter 4 presents an example design for the proposed controllable transformation matching network (CTMN) and provides simulation results of an example design CTMN including ideal and non-ideal device parameters. Finally, Chapter 5 serves as the concluding chapter. It synthesizes the key findings of the work, summarizing their implications and potentially providing a foundation for future research in this area.

Chapter 2

Variable Transformer-Based Dynamic Impedance Transformation

High-frequency (HF) applications often necessitate the use of a tunable matching network (TMN), as discussed in Chapter 1. Typically implemented as ideally lossless, lumped-element networks, TMNs often employ reactive components as variable (tunable) elements to modulate the network's impedance at a frequency of interest or over a narrow frequency band. The choice of variable components within a TMN is crucial, as it determines the tuning resolution range and tuning speed, factors that are pivotal in matching the load impedance to a desired input impedance effectively.

Plasma loads represent a complex impedance, with variations in both their resistive and reactive components to provide an impedance match to a fixed, resistive input impedance. These loads necessitate a matching network with two degrees of freedom (e.g., two variable elements) in order to compensate for variations in load resistance and load reactance (or, looked at another way, to compensate for variations in load impedance magnitude and phase). This is often accomplished with an L-section matching network comprising two variable reactances (e.g., motor-driven variable vacuum capacitors, high-power varactors, a high-quality (Q) resonant tank in conjunction with dynamic frequency tuning, etc., as discussed in the previous chapter).

This chapter introduces an innovative approach to tunable matching networks, extending beyond the traditional two-element design [48]. There are two degrees of freedom in the proposed system. It accomplishes this by employing a two-port switching network as the primary variable element, which functions similarly to a variable transformer (rescaling impedance magnitude), and a standard variable reactance as the secondary component (providing a variation in reactance). The use of a switching network as a variable two-port element to rescale impedance magnitude is unique to the author's knowledge. The variable reactance may be realized through any conventional means and is conveniently realized with a high-Q filter network with dynamic frequency tuning (i.e., frequency modulation) for a variable reactance. Together, these two elements act to provide controllable impedance matching between its two RF ports.

The following sections will outline the realization of such a dynamically variable transformer using a controllable switching network. Section 2.1 introduces the basic concept, while Sections 2.2 and 2.3 focus on the design and operation of the switching network. Section 2.4 describes the resulting input and output waveforms and how the switching network achieves voltage and current transformation. Section 2.5 provides mathematical expressions and derivations for the network transformations. The last section introduces the development of a tunable matching network based on this switching network.

2.1 A Dynamically Variable Transformer

The core principle of an ideal transformer (illustrated in Fig. 2-1) is that its turns ratio, denoted as $\frac{N_2}{N_1}$ determines the voltage scaling (and inverse current scaling) between its primary and secondary. In an ideal scenario, the voltage conversion is directly proportional to the turns ratio, $v_2 = \frac{N_2}{N_1} v_1$, while its current is scaled in an inverse fashion, $i_2 = \frac{N_1}{N_2} i_1$. Consequently, an ideal transformer provides an impedance magnitude transformation between its two ports, with the impedance conversion scaling being proportional to the square of this ratio. Thus, an impedance Z_{L2} loading the secondary of a transformer appears as an impedance $Z_1 = (\frac{N_1}{N_2})^2 Z_{L2}$ looking into its primary, and vice versa. If we could control this turns ratio in real time, we would be able to provide a dynamic adjustment of impedance magnitude as seen at the primary port for a given impedance loading the secondary.

However, the real-world application of a transformer with a variable turns ratio presents several challenges. A conventional transformer is constructed with a set number of turns around a magnetic core, which cannot be altered without mechanical adjustments. While it's theoretically possible to design a conventional transformer with an adjustable number of turns to dynamically scale impedance, such a design in practice, however, would have many of the drawbacks of existing matching systems (e.g., slow response, discretization of tuning) and would also likely suffer from significant parasitic effects.

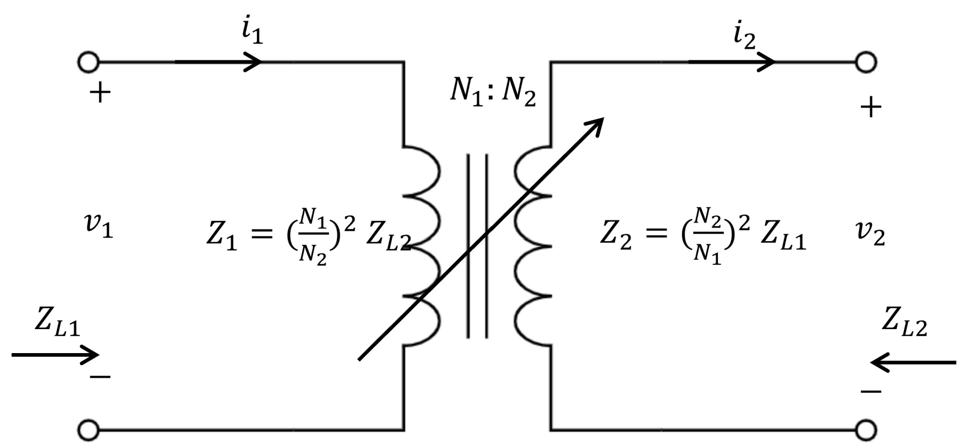

Figure 2-1: A theoretical variable transformer with dynamic turns ratio $\frac{N_2}{N_1}$ with primary and secondary impedances, currents, and voltages.

The above notwithstanding, a device mimicking the capabilities of a transformer with a dynamically variable turns ratio offers significant potential in tunable impedance matching. Imagine a hypothetical transformer whose turns ratio could be varied on demand in a continuous fashion as suggested in the illustration of Fig. 2-1; thus $\frac{N_2}{N_1}$ could be adjusted dynamically. The input and output impedances looking into ports 1 and 2 of the transformer are Z_{L1} and Z_{L2}, respectively. If the turns ratio is controlled dynamically, it will enable real-time, continuous adjustment of the magnitude by which impedances are scaled through the transformer, opening new possibilities for dynamic impedance matching. In the next section, we explore the design of such a switching network that approximately serves as a variable transformer as regards the fundamental components of the waveforms at its ports.

2.2 Introduction to the Two-Port Controllable Switching Network

This section outlines a two-port switching network comprising four switches in a bridge configuration and its associated switching sequence. The network is designed to switch among different states, each establishing a controlled path for energy transfer. As will be described later, by controlling the timing of the switch transitions, the effective transformation between the input port and the output port of the switching network can be adjusted, allowing for dynamic scaling of waveforms for matching.

2.2.1 Switching Network Topology

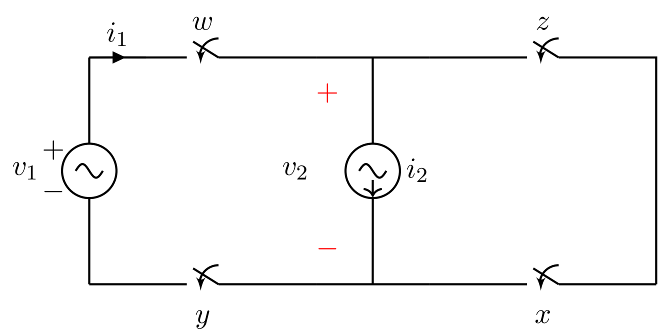

Figure 2-2: A simplified two-port switching network proposed to work as a variable transformer when operated with the switching sequences provided in Fig. 2-3.

Let us consider an idealized two-port switching network that connects two ac systems as illustrated in Fig. 2-2. In this configuration, the switching network serves as the power stage to transfer power from an ac input to an ac output. The input is modeled as a sinusoidal voltage source v_1, delivering a current i_1 into the switching network, while the load is represented by a sinusoidal current source i_2 with an output voltage v_2 across it that is controlled by the switching network. The switching network comprises four controlled switches, labeled w, x, y, and z arranged in a bridge configuration as shown in Fig. 2-2. The output voltage v_2 is related to the input voltage v_1 through the switching actions of the network, and likewise the input current i_1 is determined from the load current i_2 by the action of the switching network.

2.2.2 Switching Pattern:

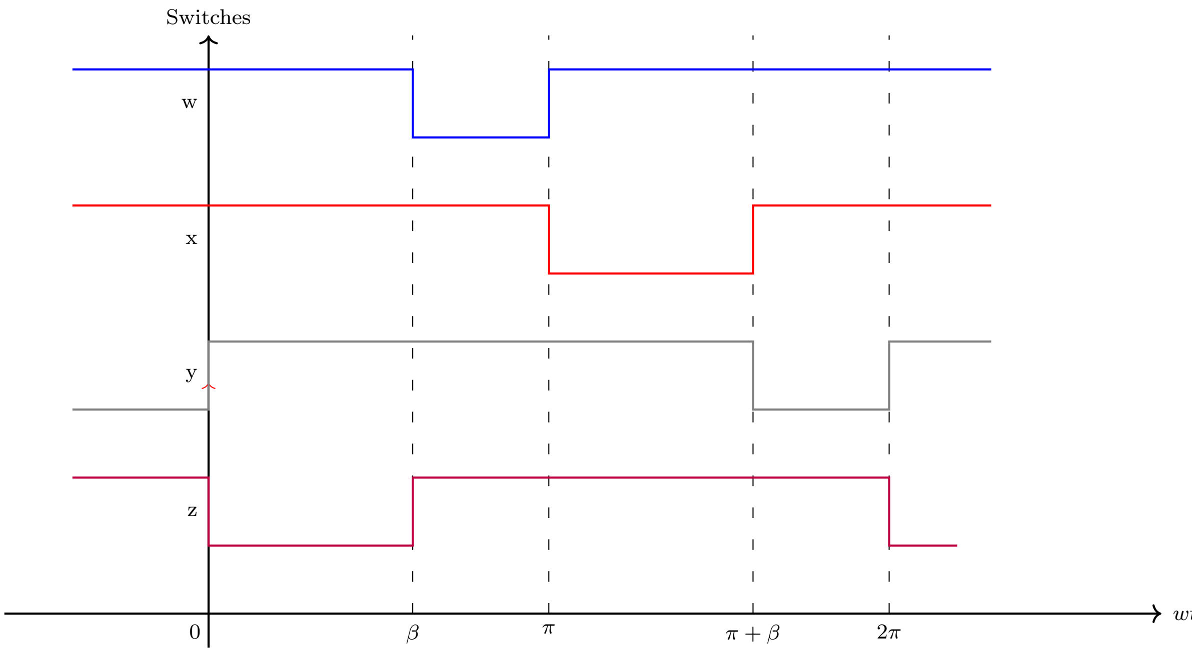

Figure 2-3: Switching sequences over one RF cycle for ideal switches w, x, y, z. A 'high' level indicates that a corresponding switch is on, while a 'low' level indicates that a corresponding switch is off. The switches are assumed to be ideal, meaning they turn on and off instantaneously.

The switching pattern of the circuit determines the relationship between the input and output waveforms and how the switching network serves to provide a controlled transformation between its input and output. Consider the switching pattern presented in Fig. 2-3, which illustrates the timing of the switch activation over one RF cycle. A 'high' level indicates that a corresponding switch is on, while a 'low' level indicates that a corresponding switch is off.

The switching cycle traverses an electrical angle ωt from 0 to 2π and features four transition points at angles β, π, $\pi + \beta$, and 2π resulting in a sequence of four phases. The transitions at the phase boundaries are controlled by only two switches that transition between on and off at each phase boundary, with each switch turning on and off only once within a complete switching cycle. Any given phase will have three switches conducting and one switch in an off state. The four phases within one cycle are outlined below:

(i) Phase 1: 0 to β : wxy ON

(ii) Phase 2: β to π : xyz ON

(iii) Phase 3: π to $\pi + \beta$: wyz ON

(iv) Phase 4: $\pi + \beta$ to 2π : wzx ON

Through this section, we have established aspects of the network: the physical arrangement of switches and the temporal sequence of their activation. The following section considers the operation of the two-port switching network during all four phases of the switch activation cycle for the switching waveforms presented discussed so far.

2.3 Circuit Behavior For Each Phase

As can be seen in the switching network in Fig. 2-3, the output (port 2) is connected to the input (port 1) through the switches w and y. Both of these switches must be in the conducting state for a continuous current path from the source to the load. If either of them is non-conducting, it breaks the path for current to flow. When there is no conductive path between the source and the load, no current can flow, and therefore no power can be transferred between the two ports. If the switches are synchronized with the switching sequence defined in Fig. 2-3 over one RF cycle, we observe different circuit responses during these four phases.

2.3.1 Phase 1: [0 to β] : wxy ON

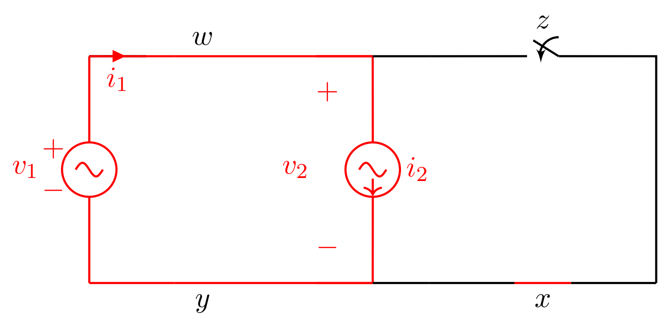

Figure 2-4: Phase 1: w x y are ON; z OFF

Phase 1, starts at electrical phase angle 0 when input voltage v_1 crosses zero with positive slope. Switch y turns on and switch z turns off at the start of the phase, such that switches w, x, and y are in the ON state, while switch z is off. This configuration results in a direct pathway from the source to the load as shown in Fig. 2-4. Current i_2 is drawn from the positive terminal of voltage v_1 and voltage v_2 is impressed across the load current i_2.The output voltage, v_2, mirrors the input v_1 and the input current i_1 mirrors the load current i_2, as shown in Table 2-1.

2.3.2 Phase 2 : [β to π] : yzx ON

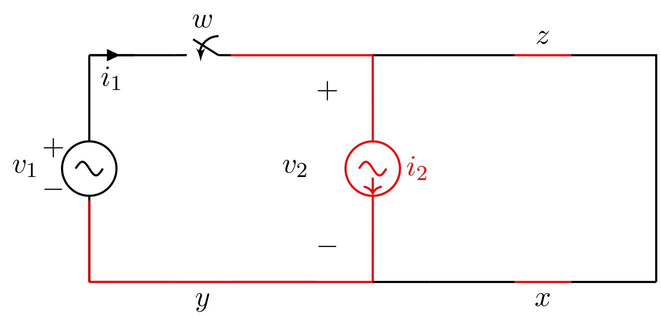

Figure 2-5: Phase 2: z, x, y are ON; w OFF

At phase angle β, switch w turns OFF, isolating the output from the input, and switch z turns on applying zero volts across the load. This switch configuration is shown in Fig. 2-5. Since switch w stays OFF, there is no energy transfer from input to output during this phase, and v_2 drops to zero. This phase persists until the phase angle reaches π. This is illustrated in Table. 2-1.

2.3.3 Phase 3: [π to $\pi + \beta$] :wyz ON

In the third phase, starting at phase angle π, when v_1 becomes negative, switch w resumes the 'ON' state, re-establishing a path for current from the source to the load, and switch x turns off. During this phase, the output current i_2 flows from v_1 (such that $i_2 = i_1$), and v_2 equals v_1 (which is negative during this interval). This phase persists until the electrical phase angle reaches $\pi + \beta$. The relations between input and output voltages and currents is summarized in Table 2.1.

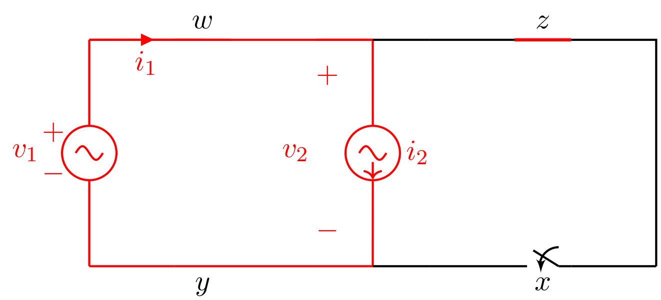

Figure 2-6: Phase 3: z w y are ON; x OFF

2.3.4 Phase 4: $[\pi + \beta$ to $2\pi]$: wzx ON

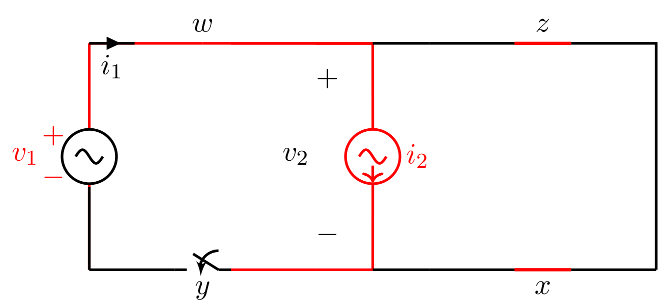

Figure 2-7: Phase 4: wzx are ON; y OFF

The final stage of the cycle starts at electrical angle $\pi + \beta$, when switch y opens, disconnecting the load from the source, and switch x closes, resulting in the configuration shown in Fig. 2-7. This configuration results in a condition where no current can flow between the source and the load stopping any power transfer. It results in a zero voltage across the load, v_2=0 and a no current drawn from the source, $i_1 = 0$. The system remains in this state until the cycle repeats, entering phase 1 at 2π.

2.4 Analyzing Voltage and Current Transformations

As of now, it has been established that the two-port switching network under consideration is regulated in a way that prevents or limits the amount of energy transfer from the input to the output during a specified phase. Complete voltage transfer is achieved during phases 1 and 3, when the output voltage v_2 is equivalent to the input voltage v_1 and the current i_1 supplied by the input corresponds to the output current i_2. In contrast, phases 2 and 4 isolate the load from the source, leading to zero-voltage states across the output v_2 indicating no supply of current i_1 drawn from the input. A summary of the consequences of this switching operation is provided in Table 2.1. The controlled switching effectively induces variations in the fundamental amplitudes of the input current and output voltage throughout the four phases. In this section, we will qualitatively analyze the signal transformations that occur as a result of the switching operation.

Phase	**Phase Range**	**Active (Output) Phase Angle**	**Output Voltage, v_2**	**Input Current, i_1 Drawn From Input Voltage, v_1**
P1	$0 < \omega t < \beta$	β	v_1	i_2
P2	$\beta < \omega t < \pi$	0	0	0
P3	$\pi < \omega t < \pi + \beta$	β	v_1	i_2
P4	$\pi + \beta < \omega t < 2\pi$	0	0	0

Table 2.1: Summary of input and output voltages and currents in each phase due to the switching.

2.4.1 Voltage Transformation

According to Table. 2.1, the output voltage v_2 exactly follows the input voltage v_1 in phases 1 and 3, but includes zero-voltage states during phases 2 and 4. Consider that the input voltage applied to the network is represented by a sinusoidal signal $v_1(\omega t) = V \sin(\omega t)$, where V is the amplitude and ω is the angular frequency of the voltage signal. The output voltage v_2 will be a 'chopped' or 'gated' sinusoidal waveform that follows v_1 in phases 1 and 3, and is 0 during phases 2 and 4.

The black waveform illustrated in Fig. 2-8 represents the input voltage v_1 and the red waveform in the same figure represents the output voltage v_2. As seen from the figure, the output waveform, v_2 replicates the input waveform, v_1 in each half cycle for some phase durations (P1 and P3). For the remainder of the half cycle (P2 and P4), output waveform v_2 remains at 0 when the input waveform is still sinusoidal. This results in a 'chopped', or 'phase-controlled' appearance of the output waveform $v_2(\omega t)$ when compared to the input waveform v_1. Thus the transformation is determined by the effective phase duration, or

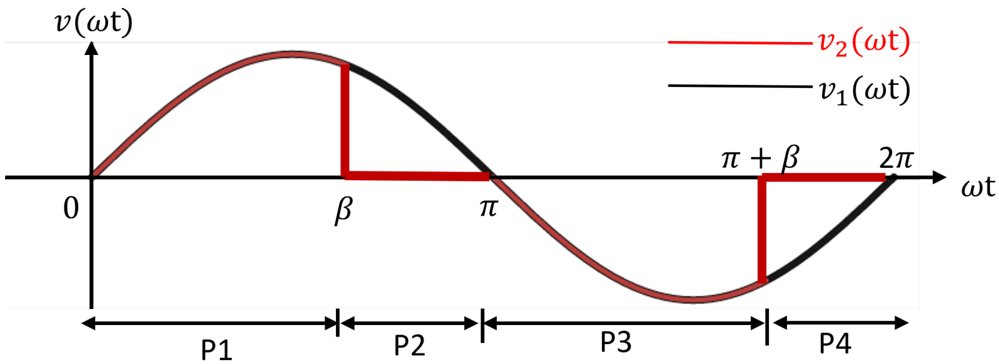

Figure 2-8: Voltage transformation demonstrated by the switching network: the sinusoidal input voltage v_1 is transformed into the stepped output voltage v_2.

duty cycle of the output signal. The phase duration is determined by a variable phase angle denoted as β and is established by the switching patterns.

$v_1(t)$ comprises only a fundamental frequency component, while $v_2(t)$ comprises a fundamental component and harmonics. As v_2 is a gated version of v_1 (with certain portions zeroed out), the fundamental component of the output voltage ($v_{2,fund}$) is necessarily smaller than the fundamental component of the input voltage ($v_{1,fund}$), such that $v_{2,fund} < v_{1,fund}$. As a result, the network generates a scaled-down version of the input voltage at the output in terms of the fundamental frequency component. Thus, owing to the switching operation, the two-port network achieves a step-down voltage transformation from the input to the output or a step-up voltage transformation from the output to the input (in terms of fundamental frequency components).

The durations of the non-zero and the zero phases in each half cycle are β and $\pi - \beta$, respectively. By changing β, the zero-state durations can be controlled. Hence, by modulating β, the voltage transformation can be regulated. For instance, setting $\beta = \pi$ leads to an active phase duration of $\beta = \pi$ for each half cycle in Fig. 2-8, and as a consequence, the output voltage, v_2 overlaps with the input voltage, v_1. This results in a full voltage delivery ($v_2 = v_1$)) from the input to the output with no voltage transformation. When setting β to 0, it results in a zero-voltage state throughout each half cycle. As a consequence, no voltage is transferred from the input to the output ($v_2 = 0$), and a full voltage transformation occurs.

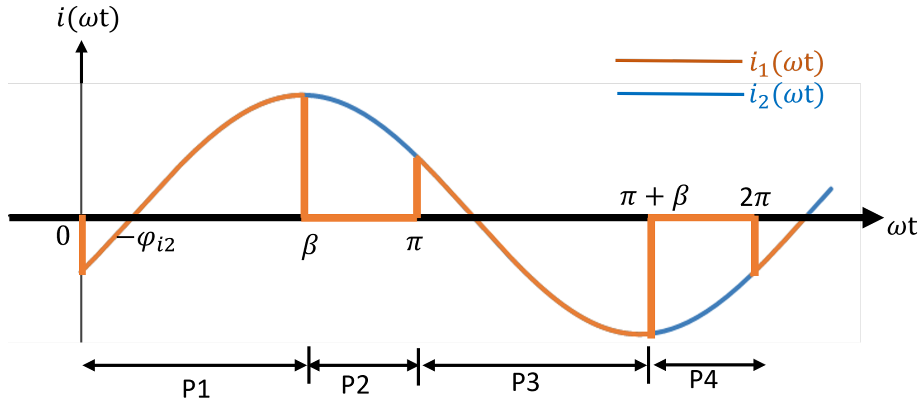

Figure 2-9: Step-down transformation of input current i_1 from output current i_2 as a result of the switching. The absolute phase is referenced to $v_1(\omega t)$ being a sine wave.

2.4.2 Current Transformation

The transformation from output current to input current can be assessed in the same manner as the voltage conversion. In our analysis above, we observed that the output voltage followed the sinusoidal input voltage, except with the presence of zero-voltage states during phases 2 and 4. Likewise, the input current i_1 drawn from the source equals the output current i_2 except during these phases when it is zero. From Table 2.1, i_1 follows the sinusoidal output current i_2 during phases 1 and 3, but the current i_1 is zero during phases 2 and 4. Thus, the input current i_1 will be a 'chopped' or 'gated' sinusoidal waveform when compared to the output current i_2.

The blue waveform shown in Fig. 2-9 illustrates a pure sinusoidal current waveform $i_2(wt)$ with a phase shift of ϕ_{i2}. Since the input current i_1 follows the output current i_2 in phases 1 and 3 and is zero during phases 2 and 4, the current i_1 appears as a 'chopped' or 'gated' version of the current i_2. The orange waveform shown in Fig. 2-9 serves as an illustration. For the same reasons discussed for voltage conversion, the magnitude of the fundamental component of the input current ($i_{1,\text{fund}}$) is smaller than that of the output current ($i_{2,\text{fund}}$), leading to a transformed or scaled-down input current waveform with respect to the output waveform. Notice that a phase shift (ϕ_{i1}) is indicated in the current waveforms in Fig. 2-9 with respect to their complementary voltage waveforms in Fig. 2-8. As will be discussed later, the phase shift ϕ_{i1} might or might not be zero depending on the operating conditions.

Thus, the switching network effectively results in the input current i_1 being a scaled-down version of the output current i_2 in terms of its fundamental frequency component, achieving a step-down current transformation from the output to the input or, conversely, a step-up current transformation from the input to the output. For the same reasons outlined in the previous section, the phase control angle β also governs the current transformation.

Because the switching network produces a fundamental voltage v_2 that is scaled down from voltage v_1 and a fundamental current i_1 that is scaled down from current i_2, it provides a transformation of the fundamental voltage and current resembling that of a transformer. Because the switching is ideally lossless, no energy is lost in the transformation provided by the switching network. Moreover, because the input voltage v_1 and output current i_2 are each sinusoidal, average power transfer (i.e., over an AC cycle) can only occur via the fundamental components of i_1 and v_2.

In the switching network, however, unlike an actual ideal transformer, the input voltage and (fundamental) output voltage are not necessarily in phase, nor are the output current and (fundamental) input current. This aspect of the waveforms of the system will be considered later.

2.5 Quantitative Analysis of Signal Transformations

In the preceding discussion, we established that the controllable switching network is capable of transforming voltage and current between its input and output ports (as regards fundamental frequency components). This transformation is facilitated through a switching action that scales a sinusoidal input voltage into a 'gated' output voltage by inserting zero states. This action also scales a sinusoidal output current into a 'gated' input current. The zero-state durations (determined by angle β) determine the degree of (fundamental) voltage and current scaling. Moving forward, our focus will be on developing mathematical expressions that accurately represent the resulting transformed signals as transformation factors controlled by the phase angle.

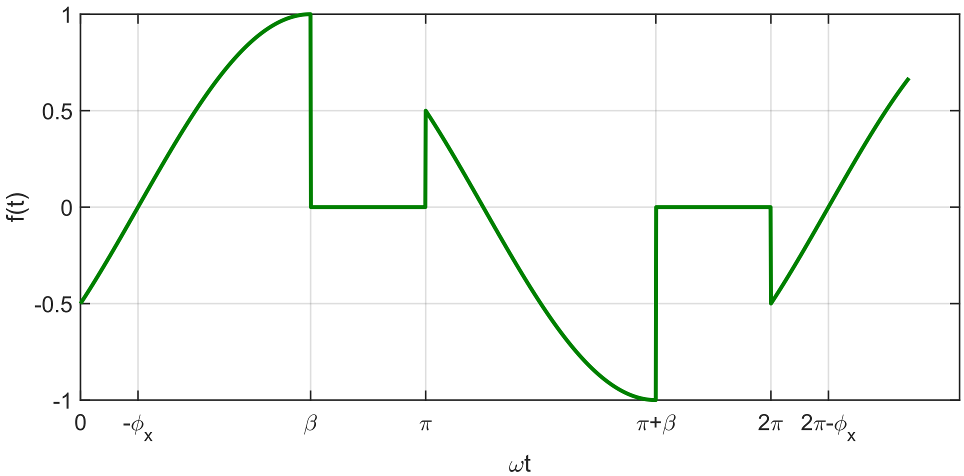

Figure 2-10: A function, $f(t)$, representing the waveforms of the transformed signals in this analysis. It is symmetric about its mean.

2.5.1 Modeling Transformed Signals

Consider Fig. 2-10, which illustrates one switching cycle of a waveform that is a 'gated sinusoid'—a sinusoid having certain waveform portions set to zero. The horizontal axis of the figure represents the phase angle, while the vertical axis indicates the instantaneous value of the waveform, with the amplitude of the sinusoidal section of $f(t)$ set to unity. This waveform crosses zero positive at an angle denoted as $-\phi_x$ and has its first zero portion between angles β and π. A second zero state occurs between $\pi + \beta$ and 2π. $f(t)$ can be expressed as:

$$f(t) = \begin{cases} 0, & \text{for } \beta < \omega t < \pi \\ & \text{and } \pi + \beta < \omega t < 2\pi \\ \sin(\omega t + \phi_x), & \text{otherwise} \end{cases} \tag{2.1}$$

This function, $f(t)$ can be used to represent the waveforms of the transformed voltage and current signals v_2 and i_1 discussed previously. By finding the magnitude and phase of the fundamental of $f(t)$, we will have a means to describe the fundamental components of v_2 and i_1 of the switching network waveforms.

2.5.2 Fourier Representation

The Fourier series expansion of the periodic function $f(t)$ may be expressed as:

$$f(t) = a_0 + \sum_{n=1}^{\infty} [a_n \sin(n\omega t) + b_n \cos(n\omega t)] \tag{2.2}$$

Where a_0 represents the dc component and a_n and b_n are the Fourier coefficients corresponding to the harmonics of the fundamental frequency component, ω of the signal. The fundamental component of $f(t)$ is denoted as $f_1(t)$ and may be expressed as

$$f_1(t) = a_1 \sin(\omega t) + b_1 \cos(\omega t) \tag{2.3}$$

where a_1 and b_1 represent the fundamental components of the harmonics defined as:

$$a_1 = \frac{2}{T} \int_0^T f_1(t) \sin(\omega t)\, d(\omega t) \tag{2.4}$$

$$b_1 = \frac{2}{T} \int_0^T f_1(t) \cos(\omega t)\, d(\omega t) \tag{2.5}$$

Applying these equations and some trigonometric relations, we can derive the Fourier coefficients a_1 and b_1 of $f(t)$ as functions of β and ϕ_x. Detailed derivations can be found in Appendix A.

$$a_1 = \frac{\beta}{\pi} \cos(\phi_x) - \frac{1}{\pi} \sin(\beta) \cos(\beta + \phi_x) \tag{2.6}$$

$$b_1 = \frac{\beta}{\pi} \sin(\phi_x) - \frac{1}{\pi} \sin(\beta + \phi_x) \sin(\beta) \tag{2.7}$$

β and ϕ_x are defined as the phase angle and the phase shift of the function $f(t)$ illustrated in Fig. 2-10. Thus, the fundamental component of the 'gated' sinusoidal $f(t)$, denoted $f_1(t)$, can be expressed in terms of ϕ_x and β as:

$$f_1(t) = [\frac{\beta}{\pi}\cos(\phi_x) - \frac{1}{\pi}\sin(\beta)\cos(\beta+\phi_x)]\sin(\omega t)$$
$$+[\frac{\beta}{\pi}\sin(\phi_x) - \frac{1}{\pi}\sin(\beta+\phi_x)]\sin(\beta)\cos(\omega t) \quad (2.8)$$

Applying trigonometric identities and further simplifying $f_1(t)$, we can represent the fundamental of $f(t)$ as:

$$f_1(t) = \sqrt{a_1^2 + b_1^2}\sin(wt + \tan^{-1}\left(\frac{a_1}{b_1}\right)) \quad (2.9)$$

$$\Rightarrow f_1(t) = M\sin(\omega t + \psi) \quad (2.10)$$

The parameters M and ψ represent the magnitude and the phase shift of $f_1(t)$ with respect to a sine wave, as defined below:

$$M = \sqrt{a_1^2 + b_1^2} \quad (2.11)$$
$$\psi = \tan^{-1}\left(\frac{a_1}{b_1}\right) \quad (2.12)$$

Hence, M and ψ give us the magnitude and phase of the fundamental of the 'gated' signal $f(t)$ with respect to its phase angle and phase shift if we can determine the values of M and ψ.

2.5.3 Transformation Factors

Folding the defined coefficients a_1 (Eqn. 2.4) and b_1 (Eqn. 2.5) into the equations for M (Eqn. 2.11) and ψ (Eqn. 2.12) allows us to solve for the magnitude and phase of the fundamental of $f(t)$. Detailed derivations are provided in Appendix A.

$$M = M(\beta, \phi_x) = \sqrt{\frac{\beta^2}{\pi^2} + \frac{1}{\pi^2}\sin^2(\beta) - \frac{2\beta}{\pi^2}\sin(\beta)\cos(\beta + 2\phi_x)} \quad (2.13)$$

$$\psi = \psi(\beta, \phi_x) = \tan^{-1}\frac{\beta\sin(\phi_x) + \sin(\beta)\sin(\beta+\phi_x)}{\beta\cos(\phi_x) - \sin(\beta)\cos(\beta+\phi_x)} \quad (2.14)$$

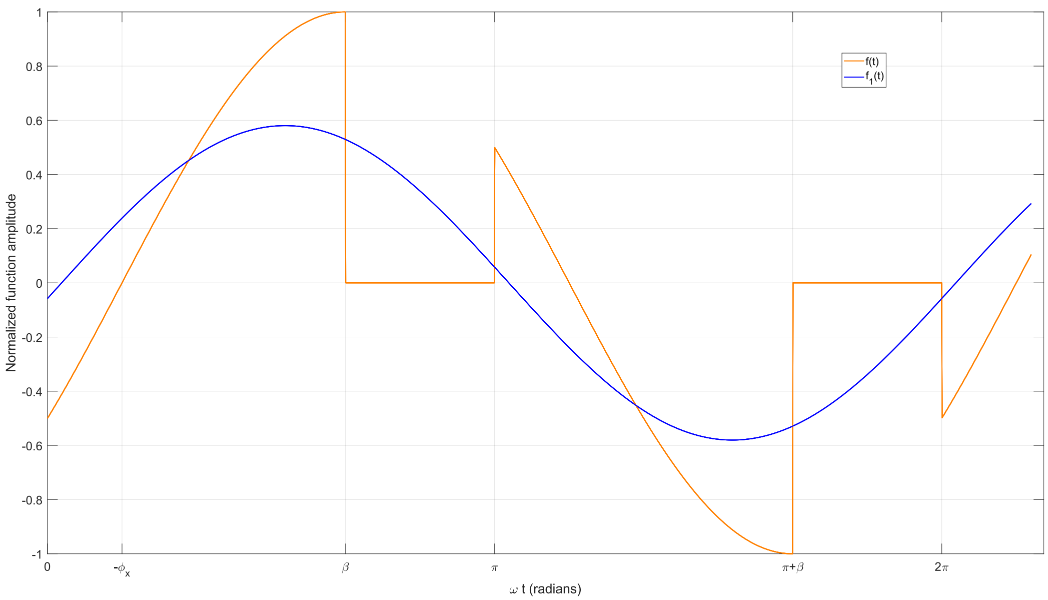

Figure 2-11: A 'gated' sinusoidal signal $f(t)$ (orange waveform) and the fundamental component $f_1(t)$ (blue waveform) of the gated signal $f(t)$ over one period. The values used for this example plot are $\beta = \frac{2\pi}{3}$ radians and $\phi_x = \frac{\pi}{6}$ radians.

We have, therefore, $f_1(t) = M(\beta, \phi_x)\sin(\omega t + \psi(\beta, \phi_x))$, where β and ψ are as defined in Eqns. 2.13 and 2.14. Both M and ψ given in Eqns. 2.13 and 2.14 represent functions defined by two variables, β and ϕ_x, where beta defines the region of $f(t)$ that is gated and ϕ_x denotes the phase shift of the underlying sinusoid in the function $f(t)$ with respect to a sine wave. Example waveforms of $f(t)$ and $f_1(t)$ are shown in Fig. 2-11.

2.5.4 Application to the Switching Network

Given the relation of the switched waveform $f(t)$ to the switching network voltage v_2 and current i_1, the functions $M(\beta, \phi_x)$ and $\psi(\beta, \phi_x)$ can be used to represent the magnitude and phase transformation factors of fundamental components between the two ports in the switching network as controlled by β and ϕ_x. Each of i_1 and v_2 in the switching network of Fig. 2-11 can be expressed in terms of a scaled version of $f(t)$ in Fig. 2-10, as seen in Figs. 2-8 and 2-9. The phase shift ϕ_x is assumed to be zero for $v_1(t)$ and a known variable for $i_1(t)$ based on the load connected to the switching network. Therefore, the primary variable that controls both the magnitude $M(\beta, \phi_x)$ and phase $\psi(\beta, \phi_x)$ of the transformation provided by the switching network is β.

Because β controls the durations of the zero states of v_2 and i_2, the fundamental-frequency amplitudes of voltage v_2 and current i_1 can be controlled by varying the phase angle β, and the relative phases of the fundamental components of i_1 and v_2 will likewise be determined by β. This concept of modulating the phase angle β to control signal transformation between the ports is referred to here as β modulation. By adjusting β a desired signal transformation therefore can be achieved.

2.5.5 Output Voltage Step-Down Transformation

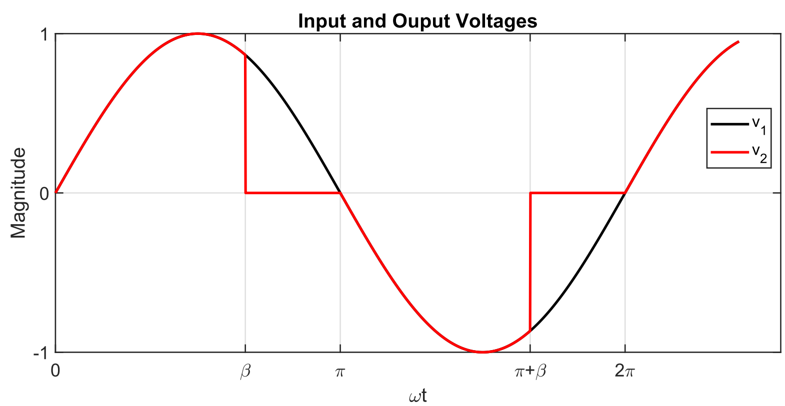

Figure 2-12: Relation of the output voltage v_2 (red waveform) to the input voltage v1 of the switching network. v_2 is transformed from the input voltage v_1 with no phase shift. Here, $\beta = \frac{2\pi}{3}$ radians.

Consider the waveforms illustrated in Fig. 2-12 represent the input voltage v_1 and the transformed output voltage v_2 of the switching network of Fig. 2-11 with the switching pattern of Fig. 2-3. The output voltage v_2 is a chopped sinusoid 'gated' at a phase angle, denoted by β over one switching cycle. According to our discussion from the last section, the magnitude and phase shift of the fundamental component of the output voltage v_2 will be modified by the two transformation factors derived in Eqns. 2.13 and 2.14 where the control angle is β and the phase shift is 0.

Assuming an input voltage magnitude of V, the input voltage can be represented by $v_1 = V\sin(wt)$. The phasor representation for v_1 is:

$$\hat{v}_1 = Ve^{-j\frac{\pi}{2}} \tag{2.15}$$

such that $v_1(t) = \text{Re}\{\hat{v}_1 e^{j\omega t}\}$. The phase duration of the output voltage $v_2(\omega t)$ is the gated region defined by β and the phase shift with respect to the input signal is 0. The magnitude and phase shift of the fundamental of the output voltage v_2 will be affected by the magnitude $M(\beta, \phi_x)$ and the phase $\psi(\beta, \phi_x)$ transformation factors defined at $(\beta, 0)$. By applying these phase values to the transformation functions derived in Eqns. 2.13 and 2.14, we obtain the magnitude and phase transformation factors for v_2 as a function of phase angle β.

$$M(\beta,0) = \sqrt{\frac{\beta^2}{\pi^2} + \frac{1}{\pi^2}\sin^2(\beta) - \frac{2\beta}{\pi^2}\sin(\beta)\cos(\beta)} \tag{2.16}$$

$$= \frac{1}{\pi}\sqrt{\beta^2 + \sin^2(\beta) - 2\beta\sin(\beta)\cos(\beta)} \tag{2.17}$$

$$\psi(\beta,0) = \tan^{-1}\frac{\beta + \sin(\beta)\sin(\beta)}{\beta - \sin(\beta)\cos(\beta)} \tag{2.18}$$

The magnitude of the fundamental of v_2 will be scaled by the derived transformation factor $M(\beta, 0)$.

$$|\hat{v_2}| = |\hat{v_1}| \times M(\beta,0) = V \times M(\beta,0) \tag{2.19}$$

The phase of the fundamental of v_2 will be shifted by the transformation factor $\psi(\beta, 0)$.

$$\phi_{v2} = \psi(\beta,0) \tag{2.20}$$

The phasor $\hat{v_2}$ for the fundamental component of the transformed output voltage v_2 will be:

$$\hat{v}_2 = |\hat{v}_1| \times M(\beta,0) \times e^{j\psi(\beta,0)} \times e^{-j\frac{\pi}{2}} \tag{2.21}$$

$$\Rightarrow \hat{v}_2 = V \times M(\beta,0) \times e^{j(\tan^{-1}\frac{\beta+\sin(\beta)\sin(\beta)}{\beta-\sin(\beta)\cos(\beta)})} \times e^{-j\frac{\pi}{2}} \tag{2.22}$$

such that the fundamental of the transformed output voltage will be $v_{2,fund}(t) = \text{Re}\{\hat{v}_2 e^{jwt}\}$. The fundamental component of the transformed output voltage can be represented as a sinusoidal function defined as v_2 with a magnitude of $V_2 = VM(\beta, 0)$ and a phase shift of $\psi(\beta, 0) = \tan^{-1}(\frac{\beta+\sin(\beta)\sin(\beta)}{\beta-\sin(\beta)\cos(\beta)})$.

$$v_{2,fund} = VM(\beta, 0) \times \sin(\omega t + \psi(\beta, 0)) \tag{2.23}$$

2.5.6 Output Current Behavior

Up to now, we have treated the load current of the switching network as an independent current source having a magnitude of I_2 and a phase (with respect to a sine wave) of ϕ_x. If we assume that there is actually a load impedance connected to the port v_2 of the switching network that only responds to the fundamental component of v_2, we can identify i_2 for a given control angle β. (That is, we assume that the fundamental of voltage v_2 drives an impedance, which results in a sinusoidal load current i_2.)

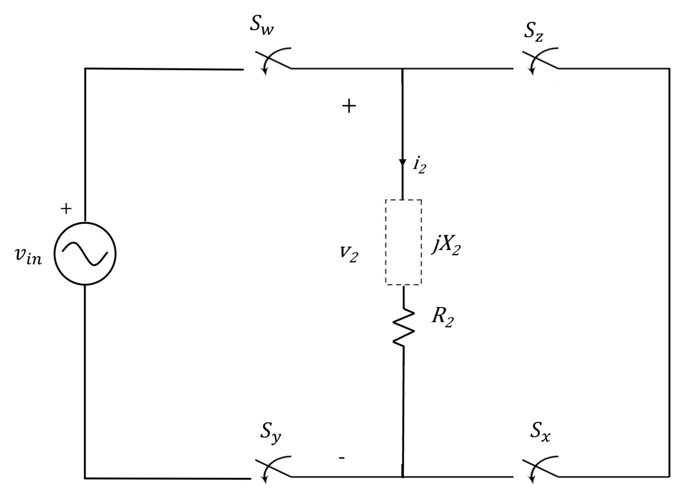

Figure 2-13: The switching network is driven by a sinsuoidal voltage v_1, and is loaded by an impedance $Z_2 = R_2 + jX_2$.

Under the above assumption, the output current can be determined from the output voltage applied across the impedance loading the secondary port of the switching network, as illustrated in Fig. 2-13. We model the loading impedance as $Z_2 = R_2 + jX_2$, where R_2 represents the resistance and X_2 represents the reactance of Z_2. Alternatively, Z_2 can be expressed in terms of its magnitude, $|Z_2|$ and phase angle, $\angle Z_2$ as:

$$Z_2 = R_2 + jX_2 \tag{2.24}$$

$$|Z_2| = \sqrt{R_2^2 + X_2^2}, \quad \angle Z_2 = \tan^{-1}\left(\frac{X_2}{R_2}\right). \tag{2.25}$$

$$\Rightarrow Z_2 = |Z_2|\, e^{j\angle Z_2} \tag{2.26}$$

In our analysis, we have defined the phasor representation of the transformed output fundamental voltage $\hat{v_2}$ in Eqn. 2.22. Considering a load characterized by impedance Z_2, we can proceed to calculate the output current phasor $\hat{i_2}$.

$$\hat{i_2} = \frac{\hat{v_2}}{Z_2}$$

$$\hat{i_2} = \frac{V \times M(\beta, 0) \times e^{-j\frac{\pi}{2}} \times e^{j\psi(\beta,0)}}{|Z_2|\, e^{j\angle Z_2}} \tag{2.27}$$

$$\Rightarrow \hat{i_2} = \frac{V \times M(\beta, 0)}{|Z_2|} \times e^{j(\psi(\beta,0)-\angle Z_2)} e^{-j\frac{\pi}{2}} \tag{2.28}$$

$$\Rightarrow \hat{i_2} = \frac{V \times M(\beta, 0)}{\sqrt{R_2^2 + X_2^2}}\, e^{j(\psi(\beta,0)-\tan^{-1}\frac{X_2}{R_2})} e^{-j\frac{\pi}{2}} \tag{2.29}$$

$$\Rightarrow \hat{i_2} = |I_2| e^{j\phi_{i2}} e^{-j\pi/2} \tag{2.30}$$

Here $|I_2|$ represents the magnitude and ϕ_{i_2} represents the phase shift of the output current $i_2(t)$ with respect to a sine wave, and is found as follows:

$$|I_2| = \frac{V \times M(\beta, 0)}{\sqrt{R_2^2 + X_2^2}} \tag{2.31}$$

$$\phi_{i2} = \psi(\beta, 0) - \tan^{-1}\left(\frac{X_2}{R_2}\right) \tag{2.32}$$

$M(\beta, 0)$ and $\psi(\beta, 0)$ represent the transformation factors defined in Eqns. 2.16 and 2.18. Therefore, we can fully express the output current i_2 in terms of the given input voltage and load impedance.

2.5.7 Input Current Step-Down Transformation

Revisiting our current transformation analysis due to the switching action, as detailed in Section 2.4, we recall that the input current experiences a step-down transformation from the output current. Specifically, i_1 will be scaled down from i_2 by the magnitude $M(\beta, \phi_x)$ transformation factor, and i_1 will be shifted by a phase of $\psi(\beta, \phi_{i2})$ with respect to the output current i_2.

The magnitude and phase transformation factors of i_1 at (β, ϕ_{i2}) are defined as:

$$M(\beta, \phi_{i2}) = \sqrt{\frac{\beta^2}{\pi^2} + \frac{1}{\pi^2}\sin^2(\beta) - \frac{2\beta}{\pi^2}\sin(\beta)\cos(\beta + 2\phi_{i2})} \tag{2.33}$$

$$\psi(\beta, \phi_{i2}) = \tan^{-1}\frac{\beta\sin(\phi_{i2}) + \sin(\beta)\sin(\beta + (\phi_{i2})}{\beta\cos(\phi_{i2}) - \sin(\beta)\cos(\beta + (\phi_{i2})} \tag{2.34}$$

Where ϕ_{i2} is derived in Eqn. 2.32. The magnitude of $\hat{i_1}$ will be scaled by the magnitude transformation factor $M(\beta, \phi_{i2})$:

$$|I_1| = |I_2| \times M(\beta, \phi_{i2}) \tag{2.35}$$

$$\Rightarrow |I_1| = \frac{V \times M(\beta, 0)}{\sqrt{R_2^2 + X_2^2}} \times M(\psi(\beta, 0) - \tan^{-1}\left(\frac{X_2}{R_2}\right)) \tag{2.36}$$

Likewise, the phase of i_1 will be shifted by the phase transformation factor, $\psi(\beta, \phi_{i2})$ with respect to i_2:

$$\phi_{i1} = \psi(\beta, \phi_{i2}) \tag{2.37}$$

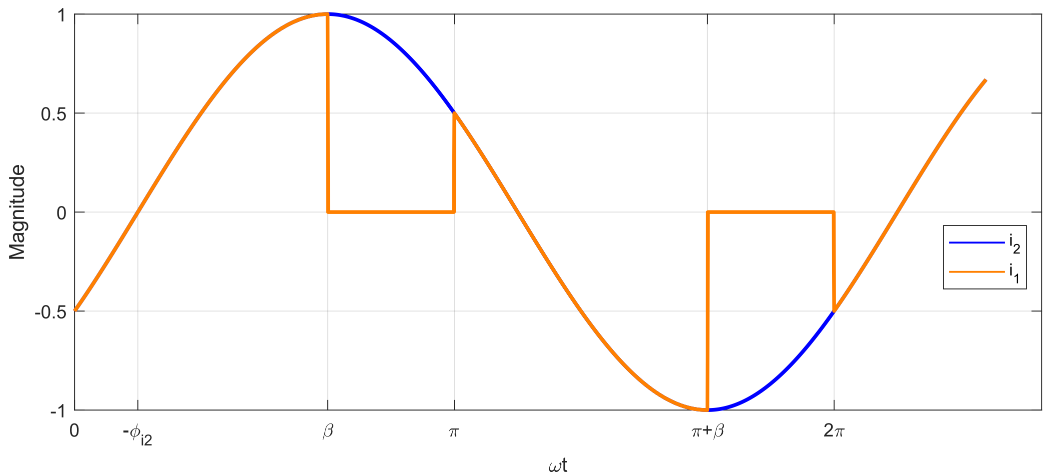

Figure 2-14: Step-down transformation of input current i_1 from output current i_2 by the magnitude and phase transformation factors at (β, ϕ_{i2}). Here, $\beta = \frac{2\pi}{3}$ radians and $\psi_{i2} = \frac{\pi}{6}$ radians.

which, substituting in Eqn. 2.32 gives

$$\phi_{i1} = \psi\left(\beta, \psi(\beta, 0) - \tan^{-1}\left(\frac{X_2}{R_2}\right)\right) \tag{2.38}$$

For the output current phasor $\hat{i_2}$, given by $|I_2|e^{j\phi_{i2}}e^{-j\frac{\pi}{2}}$, the fundamental component of the input current $\hat{i_1}$ transformed from $\hat{i_2}$ is expressed as follows:

$$\hat{i_1} = |I_2| \times M(\beta, \phi_{i2}) \times e^{j\psi(\beta,\phi_{i2})}e^{-j\frac{\pi}{2}} \tag{2.39}$$

$$\Rightarrow \hat{i_1} = |I_1| \times e^{j\phi_{i1}}e^{-j\frac{\pi}{2}} \tag{2.40}$$

The fundamental component of the transformed input current $i_{1,fund} = I_1 \sin(wt + \phi_{i_1})$ represents a sinusoidal signal with a magnitude of $|I_1|$ and a phase shift of ϕ_{i1} with respect to a sine wave. The orange waveform in Fig. 2-14 illustrates the input current i_1, and the blue waveform represents the output current i_2.

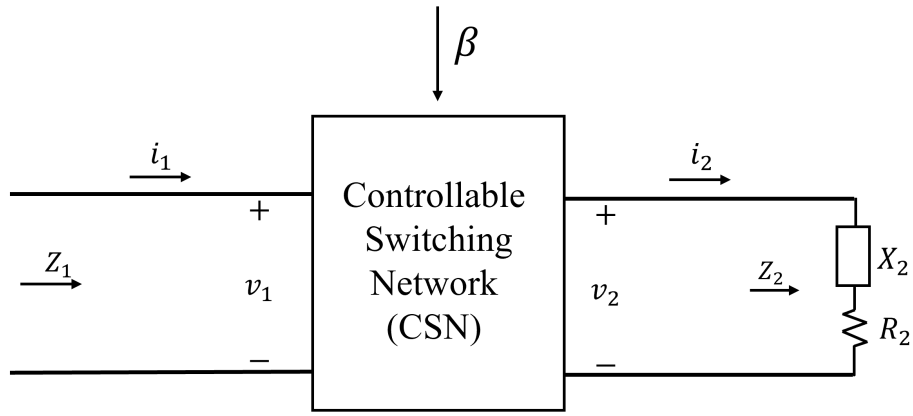

Figure 2-15: Voltage and current transformations within the controllable switching network (CSN) with performing β modulation.

2.5.8 Impedance Transformation

In this section, we have explored how the controllable switching network (CSN) can dynamically adjust the fundamental components of voltage and current signals between its two ports. The phase control angle β is directly responsible for a step-down voltage transformation from the input v_1 to the fundamental component of the output v_2 and a step-down current transformation from the output i_2 to the fundamental component of the input i_1. From the perspective of fundamental frequency components, we could treat this as transforming a load impedance Z_2 at the output port of the switching network to an impedance Z_1 seen looking into the input of the switching network as a result of the controlled transformation. The fundamental components of the signals associated with the switching network are illustrated in Fig. 2-15 and can be mathematically represented as follows:

$$\hat{v_1} = Ve^{-j\frac{\pi}{2}} \tag{2.41}$$

$$\hat{v_2} = Ve^{-j\frac{\pi}{2}}\, M(\beta,0)e^{j\psi(\beta,0)} \tag{2.42}$$

$$\hat{i_2} = Ve^{-j\frac{\pi}{2}}\, \frac{M(\beta,0)}{\sqrt{R_2^2+X_2^2}} e^{j(\psi(\beta,0)-\tan^{-1}\frac{X_2}{R_2})} \tag{2.43}$$

$$\hat{i_1} = Ve^{-j\frac{\pi}{2}}\, \frac{M(\beta,0)\,M(\beta,\phi_{i2})}{\sqrt{R_2^2+X_2^2}}\, e^{j(\psi(\beta,0)-\tan^{-1}\frac{X_2}{R_2})} \tag{2.44}$$

The control angle β is in charge of controlling these transformations. By determining the duration of the effective switching action, the switching network achieves impedance transformation between its two ports. The switching action also causes a phase shift between the fundamental components of the input and output signals. Later, we will show that, as compared to an ideal transformer, this phase shift reflects some degree of reactive energy transfer effect, which might be represented as an additional reactance in series with the output of the transformer.

The effective input impedance (as regards fundamental-frequency components) looking into the switching network is Z_1. Considering the fundamental components of the input voltage and current, we can represent Z_1 as follows:

$$Z_1 = \frac{\hat{v}_1}{\hat{i}_1} \tag{2.45}$$

$$= \frac{V e^{-j\frac{\pi}{2}}}{|I_1| e^{j\phi_{i1}} e^{-j\frac{\pi}{2}}} \tag{2.46}$$

$$= \frac{V}{|I_1| e^{j\phi_{i1}}} \tag{2.47}$$

Plugging in the values from Eqn. 2.41 and Eqn. 2.44,

$$Z_1 = \frac{\sqrt{R_2^2 + X_2^2}}{M(\beta, 0) \times M\left(\psi(\beta, 0) - \tan^{-1}\left(\frac{X_2}{R_2}\right)\right)} \times e^{-j\psi\left(\beta, \psi(\beta,0) - \tan^{-1}\left(\frac{X_2}{R_2}\right)\right)} \tag{2.48}$$

If $|Z_1|$ is the magnitude and $\angle Z_1$ is the phase angle of the impedance Z_1,

$$|Z_1| = \left| \frac{\sqrt{R_2^2 + X_2^2}}{M(\beta, 0) \times M\left(\psi(\beta, 0) - \tan^{-1}\left(\frac{X_2}{R_2}\right)\right)} \right| \tag{2.49}$$

$$\angle Z_1 = -\psi\left(\beta, \psi(\beta, 0) - \tan^{-1}\left(\frac{X_2}{R_2}\right)\right) \tag{2.50}$$

The phasor representation of the equivalent fundamental-frequency input impedance looking into the switching network is $Z_1 = |Z_1| e^{j\angle Z_1}$. It can be expressed in terms of its resistance and reactance as follows:

$$Z_1 = R_1 + jX_1 \tag{2.51}$$

R_1 and X_1 are the real and imaginary parts of the input impedance, respectively, and are defined as:

$$R_1 = |Z_1| \cos(\angle Z_1) \tag{2.52}$$

$$X_1 = |Z_1| \sin(\angle Z_1) \tag{2.53}$$

Given the output impedance, $Z_2 = |Z_2|e^{j\angle Z_2}$ in Eqn. 2.26,

$$\frac{|Z_1|}{|Z_2|} = \frac{\sqrt{R_2^2 + X_2^2}}{M(\beta, 0) \times M(\psi(\beta, 0) - \tan^{-1}(\frac{X_2}{R_2}))} \times \frac{1}{\sqrt{R_2^2 + X_2^2}} \tag{2.54}$$

$$\Rightarrow \frac{Z_1}{Z_2} = \frac{1}{M(\beta, 0) \times M(\psi(\beta, 0) - \tan^{-1}(\frac{X_2}{R_2}))} \tag{2.55}$$

$$\Rightarrow Z_1 = Z_2 \times \frac{1}{M(\beta, 0)} \times \frac{1}{M(\psi(\beta, 0) - \tan^{-1}(\frac{X_2}{R_2}))} \tag{2.56}$$

Realizing $M(\psi(\beta, 0) - \tan^{-1}(\frac{X_2}{R_2})) = M(\beta, \phi_{i2})$ from Eqn. 2.32,

$$|Z_1| = |Z_2| \times \frac{1}{M(\beta, 0)} \times \frac{1}{M(\beta, \phi_{i2})} \tag{2.57}$$

The switching network scales the impedances between the two ports by magnitude factors governed by β.

2.6 Controllable Switching Network as a Dynamically Variable Transformer

The switching network shown in Fig. 2-15 transforms the fundamental components of v_1 into v_2 and i_2 into i_1 which is the key function of a magnetic transformer. However, unlike an ideal transformer, the network introduces additional phase shifts among fundamental components owing to the switching action. As regards fundamental-frequency components, we might model the action of the switching network as a transformer-based network with an added series reactance X_T as depicted in Fig. 2-16. What this suggests is that the switching network can be conceptualized as comprising a variable transformer, along with a reactance, that facilitates variable transformation between the ports.

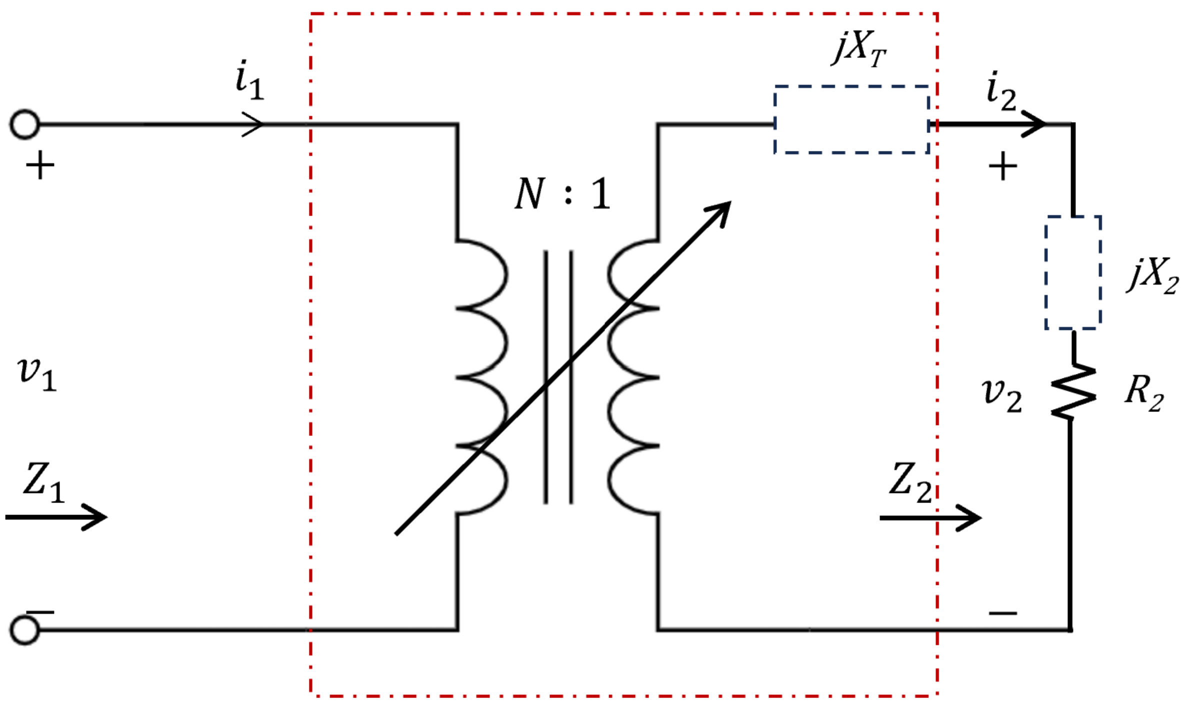

Figure 2-16: A fundamental-frequency model of the controlled switching network incorporating a transformer with variable turns ratio N:1 and a secondary-side series variable reactance X_T. N and X_T are functions of both the control angle Beta and the loading impedance $Z_2 = R_2 + jX_2$.

In the transformer depicted in Fig. 2-16, the total impedance in loading the secondary winding of the ideal transformer, denoted as Z_2', comprises the load reactance X_2 and a series reactance X_T. This can be represented as:

$$Z_2' = R_2 + j(X_T + X_2) \tag{2.58}$$

For a transformer with an $N : 1$ turns ratio, where Z_2' is the secondary impedance, the primary impedance, Z_1, is given by:

$$Z_1 = N^2 \cdot Z_2' = N^2 \cdot (R_2 + j(X_T + X_2)) \tag{2.59}$$
$$= N^2 \cdot R_2 + jN^2 \cdot (X_T + X_2) \tag{2.60}$$
$$= R_1 + jX_1 \tag{2.61}$$

Here, R_1 and X_1 are determined by the output resistance, R_2 and reactance, X_2 scaled by the square of the turns ratio. Specifically, they are defined as follows:

$$R_1 = N^2 \cdot R_2 \tag{2.62}$$
$$X_1 = N^2 \cdot (X_T + X_2) \tag{2.63}$$

By plugging in $R_1 = |Z_1| \cos(\angle Z_1)$ into Eqn. 2.62, we get:

$$N^2 = \frac{R_1}{R_2} = \frac{|Z_1| \cos(\angle Z_1)}{R_2} \tag{2.64}$$

$$\Rightarrow N = \sqrt{\frac{|Z_1| \cos(\angle Z_1)}{R_2}} \tag{2.65}$$

$$N = \sqrt{\frac{1}{R_2} \times \frac{\sqrt{R_2^2 + X_2^2}}{M(\beta, 0) \times M\left(\psi(\beta, 0) - \tan^{-1}\left(\frac{X_2}{R_2}\right)\right)} \cos\left(-\psi\left(\beta, \psi(\beta, 0) - \tan^{-1}\left(\frac{X_2}{R_2}\right)\right)\right)} \tag{2.66}$$

As we discussed, N (Eqn. 2.66) represents the turns ratio (N:1) of the variable transformer illustrated in Fig. 2-16. Here, N is a function of β, R_2, and X_2. This suggests that the turns ratio of the transformer, N, is controlled by the phase angle β and the load impedance Z_2 of the network.

Similarly, by plugging $X_1 = |Z_1|\sin(\angle Z_1)$ into Eqn. 2.63, we get:

$$X_T = \frac{1}{N^2}X_1 - X_2 \tag{2.67}$$
$$= \frac{1}{N^2}|Z_1|\sin(\angle Z_1) - X_2 \tag{2.68}$$

$$\Rightarrow X_T = -X_2 + \frac{1}{N^2}\frac{\sqrt{R_2^2 + X_2^2}}{M(\beta,0)\times M\left(\psi(\beta,0) - \tan^{-1}\left(\frac{X_2}{R_2}\right)\right)}\sin(-\psi\left(\beta,\psi(\beta,0) - \tan^{-1}\left(\frac{X_2}{R_2}\right)\right)) \tag{2.69}$$

$$\Rightarrow X_T = -X_2 + \frac{\pi}{N^2}\frac{\sqrt{R_2^2 + X_2^2}}{\sqrt{\beta^2 + \sin^2(\beta) - 2\beta\sin(\beta)\cos(\beta)}\cdot M(\tan^{-1}\frac{\beta+\sin(\beta)\sin(\beta)}{\beta-\sin(\beta)\cos(\beta)} - \tan^{-1}(\frac{X_2}{R_2}))}$$
$$\times \sin\left(-\psi(\psi(\beta,0) - \tan^{-1}(\frac{X_2}{R_2}))\right) \tag{2.70}$$

The controlled switching network therefore functions as a variable transformer with a tunable turns ratio of $N:1$ and an additional secondary-side reactance X_T as illustrated in Fig. 2-17. It facilitates dynamic impedance transformation between its ports through the adjustment of phase control angle β. In the context of the fundamental waveform components, the switching network can thus be viewed as a sort of variable transformer. Here β controls the variable turns ratio $N:1$ and this is further complemented by an additional reactance X_T. For a specific value of β, the transformed impedance Z_1 and the corresponding reactance value X_T can be precisely determined from a known impedance Z_2.

We can effectively counteract the additional reactance X_T by introducing an opposite reactance $X_{net} = -X_T$ within the network, as illustrated in Fig. 2-17. A series output filter can provide the required reactance X_{net} to neutralize X_T (where X_{net} may also incorporate the load reactance). By dynamically tuning the filter tank frequency, the reactive components in the filter can produce a wide range of reactances for X_{net}. This implementation of the reactive filters enables the switching network to more closely mimic the transformation characteristics of an ideal transformer by compensating for the additional phase shift due to the switching action.

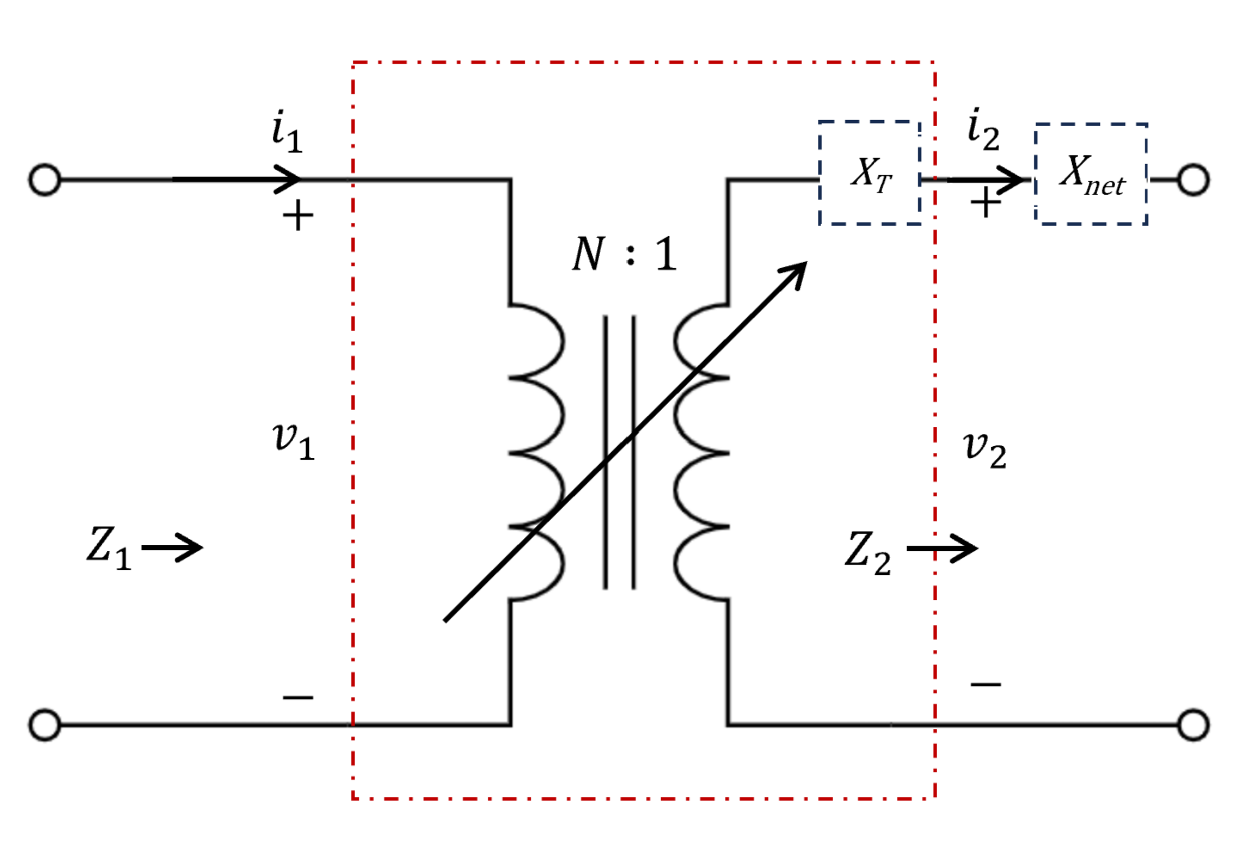

Figure 2-17: A reactance X_{net} added to the variable transformer-based network to compensate for the additional reactance X_T.

2.7 Development of a Variable Transformer-Based Tunable Matching Network

Building upon our existing two-port switching network configuration, as shown in Fig. 2-2, integrating filters at its two ports allows us to effectively extract fundamental signal components for processing within the network. A voltage-selecting filter at the input (RF port 1) and a current-selecting filter at the output (RF port 2) of the CSN illustrated in Fig. 2-18 specifically ensure that the network processes only the essential signals.

As has been established throughout this chapter, the two-port controllable switching network (CSN) dynamically transforms impedance magnitudes by operating at a variable phase angle β. This system acts as a variable transformer with an adjustable turns ratio. The reactive elements in these filters can be adjusted to provide variable reactances via dynamic

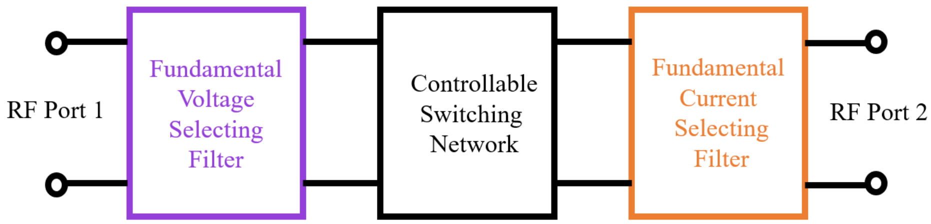

Figure 2-18: Block diagram of a two-port controllable switching network integrated with an input voltage selecting filter at RF port 1 and an output current selecting filter at RF port 2.

frequency tuning (DFT). Consequently, the network comprises two variable components: the first is the CSN, functioning as a dynamic transformer, and the second is the compensation reactance, which can be provided by the output-side fundamental current-selecting filter.

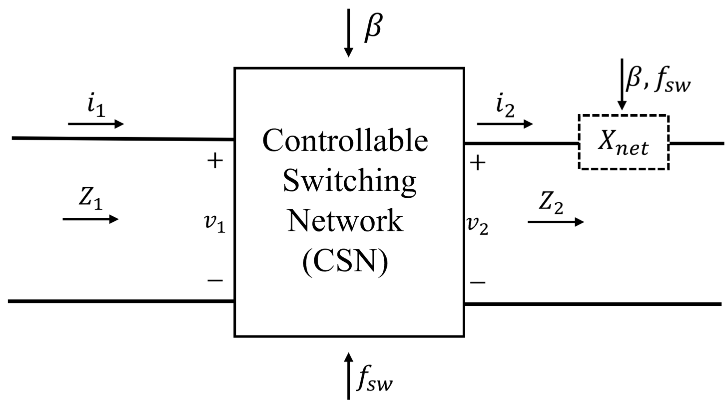

Figure 2-19: A net reactance X_{net} in series with the CSN provides two adjustable elements in the switching network. This reactance may be provided by the combination of the load reactance and filter reactance. The switching network operates at a phase angle β, and an output series filter provides the reactance X_{net} while operating at a frequency f_{sw} controlled by β.

With the integration of these filters, we evolve our switching network into a two-element matching network by leveraging the combined capabilities of the filters and the CSN. Modulating these two components yields a dual degree of freedom to achieve tunable impedance matching (see Fig. 2-19). The phase angle β serves as the primary control mechanism, adjusting impedances between the ports by governing the network switch timings (and thus switching frequency, f_{sw}). Concurrently, β also governs the output filter to operate at a frequency f_{sw} associated with the phase angle β. Through dynamic frequency tuning, the filter introduces an additional degree of control. As such, β becomes the regulatory factor for both variable elements, leading to a dual-control system, conceptually illustrated in Fig.

2-18. This system, defined as the controllable transformation matching network (CTMN) in this work, presents a versatile approach to two-element impedance matching networks.

In the next chapter, we explore the control techniques of the phase angle β in detail to achieve a desired impedance match between the two ports of this switching network.

Chapter 3

Design Approach for A Wide-Range Controllable Transformation Matching Network

In the preceding chapter, we explored the foundational principles of controllable switching network-based dynamic transformation techniques. We concluded with a discussion on how the switching network acts—for purposes of fundamental frequency components—like a controllable transformer with an additional series reactance that is a function of the switching angle β. Building upon this foundation, Chapter 3 introduces the development of a fast and dynamic impedance matching network, termed a controllable transformation matching network (CTMN), by implementing modulation techniques based on the controllable switching network (CSN).

The matching approach presented uses two variable elements to provide impedance matching between an RF input port (e.g., the output of a PA) and an RF output port (e.g., an RF plasma load). The primary variable element of the matching method is the two-port switching network explored in Chapter 2. It approximately serves as a variable transformer (i.e., a transformer with a variable turns ratio), providing one control handle for the desired impedance transformation. The second element is a conventional variable reactance, which may be implemented by the output filter through the use of frequency modulation (or dynamic frequency tuning). Together with the variable reactance, the controllable switching network can match the impedance between its two RF ports, accounting for both real and reactive variations in the load impedance.

3.1 System Structure of the Controllable Transformation Matching Network (CTMN)

In this section, we review the system structure of the transformation matching network based on the switching network.

3.1.1 Review of Variable Transformer-Based Dynamic Transformation

Fig. 3-1 shows the transformer-based transformation network, as demonstrated in Chapter 2. The input voltage to this system is defined by the phasor $\hat{v_1} = Ve^{-j\frac{\pi}{2}}$. In the system, the phasors of the fundamental components of the transformed output voltage $\hat{v}_2$ and input current $\hat{i_1}$ are determined by the switching angle β of the network, as expressed in Eqn. 3.1 and Eqn. 3.2, respectively. The switching process modifies the signal magnitudes and induces phase shifts, which are characterized by the addition of reactance X_T to the network, as detailed in Eqn. 3.3.

$$\hat{v_2} = Ve^{-j\frac{\pi}{2}}\, M(\beta,0)e^{j\psi(\beta,0)} \tag{3.1}$$

$$\hat{i_1} = Ve^{-j\frac{\pi}{2}}\, \frac{M(\beta,0)\, M(\beta,\phi_{i2})}{\sqrt{R_2^2 + X_2^2}}\, e^{j(\psi(\beta,0)-\tan^{-1}\frac{X_2}{R_2})} \tag{3.2}$$

Here, the phase shift between the fundamental of the input current phasor $\hat{i_1}$ and the voltage phasor $\hat{v_1}$ is represented by the angle $\psi((\beta,0) - \tan^{-1}\frac{X_2}{R_2})$. We refer to this angle as

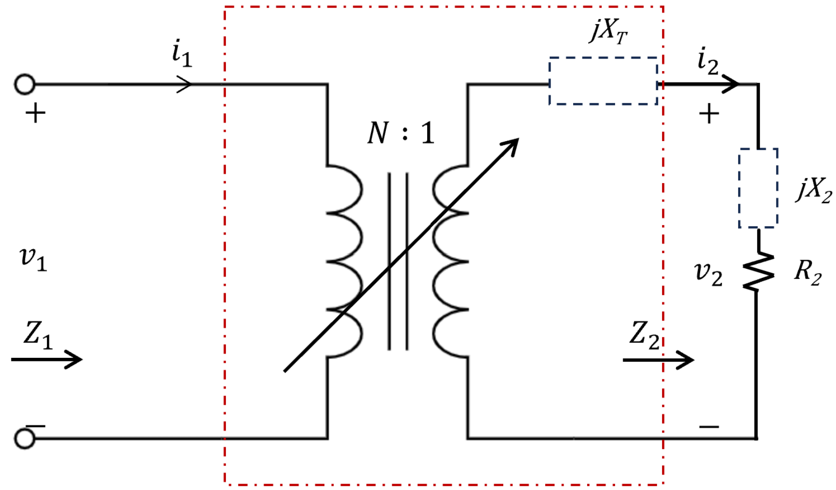

Figure 3-1: A fundamental-frequency model of the controlled switching network incorporating a transformer with variable turns ratio N:1 and a secondary-side variable reactance X_T. The network transforms $\hat{v_1}$ to $\hat{v_2}$ and introduces a phase shift in the system.

the phase shift ϕ_{i1}. This phase shift causes a reactance X_T in the system as defined below:

$$X_T = -X_L + \frac{\pi}{N^2}\frac{\sqrt{R_2^2+X_2^2}}{\sqrt{\beta^2+\sin^2(\beta)-2\beta\sin(\beta)\cos(\beta)}\cdot M(\tan^{-1}\frac{\beta+\sin(\beta)\sin(\beta)}{\beta-\sin(\beta)\cos(\beta)}-\tan^{-1}(\frac{X_2}{R_2}))}$$
$$\times \sin(-\psi(\psi(\beta,0)-\tan^{-1}(\frac{X_2}{R_2}))) \tag{3.3}$$

3.1.2 Introduction to the CTMN

In the previous section, we demonstrated that the controllable two-port switching network acts as a variable transformer in terms of the fundamental-frequency signal components. Integrating the switching network with filters creates a system, which we refer to as a controllable transformation matching network (CTMN). This integration is illustrated in Fig. 3-2, presenting a high-level block diagram of our system.

A key feature of the CTMN structure presented in Fig. 3-2 is the addition of a series output filter to the RF port 2 of the switching network. Figure 3-3 provides a more detailed view of the network architecture using the specific switching network we have discussed in this thesis.

This thesis primarily focuses on the characteristics and implications of this output series filter. While the inclusion of an input filter is also part of our design, it is not the primary

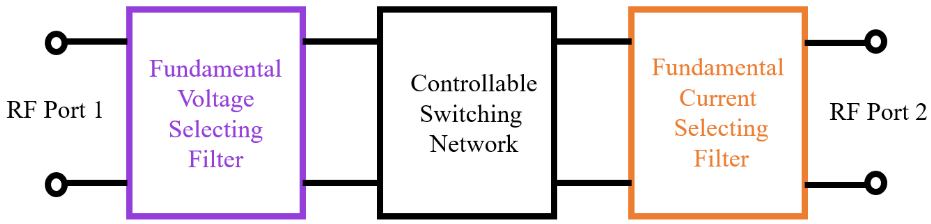

Figure 3-2: Block diagram of a two-port controllable switching network integrated with an input voltage selecting filter at RF port 1 and an output current selecting filter at RF port 2.

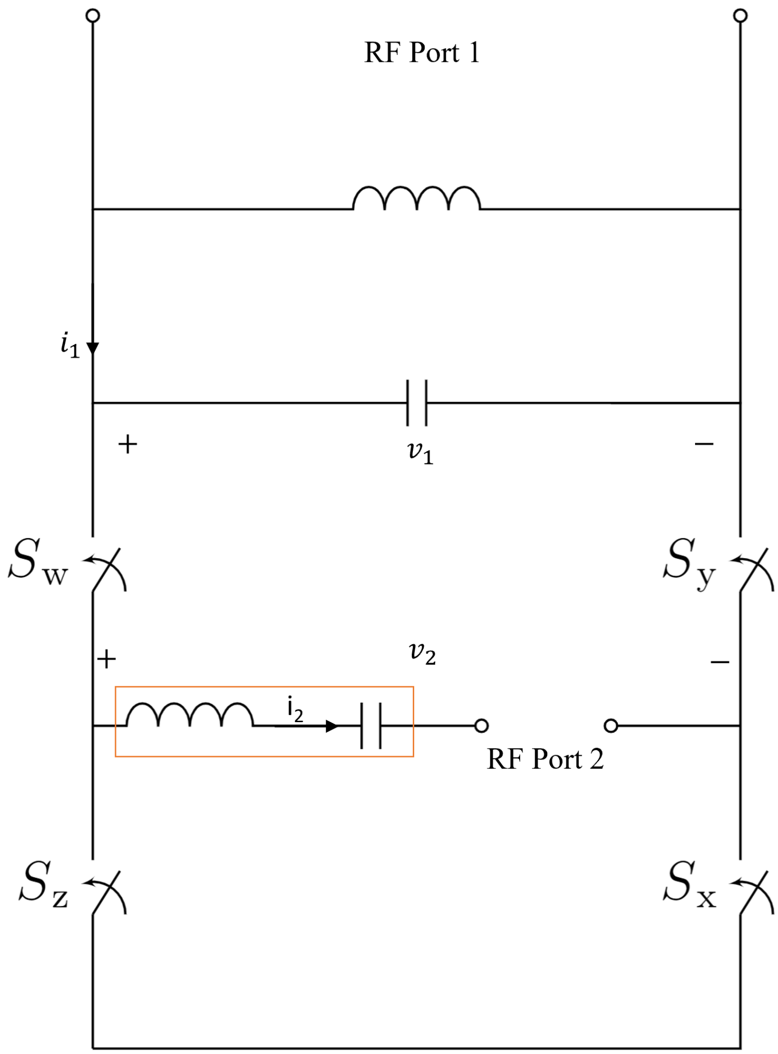

Figure 3-3: Circuit architecture of the CTMN, illustrating the integration of the series output filter at RF port 2 and parallel input filter at the RF port 1 with the two-port switching network.

focus of this thesis. For the sake of completeness, we have incorporated a parallel input filter into the network shown in Fig. 3-3. However, the details and specific characteristics of this input filter are not explored extensively in this context. The output filter serves (1) to select the fundamental component of the output current and (2) to introduce a controllable reactance, X_{comp}, in series with the load. This reactance value can be adjusted through frequency modulation, representing one of the two variable elements in the CTMN system. The first variable element is the controllable switching network (CSN) and the second variable element is the variable reactance X_{comp} provided by the series output current selecting filter.

Thus, the Controllable Switching Network (CSN) is responsible for transforming the input voltage phasor $\hat{v}_1$ into the output voltage phasor $\hat{v}_2$, while also introducing a reactance to the system. By connecting a load impedance, designated as $Z_L = R_L + jX_L$, in series with the series output filter at RF port 2 of the CTMN illustrated in Fig. 3-3, and representing the switching network in a block diagram, we arrive at the configuration depicted in Fig. 3-4. In this figure, X_L corresponds to the inductive component of the load, and X_{comp} denotes the reactance contributed by the series output filter.

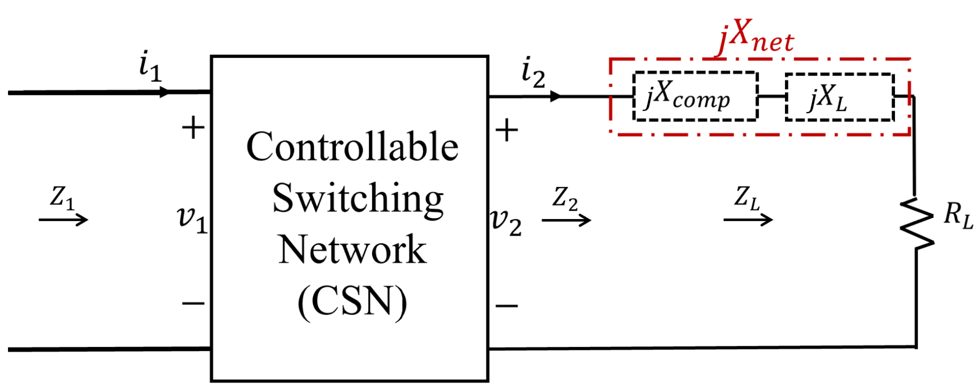

Figure 3-4: CSN-based transformation matching network. The network transforms $Z_L = R_L + jX_L$ to impedance Z_1.

In Fig. 3-4, the net reactance observed looking out of the switching network comprises the filter tank reactance X_{comp} and the load reactance X_L, represented as $X_L + X_{comp}$. Consequently, the net impedance seen from the CSN is $R_L + j(X_L + X_{comp})$. If we denote this net reactance as X_{net}, we can express it as follows:

$$X_{net} = X_{comp} + X_L \tag{3.4}$$

Considering this, the total impedance Z_2 looking out of the CSN is then:

$$Z_2 = R_L + jX_{net} \tag{3.5}$$

We can conceptualize the entire system as a controllable transformation matching network (CTMN) with an input and output port, as depicted in Fig. 3-4. The input impedance looking into this system is denoted as Z_1. When an input voltage phasor $\hat{v}_1$ is applied to the switching network, it produces a transformed output voltage phasor $\hat{v}_2$. Similarly, the network transforms the input current phasor $\hat{i}_1$, as defined by the equations (3.1) and (3.2), while introducing a reactance X_T described by equation (3.3). The primary objective of the CTMN presented is to match a reactive impedance Z_L to a purely resistive input impedance Z_0 (i.e., to make $Z_1 = Z_0$).

3.2 Control of the CTMN

The switching angle β of the controllable switching network is one control parameter used to regulate the matching in the controllable transformation matching network illustrated in Fig. 3-4. As seen in Section 3.1, the phasors of the fundamental components of the transformed output voltage (Eqn. 3.1) and input current (Eqn. 3.2) signals are defined by β. β governs the degree to which the magnitude of the load resistance is scaled up by the switching network. As a secondary effect, the CTN also introduces a β -dependent phase shift between the signals at the input and output of the CTMN, as indicated by the reactance X_T added to the network as a result of switching (Eqn. 3.3). Since β controls the transformations in the CTMN, by modulating β, the matching in the network can be controlled.

3.2.1 Impedance Transformation and Phase Control in the CTMN

For a purely resistive input impedance Z_0, the fundamental voltage and current at the input of the network are in phase, implying that the phase shift between voltage and current is zero at the input. For a given input voltage phasor $\hat{v_1} = Ve^{-j\frac{\pi}{2}}$ and a transformed input current phasor $\hat{i_1}$ (Eqn. 3.2), the phase shift ϕ_{i1} needs to be zero. Considering Eqn. 3.2,

$$\phi_{i1} = \psi\left(\beta, \psi(\beta, 0) - \tan^{-1}\left(\frac{X_{\text{net}}}{R_L}\right)\right) = 0 \tag{3.6}$$

We can solve this equation to precisely calculate the relationship between the impedance transformation ratio and the phase angle, β in the CTMN. Detailed derivations are provided in Appendix B.

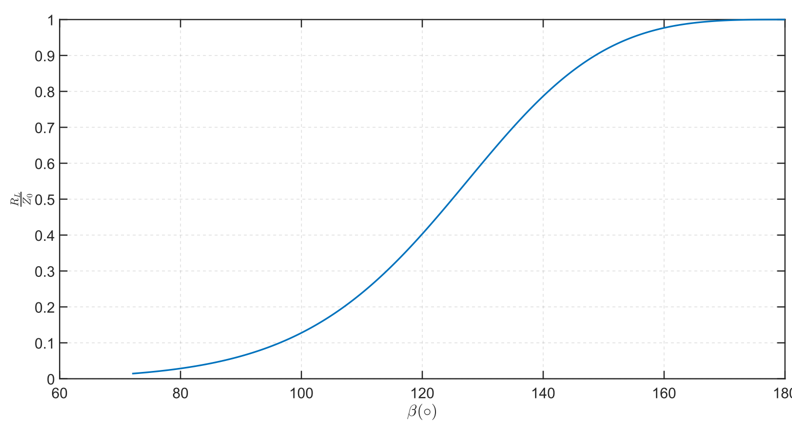

Figure 3-5: Selection of phase control angle β for a desired transformation ratio of $\frac{R_L}{Z_0}$.

$$\frac{R_L}{Z_0} = \frac{1}{\pi}\frac{\sqrt{\beta^2 + \sin^2(\beta) - 2\beta\sin(\beta)\cos(\beta)}}{\sqrt{1 + [\frac{2\beta\sin^2(\beta)}{\beta^2 - \sin^2(\beta)\cos^2(\beta) - \sin^4(\beta)}]^2}} M(\beta, \tan^{-1}(\frac{-\sin^2(\beta)}{\beta + \sin(\beta)\cos(\beta)})) \tag{3.7}$$

1. Required β for a desired transformation of $\frac{R_L}{Z_0}$ from the input port to the output port

Eqn. 3.7 enables us to determine the relationship between the "primary to secondary" transformation ratio $\frac{R_L}{Z_0}$ and the phase angle β, as illustrated in Fig. 3-5. Modulating β within $0 < \beta < 180°$ allows for a full range of impedance transformation ratios between 0 and 1. That is, we can match any value of load resistance R_L up to an equal or higher target value Z_0.Applying a specific phase control angle β achieves a desired resistive transformation ratio of $\frac{R_L}{Z_0}$. As an example, achieving a transformation ratio of 0.4 requires a $\beta = 120°$.

2. Net reactance associated with the phase control angle β

Eqn 3.8 calculates the necessary reactance, X_{net}, required to counterbalance the extra reactance introduced in the network for a desired transformation of $\frac{X_{net}}{R_L}$. A full range of transformation $\frac{R_L}{Z_0}$ defines a range of required X_{net}. Detailed derivations are provided in Appendix B.

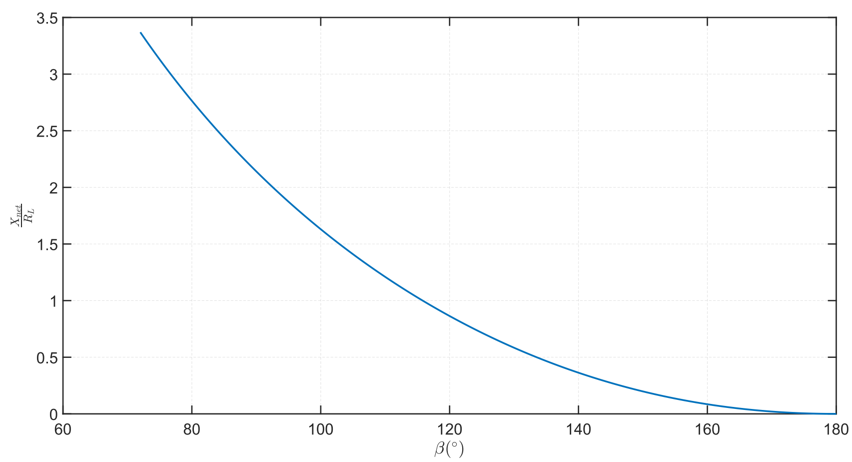

Figure 3-6: Required $\frac{X_{net}}{R_L}$, with respect to phase angle β for a desired transformation.

$$X_{net} = R_L \frac{2\beta \sin^2(\beta)}{\beta^2 - \sin^2(\beta)\cos^2(\beta) - \sin^4(\beta)} \tag{3.8}$$

3.2.2 Analyzing CTMN Control Equations

The control equations demonstrate the relationship between the phase control angle β, the impedance transformation $\frac{R_L}{Z_0}$ (Eqn. 3.7), and the necessary reactance X_{net} (Eqn. 3.8). Applying a specific phase control angle β achieves a target impedance transformation ratio of $\frac{R_L}{Z_0}$ while introducing a phase shift to the network, calculated by the net reactance X_{net}. Using Eqn. 3.7, this may be normalized to give a value of $\frac{X_{net}}{Z0}$:

$$\frac{X_{net}}{Z_0} = \frac{4}{\pi} \cdot \frac{\beta \sin^2(\beta)}{\beta^2 - \sin^2(\beta)\cos^2(\beta) - \sin^4(\beta)} \cdot \sqrt{\frac{\beta^2 + \sin^2(\beta) - 2\beta \sin(\beta)\cos(\beta)}{1 + [\frac{2\beta \sin^2(\beta)}{\beta^2 - \sin^2(\beta)\cos^2(\beta) - \sin^4(\beta)}]^2}} \cdot M\left(\beta, \tan^{-1}\left(\frac{-\sin^2(\beta)}{\beta + \sin(\beta)\cos(\beta)}\right)\right) \tag{3.9}$$

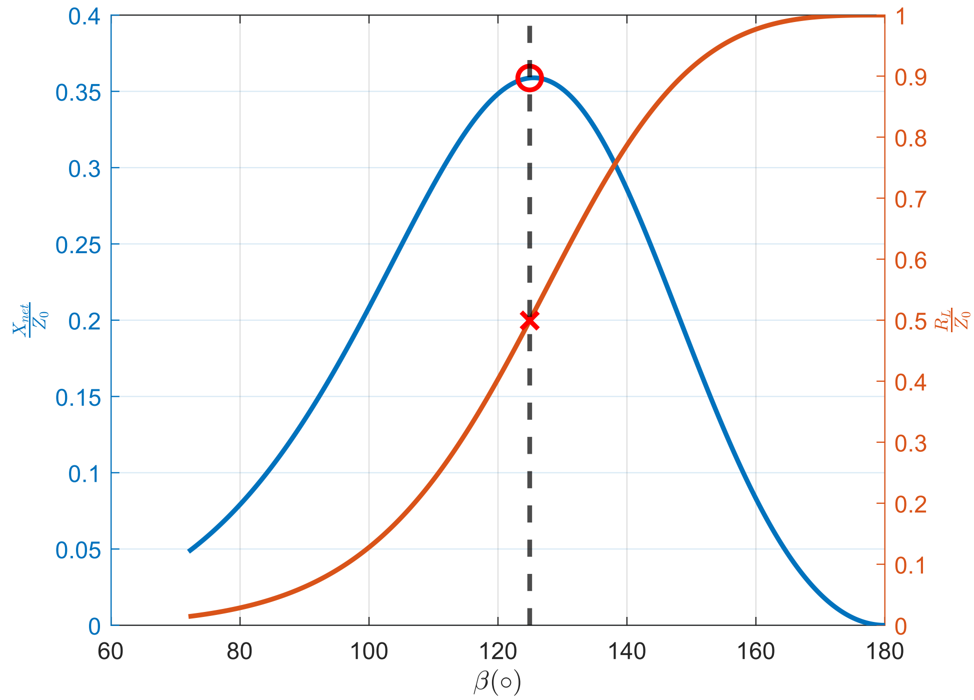

Figure 3-7: Selection of phase control angle β and the net reactance X_{net} normalized to Z_0, $\frac{X_{net}}{Z_0}$ for a desired transformation $\frac{R_L}{Z_0}$. The right-sided y axis represents a transformation ratio $\frac{R_L}{Z_0}$, and the left-sided y axis represents the normalized reactance $\frac{X_{net}}{Z_0}$ required for achieving that transformation. The x axis represents the operating phase angle β for this transformation-reactance pair. For example, for a target input impedance of $Z_0 = 50\Omega$, and a load resistance of $R_L = 25\Omega(\frac{R_L}{Z_0} = 0.5)$, we get a required β of $125°$ degrees and a required net reactance of 18Ω ($\frac{X_{net}}{Z_0} = 0.36$)
.

To match a load impedance R_L with a target input impedance Z_0, the required β and the necessary net reactance are determined by control equations, as depicted in Fig. 3-7. For instance, to achieve a transformation ratio of 0.5 for a target input impedance of $Z_0 = 50\,\Omega$ in our network (i.e., at $R_L = 25\Omega$), one operates at a beta (β) value of $125°$. Under these conditions, the network requires a normalized reactance $\frac{X_{net}}{Z_0}$ of 0.36 or approximately 18Ω of net reactance (X_{net}) to compensate for phase shift introduced by the CSN.

3.3 CTMN Design Overview

In this section, we provide an overview of the architecture of the CTMN and explain the design method for the variable elements in the network to achieve the desired impedance matching.

3.3.1 Ciruit Architecture

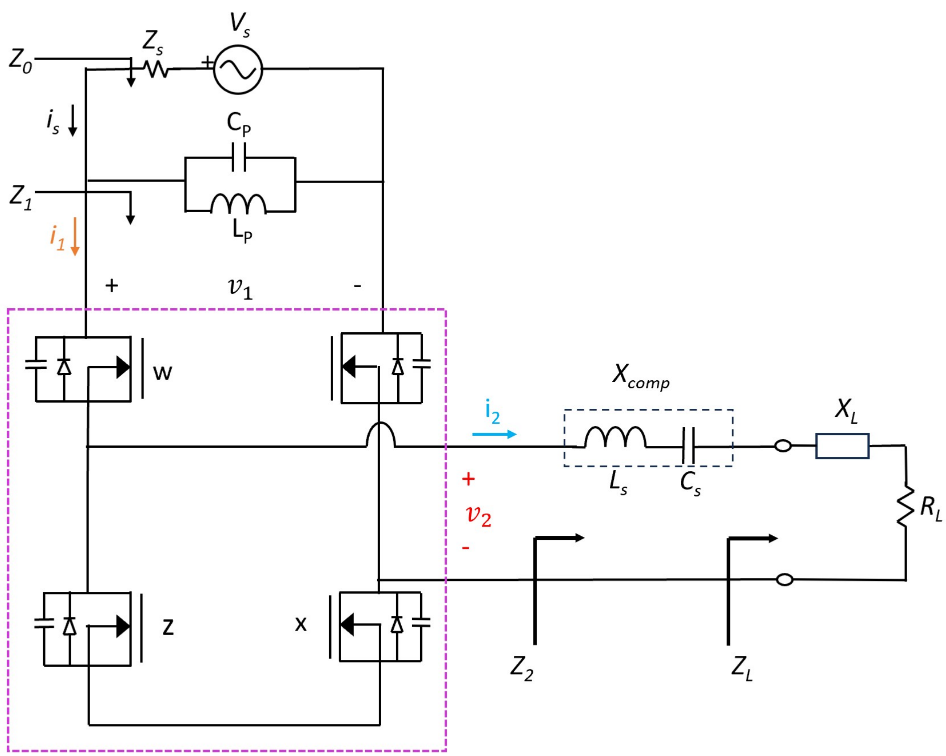

Figure 3-8: Circuit architecture of the controllable transformation matching network.

Figure 3-8 illustrates the CTMN architecture discussed in this thesis. A voltage source v_s, connected through a source impedance Z_s, represents the input to the system. The CTMN includes an input filter comprising a low-Q parallel-resonant tank (Lp-Cp); this serves to attenuate harmonic current components from the controllable switching network. For purposes of analysis in this thesis, we assume that the parallel tank appears approximately as an open circuit at the fundamental and do not consider it further. The input filter leads into the power stage, termed the controllable switching network. Z_1 represents the effective input impedance looking into the CSN at the fundamental frequency of operation (i.e., $\frac{\hat{v_1}}{\hat{i_1}}$). In series with the output port of the controllable switching network is the output series filter tank, comprising L_s and C_s provide tank reactance X_{comp}. Along with the load reactance X_L, X_{comp} constitutes the total output branch reactance $X_{comp}+X_L$. The output of the system is

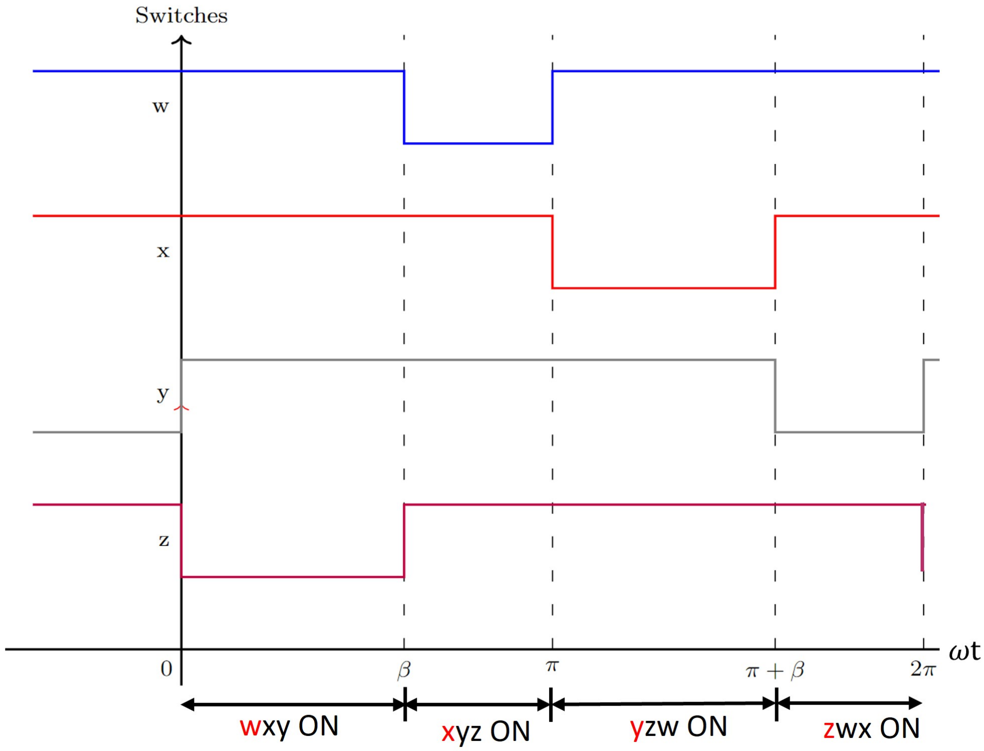

Figure 3-9: The switching sequence applied to the controllable transformation matching network.

characterized by the voltage v_2 and current i_2 across the output impedance $Z_2 = R_L + jX_{net}$. The system load is represented by $Z_L = R_L + jX_L$.

3.3.2 CTMN Operation

In the CTMN architecture, a switching sequence depicted in Fig. 3-9 is applied, controlled by the phase angle β, where we have neglected the deadtimes necessary in practice to achieve zero-voltage switching; these deadtimes will be considered later. This switching operation facilitates a step-down voltage transformation from the input voltage v_1 to the fundamental of the output voltage $\hat{v_2}$, and the resulting output impedance is given by $Z_2 = \frac{\hat{v_2}}{\hat{i_2}}$. The architecture's design allows the CSN to scale this output impedance, $Z_2 = R_L + jX_{net}$, to a higher effective fundamental-frequency input impedance, $Z_1 = R_1 + jX_1 = \frac{\hat{v_1}}{\hat{i_1}}$, where R_1 and X_1 represent the resistive and reactive input impedances, respectively. This transformation is a direct function of β and results in the creation of an additional effective reactance X_T within the switching network, as illustrated in Fig. 3-1.

In general, $Z_1 = R_1 + jX_1$, but we typically aim to target a specified resistive input impedance Z_0 (which we define as the characteristic impedance.) Thus, we would like to control the system to achieve $R_1 = Z_0$ and $X_1 = 0$. To accomplish this, X_{net} plays a key role in the system by counterbalancing the effect of X_T, essentially ensuring $X_{net} = -X_T$. This net reactance, X_{net}, is obtained by combining the output reactance X_L with the filter tank reactance X_{comp}. X_{comp} is referred to as the compensating reactance or the variable reactance in this thesis.

$$X_{net} = X_L + X_{comp} \tag{3.10}$$

For a desired transformation from a given load, the load reactance X_L is considered known. In order to achieve impedance matching to a desired input resistance Z_0, we need to select a frequency such that the output filter tank reactance X_{comp} and load reactance X_{net} combine to cancel the X_T generated by the CTMN. In the next sections, we explore design methods for the output tank and variable compensating reactance X_{comp}.

3.4 Selection of Compensating Reactance, X_{comp}

The output tank provides the compensating reactance, X_{comp}. With a high-Q series LC output filter, we can enforce nearly sinusoidal output current while introducing a reactance X_{comp} in series with the load network, with the value of X_{comp} adjustable by narrow-band frequency modulation.

3.4.1 Functionality of the Output Tank

In addition to reducing the harmonic content of the output current, the output filter in the CTMN architecture provides a reactance X_{comp}. The value of X_{comp} may be varied by narrow-band variation in the frequency of the rf source (i.e., by narrow-band frequency modulation, or FM). This technique, which relies on control of the rf source, is sometimes also known as dynamic frequency tuning (DFT). In this thesis, we primarily consider variations in the reactance of the output filter through DFT. In other designs, it could be realized through the use of variable effective filter components (e.g., the use of a variable vacuum capacitor or a network providing phase-switched impedance modulation [25, 41, 42].

The output tank of the CTMN, comprising the inductor L_s and capacitor C_s, is designed to operate at a variable angular frequency ω_{sw}. This variability in operating frequency is key to achieving a range of compensating reactances, X_{comp}, within the system. Specifically, by altering ω_{sw}, the tank can be tuned to provide different values of X_{comp}. As will be seen, X_{comp} is adjusted both to provide matching in the face of variable load reactances and to compensate for the reactive effects in the transformation provided by the controlled switching network.

3.4.2 Dynamic Frequency Tuning

Dynamic frequency tuning (DFT) refers to the process of adjusting the output tank's reactance through variations in the system operating frequency (i.e., the frequency of the input rf source, which is controlled in conjunction with the control of the CTMN). The angular frequency $\omega_{sw} = 2\pi f_{sw}$ is key to this process. As a result, the "compensating reactance" X_{comp} provided by the series Ls-Cs output filter tank can be expressed as:

$$X_{comp} = \omega_{sw} L_s - \frac{1}{\omega_{sw} C_s}. \tag{3.11}$$

This expression highlights that the reactance X_{comp} delivered by the tank is not static but dynamically modulated by the operating frequency ω_{sw}. Changes in the operating frequency directly impact the reactance produced by the series combination L_s and C_s, enabling the output tank to provide variable reactance levels for different operational requirements. A high Q network [49] allows significant reactance variations to be achieved with relatively small variations in angular operating frequency ω_{sw}.

3.4.3 Impact of Load Reactance, X_L

The compensating reactance, X_{comp}, is selected to achieve the net reactance X_{net} necessary to transform the load resistance R_L to the resistance Z_0 desired at the input of the CTMN. X_{comp} must compensate for both the load reactance X_L, and the effective reactance introduced by the controlled switching network X_T. Overall, we would like:

$$X_{comp} = -X_T - X_L \tag{3.12}$$

Lumping together the reactance X_{comp} of the Ls-Cs tank and the load network X_L as a net value X_{net} (see Fig. 3-4), we get the net reactance required for CTMN operation as calculated in Eqn 3.10 and Fig. 3-7:

$$X_{net} = X_{comp} + X_L = -X_T \tag{3.13}$$

Expressing the desired compensation reactance in scenarios with zero load reactance ($X_L = 0$), we get:

$$X_{comp} = X_{net} \tag{3.14}$$

This expression indicates that the output filter provides the entire net reactance. Conversely, with non-zero X_L, X_{comp} adjusts to:

$$X_{comp} = X_{net} - X_L \tag{3.15}$$

X_L contributes to the overall reactance of the load branch. Under these circumstances, the compensating reactance, X_{comp}, is effectively adjusted to compensate for the variance in X_L and for the effective reactance X_T introduced by the controlled switching network.

3.4.4 Selection of X_{comp} for a Range of Load Impedances

The compensation reactance X_{comp} provided by the output filter must be adjustable over a certain range to compensate for the reactance introduced by the controlled switching network X_T, which varies with the amount of transformation from the load resistance R_L up to the desired input resistance Z_0. The necessary value for X_{comp} to accomplish the task alone is referred to as X_{net}, as expressed in equations (3.6) normalized for Z_0 in equation 3.9 and Fig. 3-4. The range of X_{net} required for a given possible range in R_L might be designated as

$[X_{net,min}, X_{net,max}]$. X_{comp} must further provide sufficient adjustment range to null the load reactance X_L, which might vary over a range of $[X_{L,min}, X_{L,max}]$.

The design of the CTMN considers the ranges of R_L and X_L. The maximum and minimum values of X_{comp} that the output filter needs to provide are determined by the maximum and minimum values of X_{net} and X_L, as given by:

$$X_{comp,\min} = X_{net,\min} - X_{L,\max} \tag{3.16}$$

$$X_{comp,\max} = X_{net,\max} - X_{L,\min} \tag{3.17}$$

Consequently, the output filter's operation across different switching frequencies allows for achieving the necessary X_{comp} range based on the specific R_L and X_L ranges.

3.4.5 Selection of Operating Frequency Range

The system operates through dynamic frequency tuning, where the operating frequency f_{sw} varies to adapt to different values of load resistance $R_L$and load reactance X_L, which determine the desired value of compensating reactance X_{comp}. For a given range of X_{comp}, and output filter components L_s and C_s, the range for angular frequency ω_{sw} can be determined through the following equation:

$$\omega_{sw} = \frac{C_s X_{comp} + \sqrt{C_s^2 X_{comp}^2 + 4L_s C_s}}{2L_s C_s} \tag{3.18}$$

This equation is simply derived from Eqn. 4.21. With a known load, the required X_{comp} becomes a known quantity. Consequently, this equation enables us to calculate the specific switching frequency, ω_{sw}, needed to achieve the desired X_{comp} using the output filter designed in the next section. This approach ensures that the system's frequency tuning is precisely aligned with the operational requirements, thus optimizing the CTMN's performance under various load scenarios.

In practice, the load impedance $R_L + jX_L$ would be measured, and the values of β and ω_{sw} would be adaptively selected to provide the desired input match. The above value for ω_{sw} in Eqn. 3.18, however, gives a first-order selection about which adaptation can take place.

3.5 Selection of Series Output Filter Components L_s and C_s

Once the range of compensating reactance (X_{comp}) that must be provided by the output filter is established, we can proceed to select the inductor L_s and capacitor C_s to provide any variable reactance within that range. This design process involves selecting a range of operating frequencies, denoted as $[f_{sw,min}, f_{sw,max}]$, over which X_{comp} achieves the required degree of variation. (Here, we ignore any minor frequency dependency of the load reactance X_L, placing enough range in X_{comp} to account for such dependency.)

The frequency range translates into a corresponding angular frequency range, given by $\omega_{sw,min}$ to $\omega_{sw,max}$. Within this range, the output filter is capable of producing a range of variable reactance values for X_{comp}. Utilizing Eqn. 4.21, this relationship is mathematically represented as:

$$X_{comp,min} = \omega_{sw,min} L_s - \frac{1}{\omega_{sw,min} C_s} \tag{3.19}$$

and

$$X_{comp,max} = \omega_{sw,max} L_s - \frac{1}{\omega_{sw,max} C_s} \tag{3.20}$$

Together, Eqns. 3.19 and 3.20 enable the selection of L_s and C_s to provide the necessary tuning range of X_{comp} over the selected frequency range, accommodating the maximum and minimum reactance requirements. The values for L_s and C_s are calculated to ensure that the output filter can provide the necessary variable reactance within the specified range for a given switching frequency f_{sw}, where $\omega_{sw} = 2\pi f_{sw}$.

3.5.1 Series Inductor, L_s

The value of the output series inductor L_s is determined by balancing the maximum and minimum reactance requirements at the extremes of the switching frequency range. The equation for L_s is derived as follows:

$$L_s = \frac{X_{comp,max}\,\omega_{sw,max} - X_{comp,min}\,\omega_{sw,min}}{(\omega_{sw,max} - \omega_{sw,min})(\omega_{sw,max} + \omega_{sw,min})} \tag{3.21}$$

3.5.2 Series Capacitor, C_s

Similarly, the series capacitor C_S must be capable of handling the range of reactance values necessitated by the frequency range. The value of C_s is calculated to complement L_s, ensuring that the output filter can adapt to the necessary variable reactance within the given switching frequency range. The equation for C_s is as follows:

$$C_s = \frac{(\omega_{sw,max} - \omega_{sw,min})(\omega_{sw,max} + \omega_{sw,min})}{\omega_{sw,max}\,\omega_{sw,min}\,(X_{comp,max}\,\omega_{sw,min} - X_{comp,min}\,\omega_{sw,max})} \tag{3.22}$$

3.6 Design of Input Filter

The parallel input filter in the CTMN is to ensure that the voltage at the input of the controlled switching network remains approximately sinusoidal despite harmonic current content in i_1. The parallel L_pC_p filter network acts approximately as an open circuit at the fundamental and as a short circuit at harmonic frequencies, resulting in v_1 remaining approximately sinusoidal even if there is significant source impedance Z_s to the rf source feeding the CTMN. As we do not desire significant shunt reactance variations owing to the input filter over the operating frequency range, a relatively low-Q filter is selected, ensuring effective performance while simplifying the design process. The exact filter quality factor Q_p selected is a design variable that depends upon the degree of filtering of i_1 that is required and the degree of shunt susceptance variation that is allowable over the switching frequency range, but a quality factor Q_p in the range of 2-5 might be considered reasonable for many designs.

To achieve the desired effect, we would like the tank resonant frequency, denoted as

$$f_p = \frac{1}{2\pi L_p C_p} \tag{3.23}$$

to be very close to the operating frequency of the system, f_{sw}. Therefore, we select f_p to be at or close to the center of the range of the operating frequency.

3.6.1 Parallel Inductor, L_p

The design of the parallel inductor, L_p, is determined based on the requirement to resonate at the tank frequency. The inductance value of L_p is given by the following equation:

$$L_p = \frac{Z_0}{2\pi f_p Q_p} \tag{3.24}$$

where Q_p is the quality factor of the filter and Z_0 is the characteristic impedance that we would like the CTMN input impedance to achieve.

3.6.2 Parallel Capacitor, C_p

Similarly, the parallel capacitor, C_p, is designed to complement the inductor in achieving the desired resonance at the tank frequency. The capacitance value of C_p is calculated as follows:

$$C_p = \frac{Q_p}{2\pi f_p Z_0} \tag{3.25}$$

This equation ensures that C_p works in conjunction with L_p to maintain resonance at the resonant frequency f_p, which is close to f_{sw}.

3.7 Design Summary

Fig. 3-10 presents a flowchart that summarizes the design methodology for the CTMN, serving as a visual summary and guide for the design and systematic processes outlined in this chapter.

In the context of an ideal and lossless switching network, the CTMN depicted in Fig. 3-8 performs a step-up impedance transformation to match a resistive plus reactive load impedance to a higher input impedance Z_0. This is accomplished using the voltage-transforming properties of the controlled switching network and by using the output filter to provide a

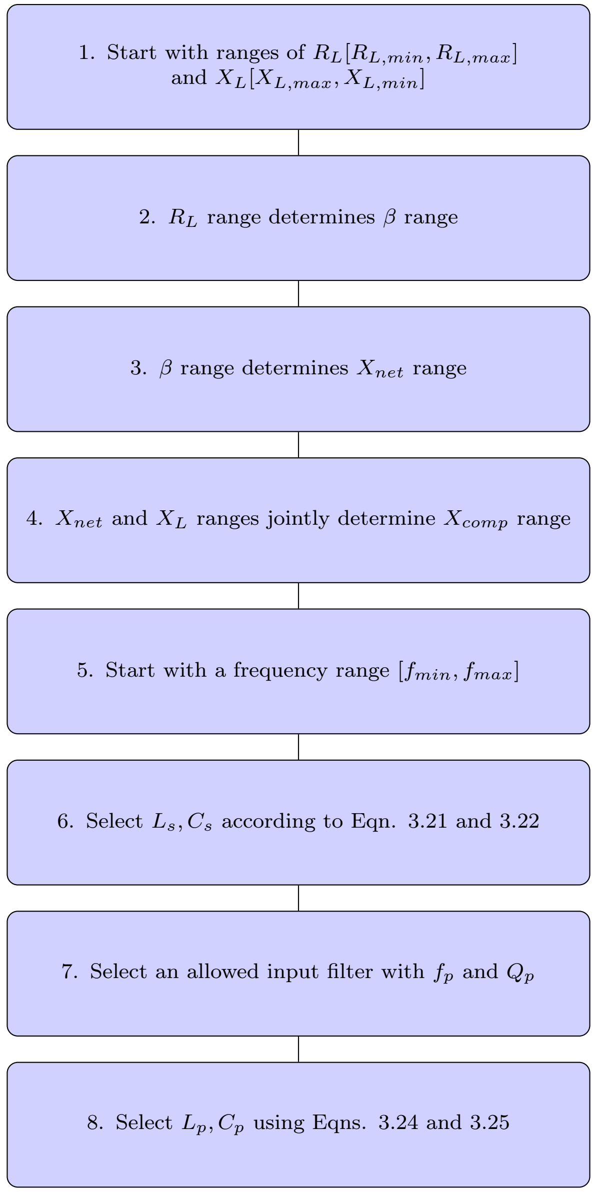

Figure 3-10: Design summary

controlled reactance. The output tank reactance is varied via dynamic frequency tuning to tune out the load reactance at resonance. At this point, the tank reactance, in conjunction with the load reactance, effectively cancels out the impact of the additional effective reactance introduced by the controlled switching network. With an appropriate switching control angle β and operating frequency ω_{sw}, the effective fundamental-frequency impedance looking into the switching network becomes Z_0 (transformed up from R_L). Furthermore, if we assume that the input filter is at resonance, the only impedance seen by the source is Z_0.

This configuration allows the CTMN to achieve a step-up transformation from R_L to a higher resistance value, denoted as Z_0. In essence, the CTMN functions like a tunable matching network, enabling the matching of a load represented by resistance R_L and reactance X_L to a higher input resistance value Z_0.

This chapter has provided a comprehensive overview of the key design elements and control parameters within the controllable transformation matching network (CTMN). The major points discussed include:

- Identification and analysis of variable elements within the CTMN.
- Modeling of critical control parameters, specifically β and f_{sw}.
- Detailed design methodologies for both the output and input tanks.

In the following chapter, we will take these theoretical concepts forward by designing a specific example of a CTMN. This design will be validated through a series of simulations, demonstrating the application of the principles discussed in this chapter.

Chapter 4

An Example Design for A 1kW Wide-Range Controllable Transformation Matching Network

In this chapter, we present an example design of a 13.56 MHz controllable transformation matching network (CTMN). This design aims to match load impedances ranging between $5\,\Omega$ and $20\,\Omega$ in resistance and $0\ \Omega$ to 15Ω in reactance, transforming them to a standard $50\,\Omega$ impedance for industrial applications. The switching network design utilizes a 4-switch network for impedance transformation as discussed in previous chapters, and the series LC output filter of the system realizes the secondary variable reactance, enabling dynamic frequency tuning (DFT) within a $\pm 5\%$ range around $13.56\,\mathrm{MHz}$ $[12.88\,\mathrm{MHz}, 14.24\,\mathrm{MHz}]$. The CTMN is designed to operate under conditions of 1 kW of input power at both the input and output; these conditions correspond to a peak ac voltage amplitude at the input of the matching network ($|V_1|$) of up to approximately 316 V and a 300 V input voltage. With a 13.56 MHz center frequency.

The findings and design details presented here rely on computational simulations performed in LTSpice. Although component choices, such as the MOSFET switch with an output parasitic capacitance value and a diode, are based on practically available switch parameters, these simulations remain untested against a physical prototype.

In the introductory section of this chapter, we discuss the parameter specifications for the design of the controllable transformation matching network. The subsequent sections detail the design methodologies for the input and output filter tanks and the selection of dynamic frequencies to achieve impedance matching.

4.1 Design Specifications of the CTMN

The controllable transformation matching network is designed based on the design method provided in the previous chapters of the thesis. Fig. 4-1 illustrates the detailed architecture of the CTMN designed in this thesis. In this section, we specify the ranges that are used in the design of the CTMN.

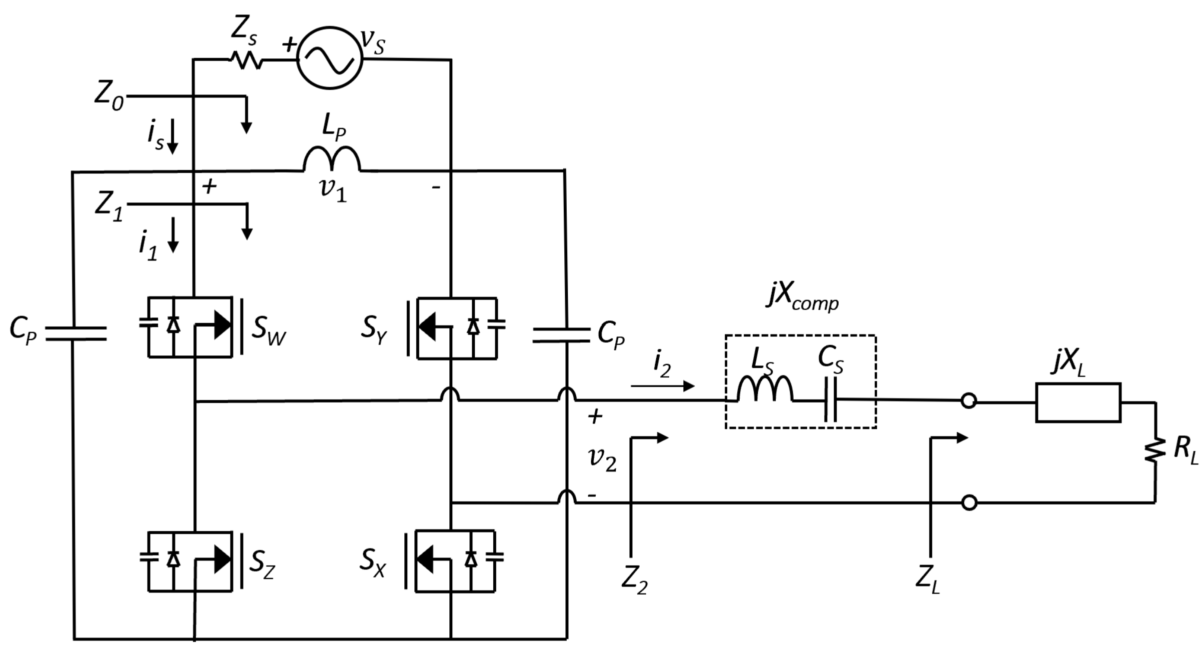

Figure 4-1: Detailed circuit architecture of the CTMN with design parameters.

4.1.1 Design Overview

The CTMN illustrated in Fig. 4-1 is composed of three main stages as illustrated in Fig. 2-18 (repeated here as Fig. 4-2):

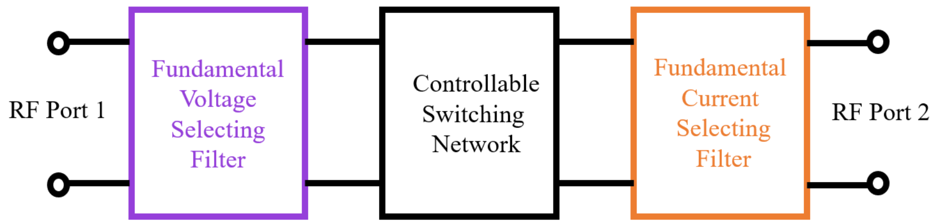

Figure 4-2: Block diagram of the CTMN system with fundamental voltage-selecting input filter, switching network and output filter stages.

- **Input Filter Stage:** The input filter stage functions as a fundamental voltage-selecting filter and consists of the parallel inductor L_p and the parallel capacitor C_p.
- **Switching Network:** This constitutes the power stage of the CTMN that performs the transformations. It is comprised of four switches, w, y, x and z as illustrated in Fig. 4-1. The switches operate at the operating frequency f_{sw} controlled by the phase control parameter β.
- **Output Filter Stage:** The fundamental-current-selecting output filter is a series combination of an inductor L_s and a capacitor C_s. This filter stage provides the variable reactance X_{comp}. The filter is connected with a load in series with resistance R_L and reactance X_L. The net reactance of the output branch is X_{net}.

These are the parameters of the CTMN that we are interested in designing. The results of this design are concisely summarized in Table 4.6.

4.1.2 Load Range, Z_L

We begin by selecting a load range for our design that needs to be matched to an input impedance of $Z_0 = 50\,\Omega$. In the matching network design, the load is represented by $Z_L = R_L + jX_L$. Based on the intended application, the resistive component of the load R_L is assumed to range from 5 Ω to 20 Ω (a 4X range). We also assume an inductive reactance, X_L that varies between 0 Ω and 15 Ω. The Smith chart in Fig. 4-3 illustrates the load range shaded in yellow, normalized to a $50,\Omega$ resistance. The CTMN converts any load within this specified range to a $Z_0 = 50\,\Omega$ load impedance, which corresponds to a normalized $Z_0 = 1$ on the Smith chart.

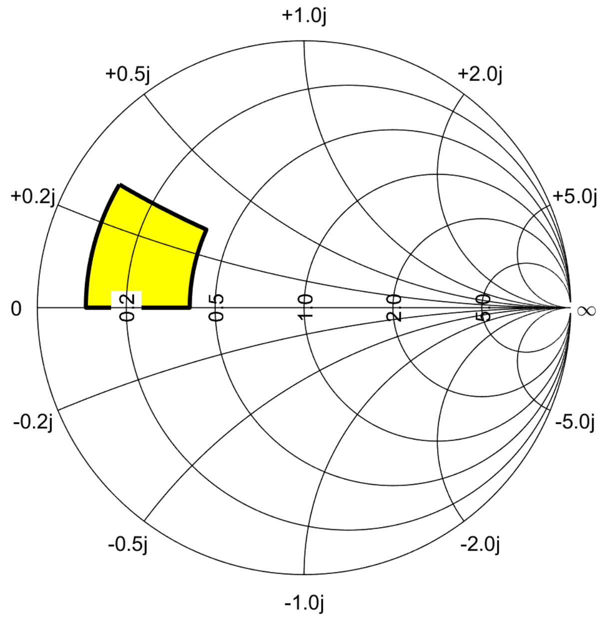

Figure 4-3: Smith chart showing the load range that can be matched to $Z_0 = 50\,\Omega$.

Table 4.1 illustrates a summary of the load range.

Load Impedance	Range (Ω)	Normalized Range
Resistance, $[R_{L,\min}, R_{L,\max}]$	[5, 20]	[0.1, 0.4]
Reactance, $[X_{L,\min}, X_{L,\max}]$	[0, 15]	[0, +0.3j]

Table 4.1: Selected range for load components

4.1.3 Phase Control Angle, β

As discussed in Chapter 3, the resistive component R_L of the load directly determines the range for the required phase control angle, β (see design summary in Fig. 3-10). Fig. 4-4 illustrates the required range of phase control angle β for an impedance transformation ratio of $\frac{R_L}{Z_0}$. Given the selected R_L range of $[5, 20]\,\Omega$, and a target input impedance $Z_0 = 50\Omega$, the controlled switching network must provide a transformation in resistance (impedance) $[0.1, 0.4]$, which falls within the achievable range of Fig. 4-4. The required range for the

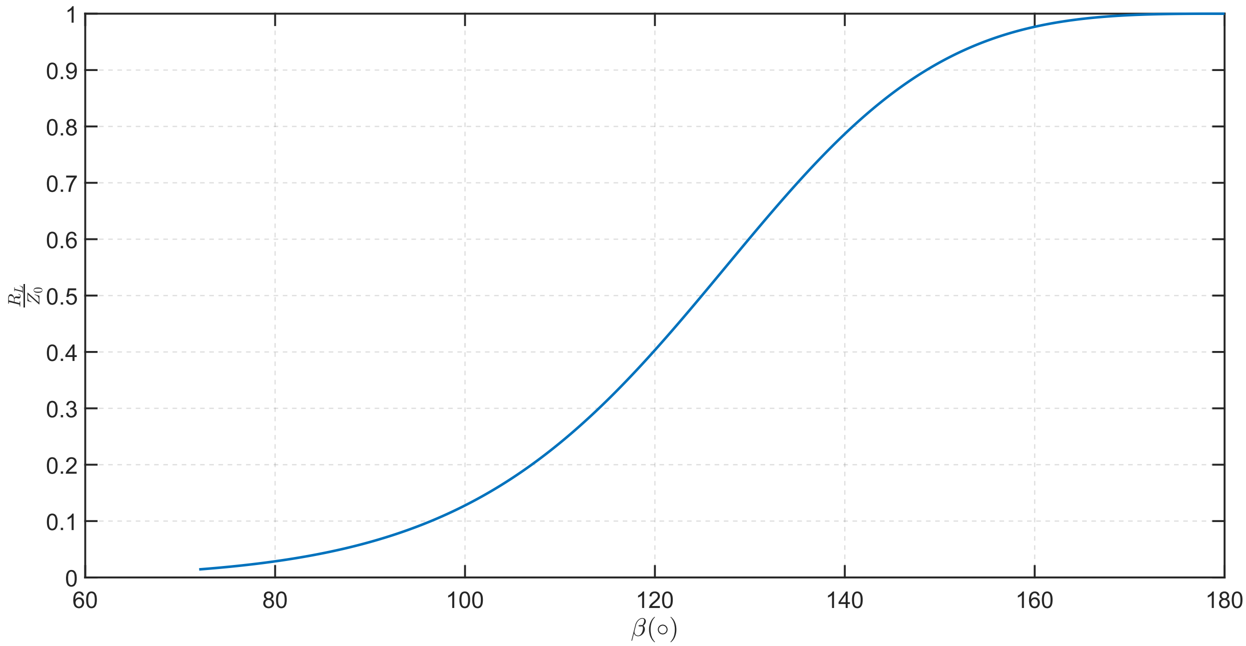

Figure 4-4: Selection of phase angle β for a desired transformation ratio of $\frac{R_L}{Z_0}$.

phase angle β to ensure impedance matching within this resistive load range is $[\beta_{min}, \beta_{max}] = [96.66°, 119.88°]$. The smallest (5 Ω) and largest (20 Ω) load resistances correspond to the lower (96.66°) and upper (119.88°) ends of the required phase angle, respectively. In essence, a higher resistance necessitates a larger phase angle to facilitate the desired impedance transformation. This is illustrated in Table 4.2. Note that the inductive component of the load impedance has no effect on the choice of β.

Load Resistance R_L	**Phase Control Angle β (°)**
$R_{L_{\min}} = 5\,\Omega$	$\beta_{\min} = 96.66°$
$R_{L_{\max}} = 20\,\Omega$	$\beta_{\max} = 119.88°$

Table 4.2: Desired Range for Phase Control Angle β for a given resistive load range R_L.

4.1.4 Net Reactance X_{net}

The phase control angle β determines the required net reactance X_{net} range. Since β is determined by the given resistive load R_L range, in other words, the given range for R_L

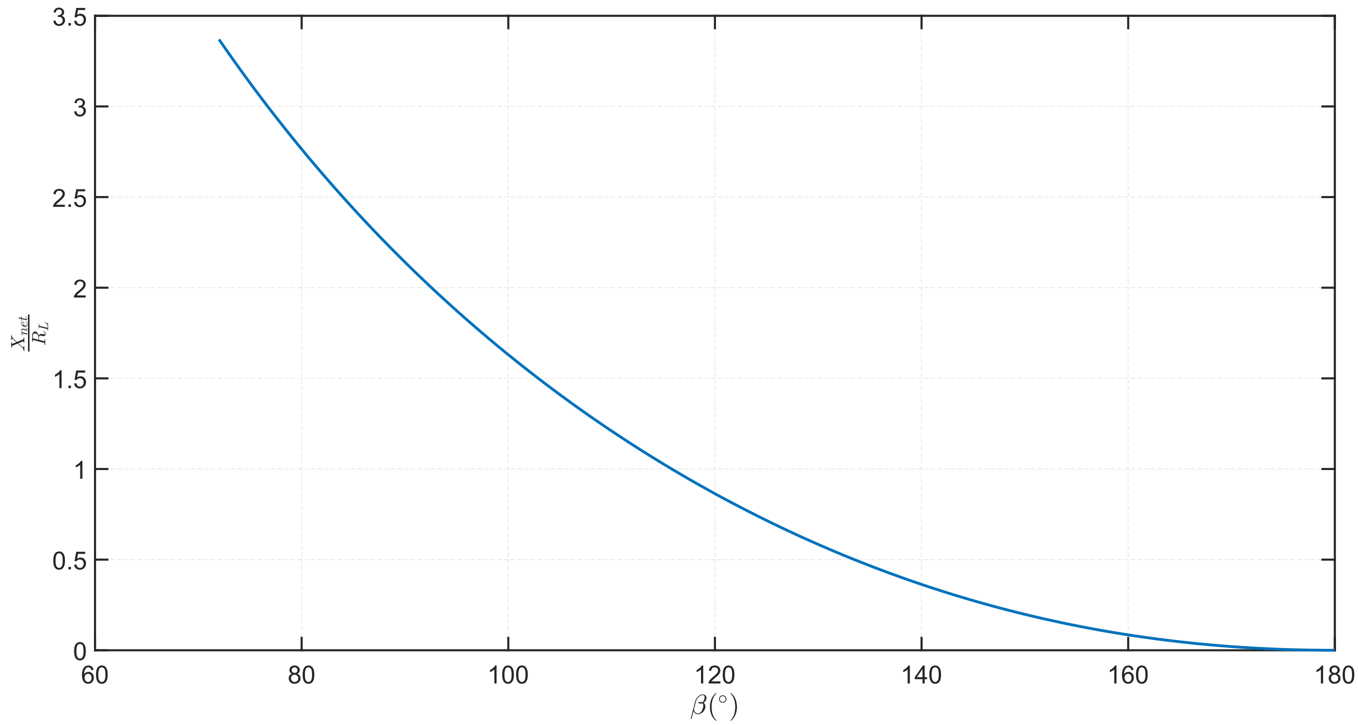

Figure 4-5: Required $\frac{X_{net}}{R_L}$, with respect to phase angle β for a desired transformation.

determines the range for X_{net}. From Table 4.2, the desired β range for our design is $[\beta_{min}, \beta_{max}] = [96.66°, 119.88°]$. This range yields the range for the required net reactance as $[X_{net,min}, X_{net,max}] = [8.95\Omega], 17.352\Omega]$, as seen in Fig. 4-5.

Phase Control Angle β (°)	X_{net} **Range**
$\beta_{\text{min}} = 96.66°$	$X_{net,max} = 17.352\Omega$
$\beta_{\text{max}} = 119.88°$	$X_{net,min} = 8.95\Omega$

Table 4.3: Net reactance X_{net} range.

4.1.5 Compensating Reactance, X_{comp}

The maximum and minimum values of X_{comp} that the output filter needs to provide are determined by the maximum and minimum values of X_{net} and X_L, as given by:

$$X_{comp,\min} = X_{net,\min} - X_{L,\max} \tag{4.1}$$

$$X_{comp,\max} = X_{net,\max} - X_{L,\min} \tag{4.2}$$

From Tables 4.1 and 4.3:

$$X_{net,\max} = 17.352\,\Omega \tag{4.3}$$

$$X_{net,\min} = 8.95\,\Omega \tag{4.4}$$

$$X_{L,\max} = 15\,\Omega \tag{4.5}$$

$$X_{L,\min} = 0\,\Omega \tag{4.6}$$

For the **minimum compensating reactance,** $X_{comp,min}$, subtract the maximum load reactance from the minimum net reactance:

$$X_{comp,\min} = X_{net,min} - X_{L,max} \tag{4.7}$$

$$= -6.05\,\Omega \tag{4.8}$$

For the **maximum compensating reactance,** $X_{comp,max}$, subtract the minimum load reactance from the maximum net reactance:

$$X_{comp,\max} = X_{net,max} - X_{L,min} \tag{4.9}$$

$$= 17.352\,\Omega \tag{4.10}$$

4.1.6 Operating Frequency, f_{sw}

The center frequency is set at 13.56 MHz, with a ±5% frequency modulation determining the operating range. This modulation results in frequency limits of $f_{min} = 12.880$ MHz and

Net Reactance $X_{net}(\Omega)$	**Load Reactance** $X_L(\Omega)$	**Compensating Reactance** $X_{comp}(\Omega)$
$X_{net,\max} = 17.352$	$X_{L,\min} = 0$	$X_{comp,\max} = 17.36$
$X_{net,\min} = 8.95$	$X_{L,\max} = 15$	$X_{comp,\min} = -6.05$

Table 4.4: Compensating reactance X_{comp} range.

$f_{max} = 14.238$ MHz as shown in Table 4.5. Over this frequency range, we must synthesize the necessary compensating reactance X_{comp} to provide the net reactance X_{net} to accommodate the 4X range resistive load range of [5,20] Ω and inductive reactive load range of $[0, 15]\,\Omega$ with matching to 50Ω. The details of how this is achieved is described in Section 4.2.

Operating Frequency	**Frequency (MHz)**
Minimum Frequency, f_{min}	12.880
Maximum Frequency, f_{max}	14.238

Table 4.5: Specified operating frequency range.

4.2 Output Filter Design

The output filter tank, consisting of L_s and C_s is designed to ensure that the current i_2 is dominated by its fundamental-frequency component. Furthermore, frequency modulation in the operating frequency f_{sw} (also known as dynamic frequency tuning (DFT)) is implemented such that the series $L_s - C_s$ tank generates a variable reactance X_{comp}. The $L_s - C_s$ tank components are selected so that the tank can produce a range of reactance values X_{comp} to achieve the desired net reactance (between X_{comp} and X_L) necessary for the desired impedance match within the narrow frequency modulation range. The selection approach below follows the development in Section 3.5.

Design Parameter	Parameter Value
$R_{L,\min}$	$5\,\Omega$
$R_{L,\max}$	$20\,\Omega$
$X_{L,\min}$	$0\,\Omega$
$X_{L,\max}$	$15\,\Omega$
$\beta_{\min}$	$96.66°$
$\beta_{\max}$	$119.88°$
$X_{net,\min}$	$8.95\,\Omega$
$X_{net,\max}$	$17.352\,\Omega$
$X_{comp,\min}$	$-6.05\,\Omega$
$X_{comp,\max}$	$17.36\,\Omega$
$f_{sw,\min}$	12.88 MHz
$f_{sw,\max}$	14.238 MHz
$\omega_{sw,\min}$	$2\pi \times 12.88$ rad/s
$\omega_{sw,\max}$	$2\pi \times 14.238$ rad/s

Table 4.6: Design specifications for CTMN parameters

new paragraph. The tank resonant frequency is $f_{r,series}$. The resonant frequency for the series LC tank can be determined using the following formula:

$$f_{r,series} = \frac{1}{2\pi\sqrt{L_s C_s}} \tag{4.11}$$

4.2.1 Series Inductor, L_s

The equation for L_s is derived as follows:

$$L_s = \frac{X_{comp,max}\,\omega_{sw,max} - X_{comp,min}\,\omega_{sw,min}}{(\omega_{sw,max} - \omega_{sw,min})(\omega_{sw,max} + \omega_{sw,min})} \tag{4.12}$$

Plugging in the values from Table 4.6, we obtain:

$$L_s = 1.41\,\mu H \tag{4.13}$$

4.2.2 Series Capacitor, C_s

Similarly, by utilizing the values from Table 4.6, we can calculate the series tank capacitance:

$$C_s = \frac{(\omega_{sw,max} - \omega_{sw,min})(\omega_{sw,max} + \omega_{sw,min})}{\omega_{sw,max}\, \omega_{sw,min}\, (X_{comp,max}\, \omega_{sw,min} - X_{comp,min}\, \omega_{sw,max})} \tag{4.14}$$

$$C_s = 103\, pF \tag{4.15}$$

4.2.3 Output Tank Resonant Frequency, $f_{r,series}$

The tank resonant frequency for the series LC tank is therefore:

$$f_{r,series} \approx 13.207\,\mathrm{MHz}$$

4.3 Input Filter Design

The input filter, consisting of L_p and C_p as illustrated in Fig. 4-1, operates to ensure that the voltage v_1 is dominated by its fundamental-frequency component (at f_{sw}). It also ensures that harmonic currents are shunted such that the current drawn from the input source is dominated by its fundamental. As discussed in Section 3.7, we have selected a relatively low quality factor (Q_p) of 7 (where we define $Q_p = Z_0/\sqrt{(L_p/C_p)}$) and set the resonant tank frequency f_p to 14.238 MHz , which is closely aligned with the operating frequency of our system (f_{sw}). The input filter is designed to resonate at the upper frequency boundary ($f_{sw,\mathrm{max}}$) of our switching frequency range. A quality factor (Q_p) of 7 is adopted for both design and simulation purposes, aiming to minimize the shunt reactive loading it represents over a ±5% variation in the operating frequency.

For the determination of the tank components, the objective is to configure L_p and C_p to resonate at a frequency of f_p = 14.238 MHz, with a loaded tank quality factor (Q_p) set to 7. The target impedance for the parallel tank is specified to be $Z_0 = 50\,\Omega$ while the characteristic impedance of the parallel tank is $Z_p = \sqrt{L_p/C_p}$, and the loaded tank quality factor is $Q_p = Z_0/Z_p$.

4.3.1 Input Tank Resonant Frequency, f_p

The input tank resonant frequency is calculated using the equation provided below:

$$f_p = \frac{1}{(2\pi\sqrt{(L_p\,C_p)}} \tag{4.16}$$

4.3.2 Parallel Inductor, L_p

For a parallel resonant tank circuit consisting of an inductor L_p and a capacitor C_p, the inductance L_p is determined by the tank's characteristic impedance Z_p, resonant frequency f_p, and quality factor Q_p. This relationship is expressed as follows:

$$L_p = \frac{Z_0}{2\pi f_p Q_p} \tag{4.17}$$

With the given values for our design, including $Z_0 = 50\,\Omega$, $f_p = 14.238\,\text{MHz}$, and $Q_p = 7$, we can proceed with the calculations:

$$L_p = \frac{50}{2\pi(12.88 \times 10^6)(7)} \approx 79.84\,nH \tag{4.18}$$

4.3.3 Parallel Capacitor, C_p

In the same parallel resonant tank circuit, the capacitance C_p is also linked to the resonant frequency f_p, quality factor Q_p, and the tank's characteristic impedance Z_0. The calculation for determining the capacitance C_p is as follows:

$$C_p = \frac{Q_p}{2\pi f_p Z_0} \tag{4.19}$$

With the provided values designed for the CTMN:

$$C_p = \frac{7}{2\pi(14.238 \times 10^6)(50)} \approx 1.56\,nF \tag{4.20}$$

4.4 Operating Frequency Selection for a Given Load, Z_L

The CTMN illustrated in Fig. 4-1 operates at a variable angular frequency ω_{sw} within a defined range as provided in Table 4.5. As a result, the reactance X_{comp} provided by the series Ls-Cs output filter tank can be expressed as:

$$X_{comp} = \omega_{sw} L_s - \frac{1}{\omega_{sw} C_s}. \tag{4.21}$$

Given L_s, C_s and the compensating reactance, X_{comp}, the system operating frequency ω_{sw} can be determined by using the equation:

$$\omega_{sw} = \frac{C_s X_{comp} + \sqrt{C_s^2 X_{comp}^2 + 4 L_s C_s}}{2 L_s C_s} \tag{4.22}$$

$$f_{sw} = \frac{\omega_{sw}}{2\pi} \tag{4.23}$$

As indicated in Table 4.4, the system operates across a range of frequencies to maintain a range of compensating reactance X_{comp} for the design purpose of our CTMN. The CTMN needs to operate at a specific frequency to produce the required value of X_{comp} necessary for a desired impedance matching, given a certain combination of X_{net} and X_L. Thus, there is a unique operating frequency f_{sw} at which the CTMN must operate to achieve a specific impedance match from $Z_L = R_L + jX_L$. This relationship is illustrated in Fig. 4-6.

By integrating the results from Equations 3.7 and 3.8, as well as Figures 3-5 and 3-6, we can determine the operating frequency f_{sw} for any load within the specified range. This is further illustrated in Figure 4-6. For instance, table 4.7 shows examples of switching frequencies for five example load impedances. This aligns with the explanation in Section 4.1.5 that the minimum switching frequency is required to synthesize the smallest load resistance and the highest load inductance, and vice versa.

Next, we will simulate this example design of the CTMN using LTSpice, aiming to validate the design and assess the functionality of the CTMN.

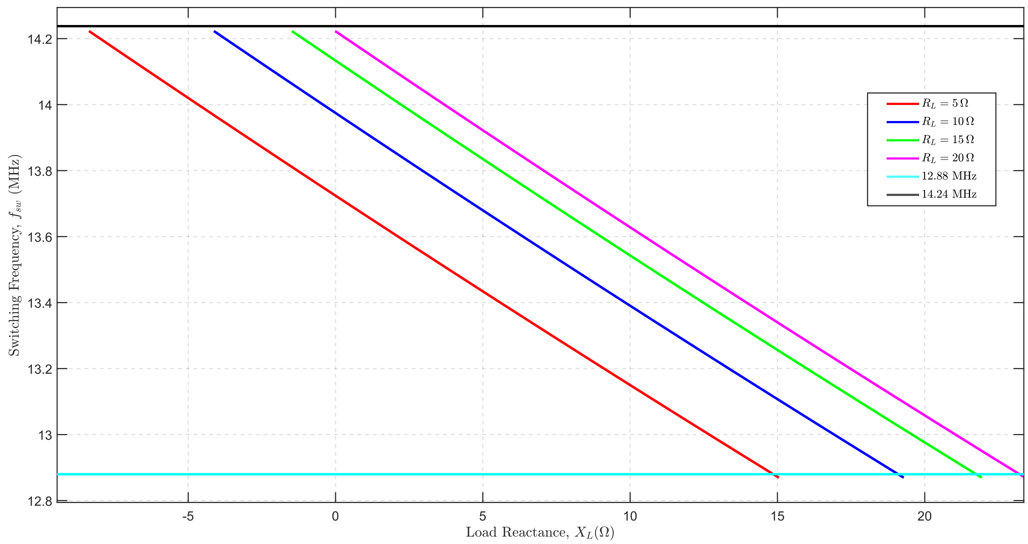

Figure 4-6: Example of frequency selection for given inductive loads. The horizontal boundary lines in cyan and black indicate the operating frequency range, which lies between 12.88 MHz and 14.24 MHz. This range represents a ±5 % deviation around a 13.56 MHz center frequency.

Load Impedance ($Z_L = R_L + jX_L$)	Operating Frequency (f_{sw})
$5 + j0\,\Omega$	13.724029
$20 + j0\,\Omega$	14.222263
$5 + j15\,\Omega$	12.872056
$20 + j20\,\Omega$	13.058086
$15 + j15\,\Omega$	13.256467

Table 4.7: Operating Frequencies for Different Load Impedances

4.5 Simulation Verification: Ideal Model

Employing the previously developed CTMN example, Sections 4.5 and 4.6 present LTSpice simulations to demonstrate the CTMN's capability in voltage and current transformations, as well as its ability to perform impedance matching between its input and output ports. In section 4.5, we present results for idealized designs (e.g., where device parasitics and other elements are not included), and in section 4.6, we include practical characteristics such as device parasitics and deadtimes. As will be seen, the simulated circuit waveforms verify that the CTMN design can achieve a step-up impedance matching from a load impedance $Z_L = R_L + jX_L$ having a small resistive component R_L to a resistive input impedance Z_{in} having a higher value resistance $Z_s = 50\,\Omega$ within the specified ranges. The CTMN

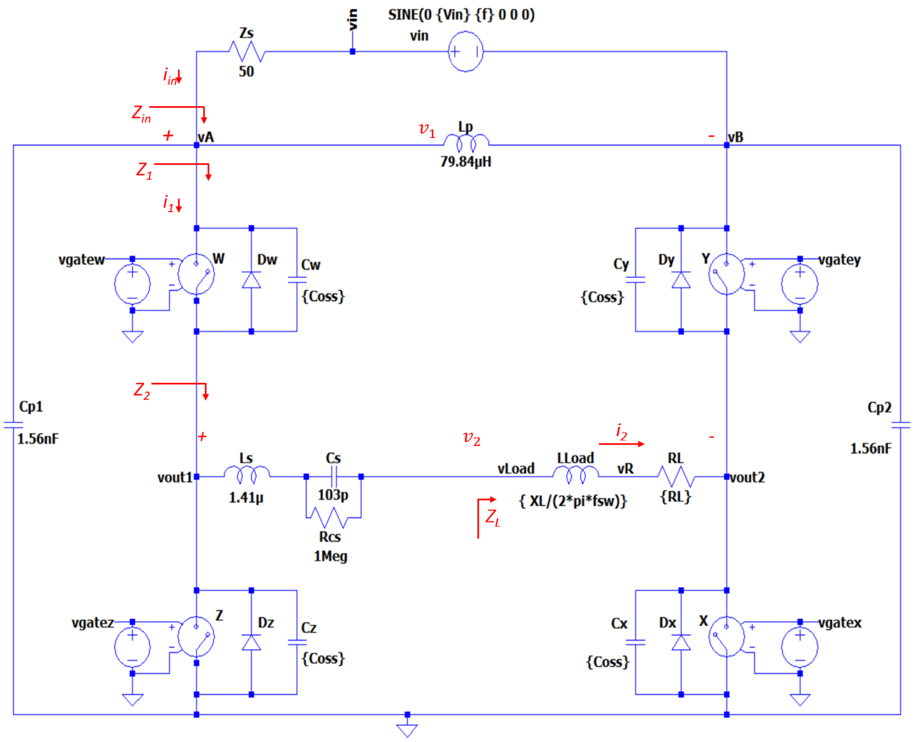

Figure 4-7: Overview of the CTMN schematic for the simulation.

is driven with a differential input from a Thevenin source comprising a sine wave source voltage v_{in} (V(vin,vB)), having a peak amplitude $V_{in} = 628.32$ V and frequency f, and a source impedance of $Z_s = 50\,\Omega$; this is intended as a test signal for the CTMN, simulating practical input conditions like that from an rf power amplifier. For the simulation, the input signal's frequency is set to match the CTMN's operating frequency, f_{sw}, with the CTMN switching locked in phase with the input source.

4.5.1 Idealized Operating Conditions

During the idealized operation of the CTMN, we assume perfect operational conditions for the circuit components and neglect the influence of device non-idealities and switch dynamics. Specifically:

- The active switches are considered to have ideal characteristics. This implies they have instantaneous on-and-off transitions and negligible dead times, as illustrated in Table 4.8. The idealized control sequence for the switches is illustrated in Fig. 4-8.

Switch Dynamics	Symbol	Value
Rise time	t_r	0.01n (negligible)
Fall time	t_f	0.01n (negligible)
Dead time	t_{dead}	0.01n (negligible)
Switch capacitance	C_{oss}	0.1pF

Table 4.8: Switch parameters used in idealized control signals.

- Intrinsic elements like switch capacitances (C_{oss}) of the switches are considered negligible. This assumption is based on their relatively small magnitudes ($C_{oss} = 0.1\,pF$), which have a minimal impact on the ideal simulation.

- The source signal v_s is characterized by a fixed frequency f and peak voltage V_{in}. In the simulation, f is set to match the switching frequency $f = f_{sw}$ with the CTMN operated in phase with the input signal, although in practical scenarios, these frequencies and phases might not be the same under transient conditions. Synchronizing the source and switching frequencies and phases in such cases is a consideration not covered in this thesis.

Further details and exceptions to this assumption are addressed in the discussion of practical-case scenarios in Subsection 4.6.

4.5.2 Component Specifications

For simulating the CTMN, we utilized the LTSpice simulation software. Figure 4-7 provides an example schematic of the CTMN as configured for the simulations in LTSpice. The corresponding LTSpice netlist for this model using 'idealized' parameters can be found in Appendix D.1.

The input tank components, inductor L_p and capacitor C_p, are selected based on the design procedure outlined in Section 4.3.

$$L_p = 79.84\,\text{nH}, \quad C_p = 1.56\,\text{nF}$$

The tank resonant frequency $f_p = 14.238$ MHz, a tank characteristic impedance $Z_p = \sqrt{L_p/C_p} = 7.15\Omega$, which gives a quality factor $Q_p = 7$ when loaded with the source impedance, a characteristic impedance $Z_s = 50\,\Omega$. In the schematic, the parallel capacitor C_p is replicated as C_{p1} and C_{p2} with one of the two in use in a given switch state. The output tank components, L_s and C_s, values are calculated in Eqns. 4.13 and 4.15:

$$L_s = 1.41\,\mu\text{H}, \quad C_s = 103\,\text{pF}$$

Parallel input tank	**Symbol**	**Values**
Inductor	L_p	79.84 nH
Capacitor	C_p	1.56nF
Characteristic impedance	Z_p	7.15
Q-factor	Q_p	7
Replicated capacitance	C_{p2}	0.1pF
Resonant frequency	f_p	14.238 MHz

Table 4.9: Parallel input tank parameters for LTSpice model.

The load is dynamically modeled as a series combination of a resistor R_L and an inductor L_{Load} whose value is determined by the switching frequency f_{sw} and a specified fundamental-frequency reactance X_L, with R_L and X_L as predefined inputs. The load inductance L_{Load} is calculated using the given X_L and the designed operating frequency f_{sw} per the following equation:

$$L_{Load} = \frac{X_L}{2\pi f_{sw}} \tag{4.24}$$

In the idealized example simulations presented here, the load parameters were set to $R_L = 20\Omega$ and $X_L = 0\Omega$. They define the control parameters as β and f_{sw}. Utilizing the MATLAB script provided in Appendix C, the calculated parameters are $f_{sw} = 14.2263$ MHz and $\beta = 119.88$ degrees. The system parameters used in the example are summarized in

Series output tank	**Symbol**	**Values**
Inductor	L_s	1.41 μH
Capacitor	C_s	103 pF
Resonant frequency	f_s	13.207 MHz

Table 4.10: Series output tank parameters for LTSpice model.

Table 4.11.

System Parameter	Symbol	Values
Load resistance	R_L	$20\,\Omega$
Load reactance	X_L	$0\,\Omega$
Load inductance	L_{Load}	0 μH
Phase control angle	β	119.88°
Switching frequency	f_{sw}	14.2263 MHz

Table 4.11: Example load parameters for LTSpice model.

The four switches W, X, Y and Z are modeled as voltage-controlled switches using the LTSpice switch model, detailed in Appendix D.1. Switch parameters are on-resistance (R_{on}), off-resistance (R_{off}), trip voltage (V_t), and hysteresis voltage (V_h). The switch model also includes an intrinsic body diode (D). The simulations also allow for a switch output capacitance C_{oss}. In the ideal simulations, C_{oss} is very small which can be assumed to have negligible effects on the simulation. The switch parameters for the ideal LTSpice model are illustrated in Table 4.12.

Parasitics	**Symbol**	**Values**
Output Capacitance	C_{oss}	0.1pF
Parameters	**Symbol**	**Values**
Drain-source on-state resistance	R_{on}	$22\,\text{m}\Omega$
Off-state resistance	R_{off}	$1\,\text{M}\Omega$
Trip voltage	V_t	2.5 V
Hysteresis voltage	V_h	2.5 V
Body Diode (D)	**Symbol**	**Values**
Off resistance	R_{off}	$1\,\text{M}\Omega$
Forward bias voltage	V_{fwd}	1.7 V

Table 4.12: Switch parameters for ideal simulation model of the CTMN.

Source Signals	Notation
Source voltage	v_{in}
Source Current	i_{in}
Source impedance	z_s
Resistive input impedance	Z_{in}
Switching Network Waveforms	**Notation**
Input voltage	$v_1 = v_A - v_B$
Output voltage (transformed)	$v_2 = v_{out1} - v_{out2}$
Output current	$i_2 = i_{R_{Load}}$
Input current (transformed)	i_1
Output impedance	Z_2
Load impedance	Z_L
Input impedance (transformed)	Z_1

Table 4.13: Waveform and signal label notations used in the ideal CTMN simulation.

4.5.3 Input Impedance Measurement Methodology

We use the specified components in the ideal LTSpice model illustrated in Fig. 4-7. The source signal v_s with a resistance $Z_s = 50\Omega$ is filtered by the input filter tank $L_p - C_p$. The filtered input voltage v_1 (represented as $v_A - v_B$ in the waveforms) is processed through the switching network, resulting in the output voltage $v_2 = v_{out1} - v_{out2}$. $v_2 = v_{out1} - v_{out2}$ is the voltage applied across the load branch , and $i_2 = i_{R_{Load}}$ represents the current through this branch. The output tank, comprising $L_s - C_s$, filters the output current i_2. i_1 and Z_1 are the input current and input impedance observed by the input source, respectively. The components and parameters utilized in the LTSpice model are detailed in Table 4.13.

Once the source signal is implemented in the CTMN with a given load impedance $Z_L = R_L + jX_L$, the switches in the network are governed by control signals, which are defined by the two control parameters β and f_{sw}. In our simulations, control signals are represented as pulsed voltage sources, details of which will be illustrated in the subsequent figures.

The analysis of the simulated voltage and current waveforms for both ideal and practical scenarios indicates that the output voltage $v_{out1} - v_{out2}$ is effectively a phase-modulated waveform with respect to the input $v_A - v_B$, governed by the control angle β. β has a direct effect on the duration of modulation within each cycle, which supports the function of the phase control mechanism in the CTMN. The analysis highlights a significant reduction in the fundamental component of the output voltage, indicating a successful step-down voltage transformation. A step-up current transformation occurs when the fundamental component of the output current increases in relation to the input current. Figures 4-13 and 4-18 exemplify these transformations through the waveforms during the switching intervals. Here, the CTMN adeptly modulates the input voltage $v_A - v_B$ into the output voltage $v_{out1} - v_{out2}$, as dictated by β.

In order to perform impedance calculations in the LTSpice environment, it is necessary to measure the current through and voltage across the targeted components. By employing Fourier analysis, the fundamental waveform components are isolated, which provide the basis for further calculations. In order to determine the magnitude and phase of the fundamental component of an impedance, the essential step is to divide the fundamental-component magnitudes of the associated voltage and current waveforms and then compare their phase angles.

For measuring the input impedance Z_{in} seen by the source , we utilize LTSpice to extract the fundamental components of the magnitudes and phases of the input voltage v_{in} and input current i_{in} by performing Fourier analysis on their simulated waveforms $V(\mathrm{vin}, \mathrm{vB})$ and $I(\mathrm{Zs})$, respectively. One way to implement this method is to use the `.four` command, as shown below:

```
.four f_{sw} 1 1 V(vin.vB) FROM {STTRIG} TO {ENDTRIG}
```

This command provides the magnitude and phase components of the waveform $V(\mathrm{vin}, \mathrm{vB})$ with a fundamental frequency of f_{sw} over one switching cycle.

```
.four {switching frequency} {Number of periods} {harmonic number}

waveform of interest {starting time} to {end time}
```

Once we have the results, we divide the fundamental component of the voltage magnitude $|v_{\mathrm{in}}|$ by that of the current magnitude $|i_{\mathrm{in}}|$. This gives us the magnitude $|z_{\mathrm{in}}|$ of the fundamental component of the input impedance z_{in}. Similarly, by dividing the fundamental component of the voltage phase $\angle v_{\text{in}}$ by that of the current phase $\angle i_{\text{in}}$, we obtain the phase $\angle z_{\text{in}}$ of the fundamental component of the input impedance.

We can use the magnitude $|z_{\text{in}}|$ and phase $\angle z_{\text{in}}$ to calculate the resistive R_{in} and the reactive X_{in} components of the input impedance Z_{in}, where:

$$R_{\text{in}} = |z_{\text{in}}| \cos(\angle z_{\text{in}})$$
$$X_{\text{in}} = |z_{\text{in}}| \sin(\angle z_{\text{in}})$$

Then we measure the input impedance z_{in} using the equation below:

$$z_{\text{in}} = R_{\text{in}} + jX_{\text{in}}$$

In our analysis, we are primarily interested in the resistive component of the input impedance z_{in}, which is R_{in} in our calculations.

4.5.4 Control Signals

The idealized control signals for the switches, governed by the phase control angle β, are considered to be perfectly timed and accurate with assumptions as summarized in Table 4.8. The switch control signals defined by these assumptions are illustrated in Fig. 4-8. A 'high' level indicates the switch is in an on state, while a 'low' level indicates it is in an off state. These signals are considered ideal because they ignore a practical switch's rise and fall times and dead times. The occurrence of $\beta = 119.88°$ is at $t = 23.239$ ns, with a period T of 70 ns and a frequency f_{sw} of 14.2263 MHz.

4.5.5 Results

The CTMN, as illustrated in Fig. 4-7, operates using an input signal $v_1 = v_A - v_B$ (refer to Fig. 4-9), which is subjected to controlled switching. This switching process is governed by the control sequences shown in Fig. 4-8. As a result of this switching, an output voltage

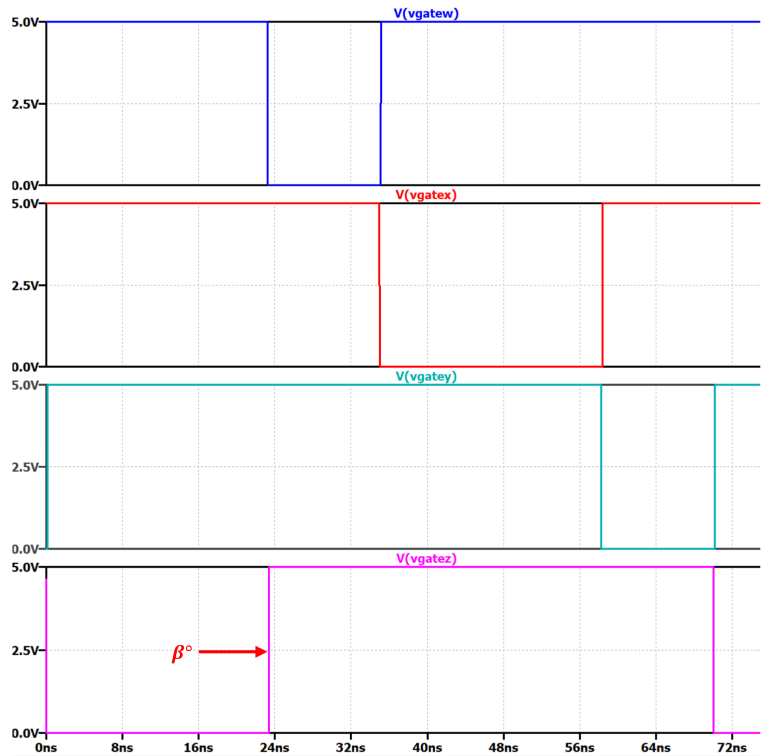

Figure 4-8: Ideal control sequences of the CTMN. A 'high' level indicates that a corresponding switch is on, while a 'low' level indicates that it is off. The switch timings and the equivalent non-zero duration $t = 23.24$ ns are controlled by the phase angle $\beta = 119.88°$. The switching frequency $f_{sw} = 14.2263$ defines the period (T=70 ns in this example) of the switching cycle.

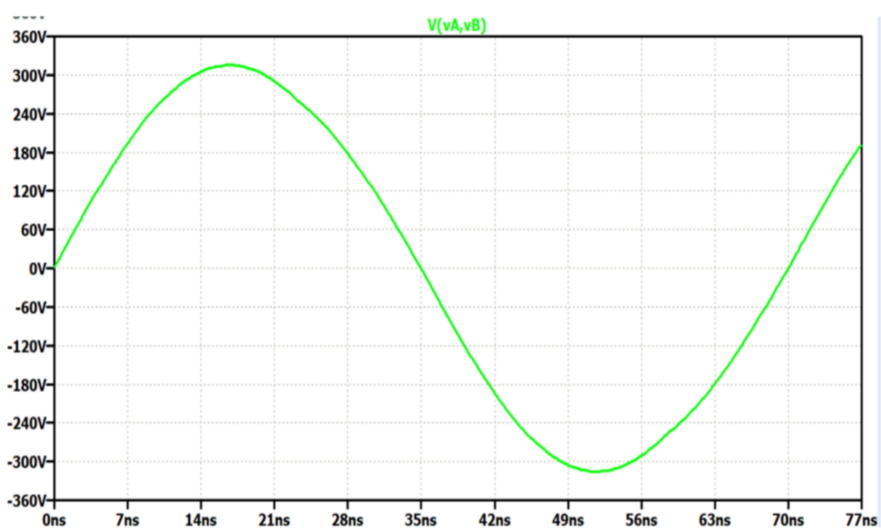

Figure 4-9: Input voltage waveform v_1 entering the switching network.

waveform $v_2 = v_{out1} - v_{out2}$ is produced, as depicted in Fig. 4-10. The output current i_2 and the input current i_1 waveforms are illustrated in Figs. 4-11 and 4-12.

Fourier analysis was conducted on the waveforms presented in Fig. 4-13, focusing on

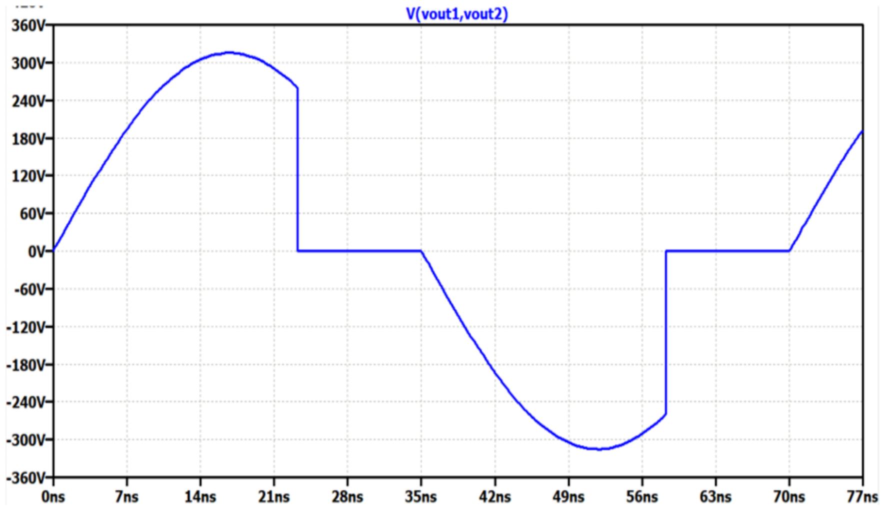

Figure 4-10: Output voltage waveform v_2 after a phase-controlled transformation with $\beta = 119.88°$.

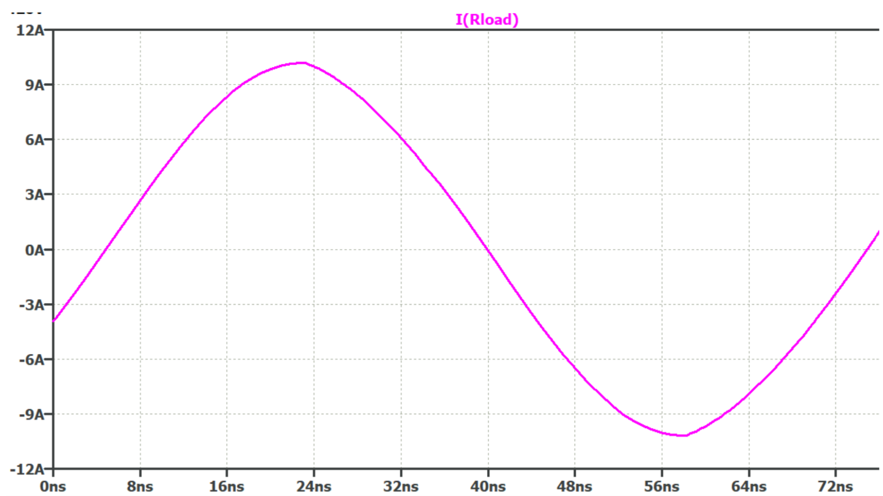

Figure 4-11: Output Current waveform i_2 loading an output impedance $Z_L = 20 + j0\,\Omega$.

extracting the fundamental components to understand the circuit's transformation behavior. The analysis showed that the fundamental frequency component of v_1 had a magnitude of 314.2 V and a phase angle of 88.51°, whereas that of v_2 exhibited a magnitude of 266.2 V and a phase angle of 72.27°. Similarly, the fundamentals of the source current i_s and load current $i_{L\mathrm{Load}}$ were found to have magnitudes of 6.267 A and 9.808 A, respectively, with corresponding phase angles of 91.50° and 114.74°.

Fig. 4-14 illustrates the input current i_{in} and source voltage v_{in} observed by the rf source. By analyzing the fundamental components of these waveforms, we calculate the fundamental components of the input impedance Z_{in} seen by the rf source as described in Table 4.15.

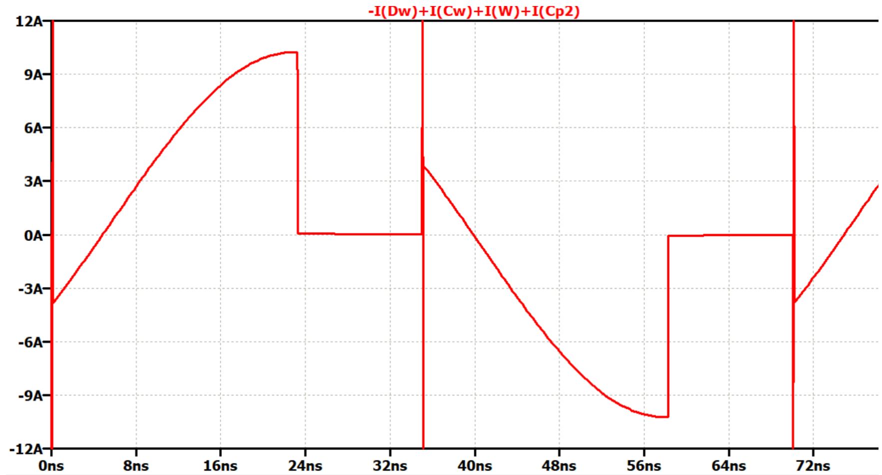

Figure 4-12: Waveform of the input current entering the switching network. This depicted current is the transformed input current represented as i_1 in our analysis and Figure 4-7.

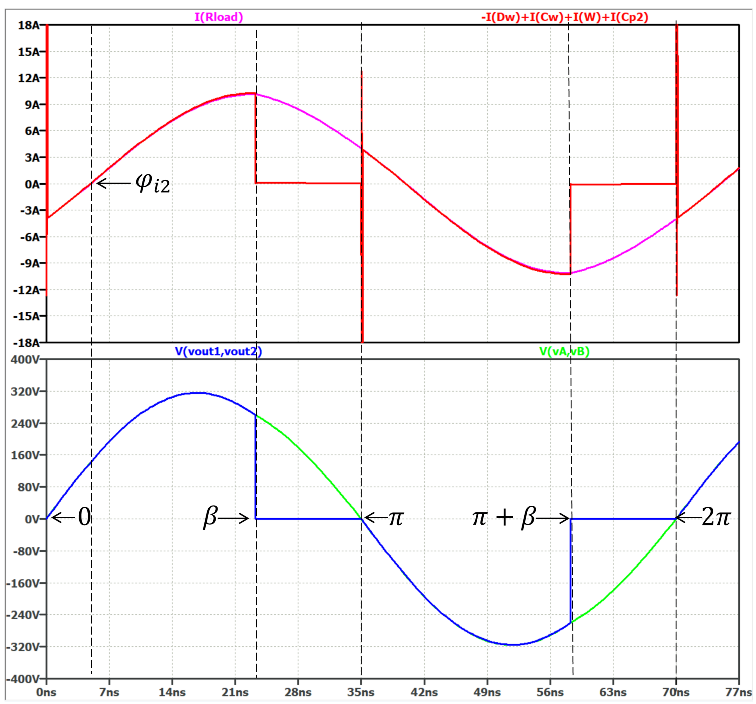

Figure 4-13: Voltage and current transformations in the CTMN.

These results enabled the calculation of the fundamental components of the magnitude and phase of the input impedance seen by the rf source, which is the input voltage v_{in} divided by the source current i_{in}, which resulted in 50.135 Ω, with resistive and reactive components $Z_{in} = 50.068\,\Omega$ and $X_{in} = -2.606\,\Omega$. The resistive input impedance Z_{in} is the target impedance for matching. Through these voltage and current transformations, the CTMN successfully achieves step-up impedance matching from an output impedance value

Fundamental Component	**Magnitude**	**Phase (degrees)**
Input Voltage, v_1	314.2 V	88.51°
Output Voltage, v_2	266.2 V	72.27°
Source Current, i_{in}	6.267 A	91.50°
Load Current, $i_{L\text{Load}}$	9.808 A	114.74°

Table 4.14: Fundamental components of voltage and current waveforms in the CTMN.

Input impedance Z_{in} Calculation	**Value**
Input impedance, $\lvert Z_{in}\rvert$	$50.135\,\Omega$
Phase shift $\angle Z_{in}$	$-2.98°$
Resistive component of input impedance, Z_{in}	$50.068\,\Omega$
Reactive component, X_{in}	-2.606Ω
Percentage error in impedance matching	0.27%

Table 4.15: Input impedance Z_{in} observed by the source for a loading of $Z_L = 20\,\Omega$.

of $Z_L = 20 + j0\,\Omega$ to an input impedance value of $Z_{in} = 50\,\Omega$ with an error of merely 0.27%, which is confirmed by these example simulation results.

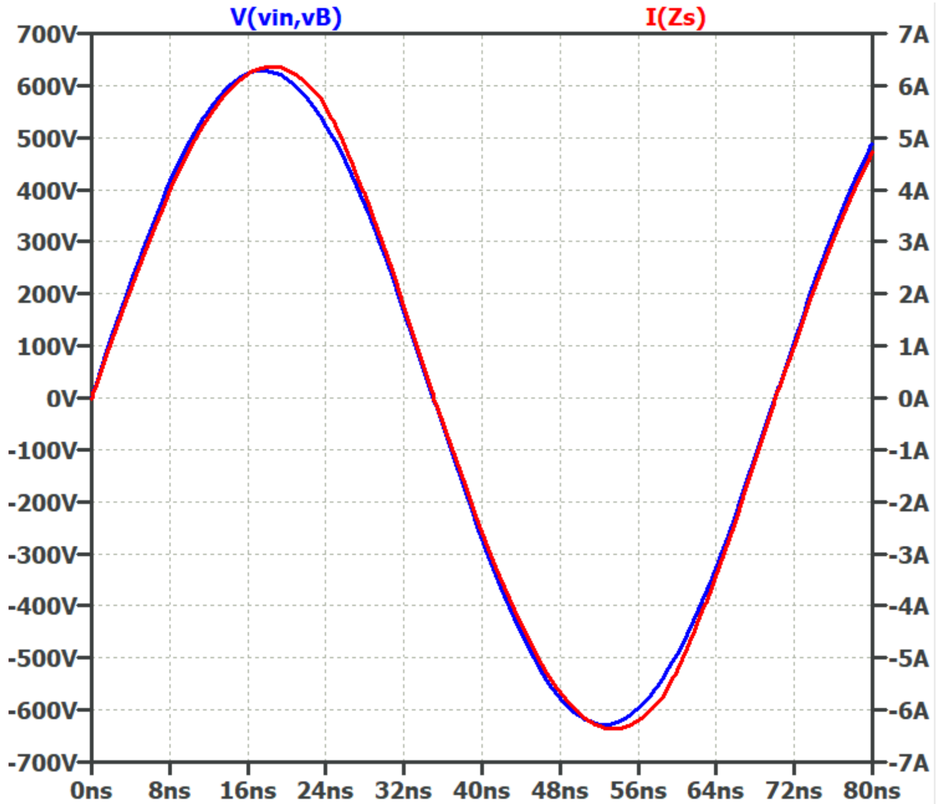

Figure 4-14: Input source current i_{in} and source voltage v_{in}, calculated as $I(Z_s)$ and $V(vin, vB)$ in the simulations, for the ideal LTSpice model.

4.6 Simulation Verification including Device Non-Idealities

In the previous section, the idealized version of the CTMN was analyzed, assuming perfect switching conditions and component behaviors. However, in real-world applications, various non-idealities come into play that can significantly impact the performance of the CTMN. These non-ideal behaviors can arise from several sources. For instance, the MOSFET switches may have inherent finite on-resistance, non-zero turn-on and turn-off times, and may exhibit inherent switch parasitics. Moreover, if both switches in a half bridge or a full bridge are on simultaneously, it creates a direct short circuit from the power supply to the ground, known as a shoot-through. A brief period, termed dead time, is required to prevent an accidental shoot-through, during which both switches in the half-bridges are turned off. Dead time ensures that one switch is fully off before the other switch starts to turn on, accounting for inherent switch delays and avoiding any overlap that could cause shoot-through. Fig. 4-15 illustrates the LTSpice model considering practical device non-ideas of

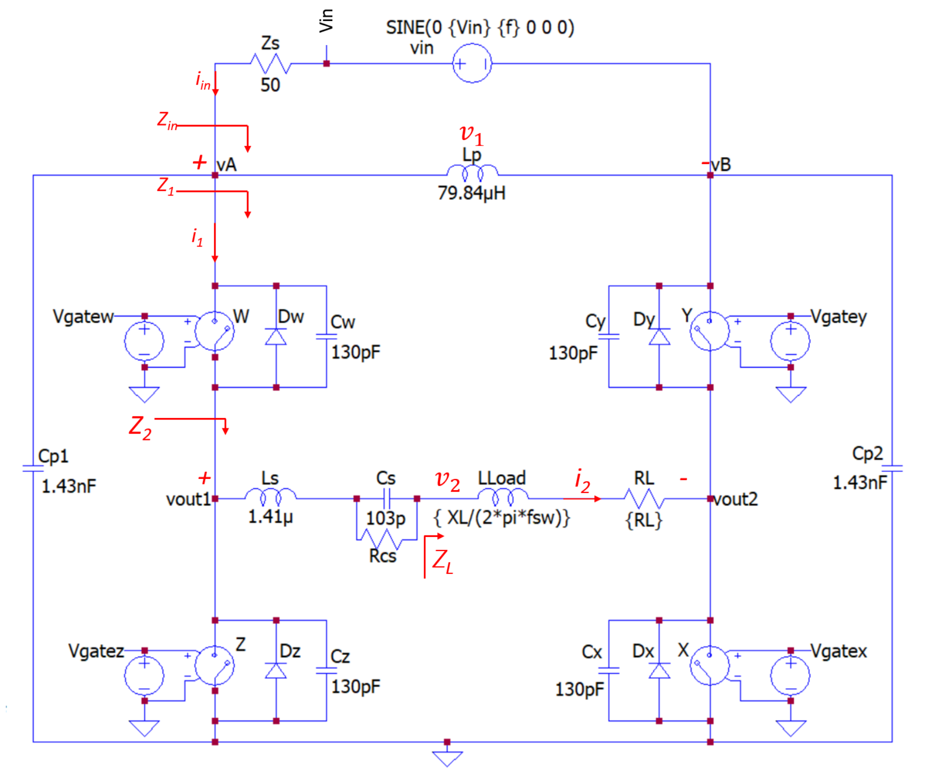

Figure 4-15: LTSpice model for CTMN designed considering practical non-idealities outlined in Table 4.16.

the CTMN.

4.6.1 Zero-Voltage Switching (ZVS)

Zero-voltage switching (ZVS) involves synchronizing the switching action with the point at which the voltage across the switch is at or near zero, minimizing the energy dissipated during the transition. ZVS is particularly relevant when considering non-ideal switch characteristics because it helps in avoiding the overlap of high voltage and current during switching events, which is where significant losses can occur. The non-ideal characteristics can lead to increased power dissipation, especially at higher frequencies, and can affect the voltage and current waveforms, resulting in deviations from the expected performance. This is why it is important to implement ZVS into the design to reduce the impact of these non-idealities.

Under Zero-Voltage Switching (ZVS), switches are turned on only when there is a small voltage across them, and the voltage across the switches remains low during turn-off. Implementing ZVS is crucial to avoid switching losses at high frequencies, especially for switches with finite rise and fall times and switch capacitances. The controllable transformation matching network is designed to ensure ZVS across wide loading conditions. In the CTMN, ZVS is achieved by charging and discharging switch capacitances (C_{oss}) through the load branch current i_2. The CTMN's control includes 'dead times' that allow for the complete charging and discharging of C_{oss}, thus enabling zero-voltage conditions during switch turn-on. These dead times are included in the switch control signals for practical conditions.

4.6.2 Control Signals for Effective ZVS Implementation

The control sequences considering rise time, fall time, and dead times are illustrated in Fig. 4-16. These signals incorporate the inherent dead times of switches. The switch control sequence for the CTMN is designed to enable zero-voltage switching, with dead times incorporated to allow for thorough charging and discharging of the switch capacitance C_{oss}.

Figure 4-17 illustrates the implementation of dead time, along with rise and fall times, in the control sequences. In this example, switch W turns off completely at a phase angle ofβ before switch Z turns on, preventing a short circuit in the left leg of the half-bridge.

Parameter	**Symbol**	**Values**
Switch capacitance	C_{oss}	130 pF
Rise time	t_{r}	8 ns
Fall time	t_{f}	7 ns
Dead time	t_{dead}	5.5 ns
Input tank capacitance	C_p	1.56nF
Replicated Parallel Capacitance	$C_{p1} = C_{p2} = C_p - C_{oss}$	1.43 nF

Table 4.16: LTSpice parameters considering switch dynamics and practical non-idealities in the CTMN.

4.6.3 Capacitor Charging and Discharging for ZVS

From the control sequence in Fig. 4-16, it is noted that each switch state is designed to achieve ZVS and the charging and discharging of specific capacitances $(C_w, C_y, C_y, \text{and}\, C_z)$

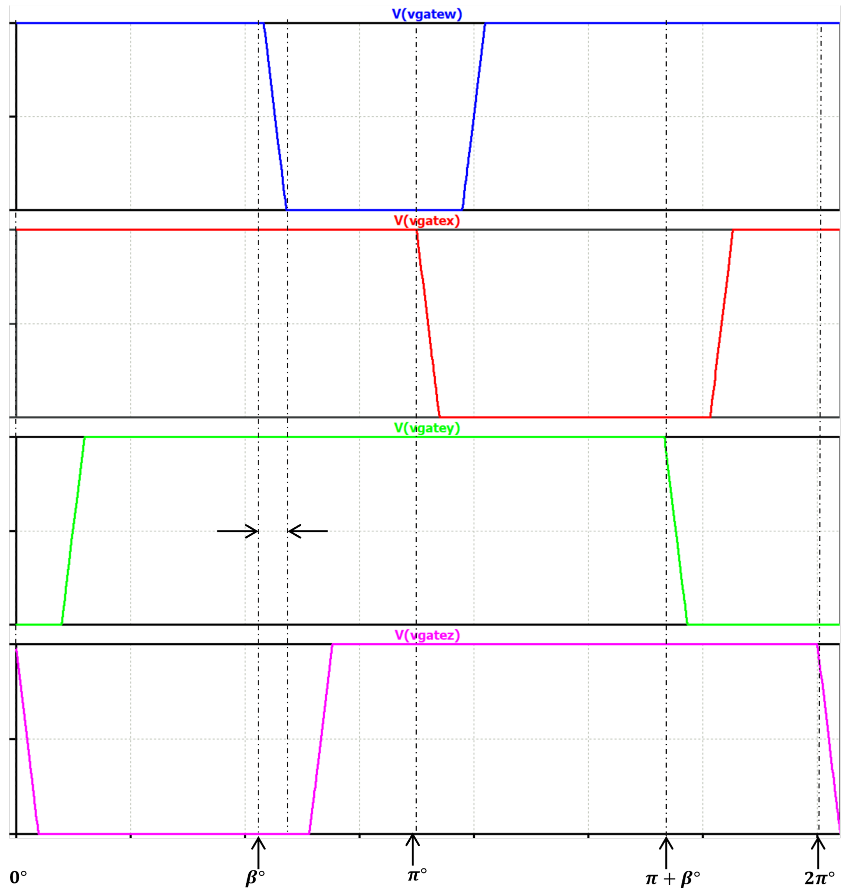

Figure 4-16: Practical control sequences considering rise and fall times. A 'high' level indicates that a corresponding switch is on, while a 'low' level indicates that it is off. The x-axis shows the phase angles that control the sequences.

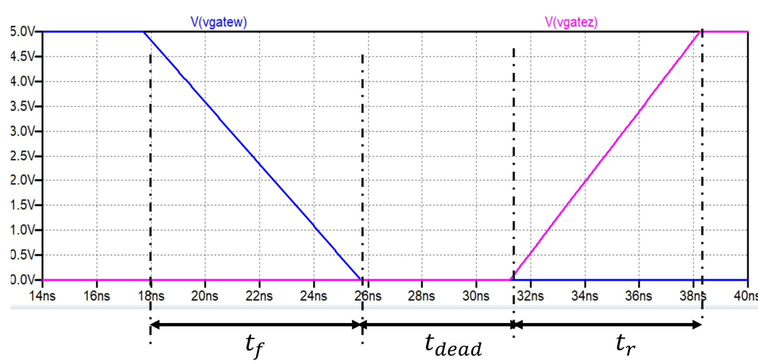

Figure 4-17: Control signals with finite rise time t_r, fall time t_f, and dead time t_{dead} for practical switches. In this example design, $t_r = 7$, $t_f = 8$ ns and $t_{dead} = 5.5$ ns.

are timed precisely in a controlled manner with the switching actions. The specific synchronization ensures that at any given time, certain switches are on and off, which controls the path of current flow and the charging and discharging of specific components. The operation of the CTMN, therefore, is not just a sequence of switch activations but a well-coordinated process that minimizes energy loss while maintaining effective control over the circuit's dynamic behavior.

The switch capacitance associated with the off switch in each state charges during the off time and prepares for a ZVS turn by accumulating charges. When the capacitor is fully charged, the voltage across it is at or near zero, which minimizes the energy lost during switching. The stored charge in the capacitance is discharged during the switch transition phase. By charging a switch capacitance during its off time, it prepares the switch for a ZVS turn-off in the next switch state. A summary of the charging and discharging processes of the switch capacitances over one full switching cycle in the CTMN is presented in Table 4.17.

Phase/Transition	**Switches ON**	**Switch OFF**	**Capacitor Charging**	**Capacitor Discharging**
Phase 1 (P1)	w, x, y	z	C_z	-
Transition to P2	-	w	C_w	C_z
Phase 2 (P2)	x, y, z	w	C_w	-
Transition to P3	-	x	C_x	C_w
Phase 3 (P3)	y, z, w	x	C_x	-
Transition to P4	-	y	C_y	C_x
Phase 4 (P4)	z, w, x	y	C_y	-
Transition to P1	-	z	C_z	C_y

Table 4.17: Summary of switch capacitor charging and discharging to achieve ZVS.

4.6.4 Results

The simulation results depicted in Figure 4-18 illustrate the CTMN's behavior, including practical aspects such as switch nonidealities and control deadtimes, as detailed in Table 4.16. The output voltage waveform, $V(V_{out1}, V_{out2})$, exhibits phase-controlled behavior in alignment with the design objectives of the CTMN. Notably, the input current waveform i_1

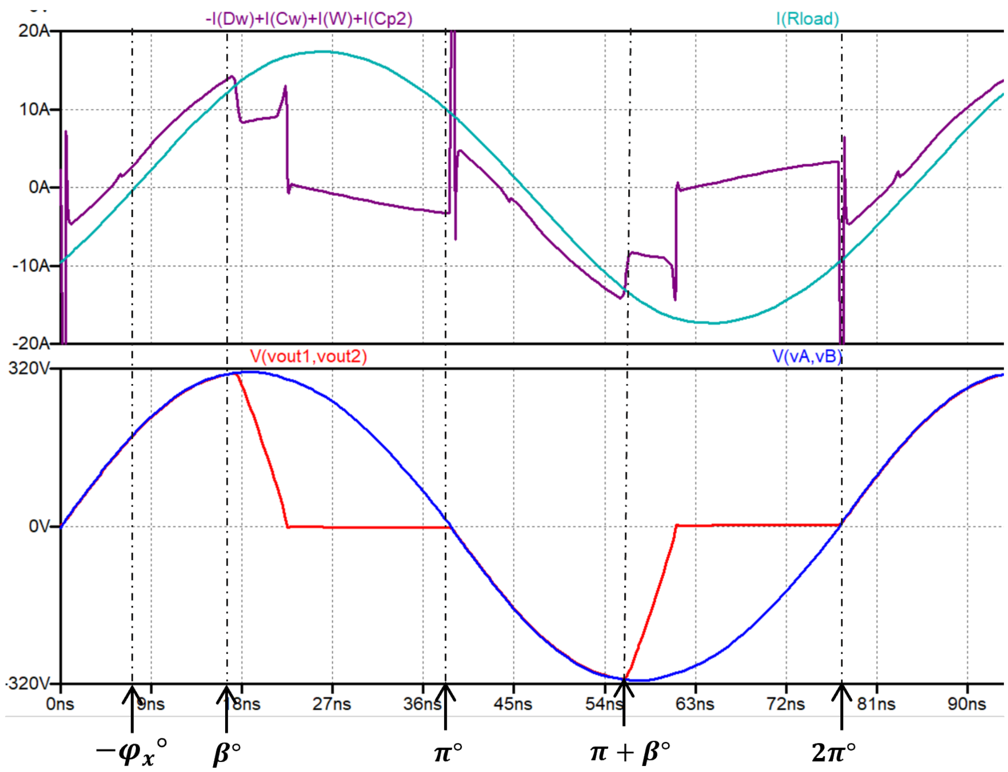

Figure 4-18: Voltage and current waveforms in the CTMN considering practical parameters detailed in Table 4.16.

into the controlled switching network calculated as $-I(Dw) + I(Cw) + I(W) + I(Cp2)$ in the simulations presents distinct spikes corresponding to the switching events in the CTMN, resulting from switch parasitics.

Fundamental Component	Magnitude	Phase (degrees)
Input voltage, v_{in}	314.5 V	95.67°
Output voltage, v_2	258 V	79.28°
Source current, i_{in}	6.34 A	83.67°
Load current, $i_{L,\text{Load}}$	9.54 A	121.65°

Table 4.18: Fundamental components of voltage and current waveforms in the CTMN.

Analysis of the fundamental components from Fig. 4-18 yields the input voltage $v_{in} = 314.5\,\text{V}$ with a phase angle of 95.67°, and the output voltage $v_2 = 258\,\text{V}$ with a phase angle of 79.28°. The input current i_{in} is 6.34 A at 83.67°, and the load current i_2 is 9.54 A at 121.65°. These values are summarized in Table 4.18. Fig. 4-19 illustrates the input source

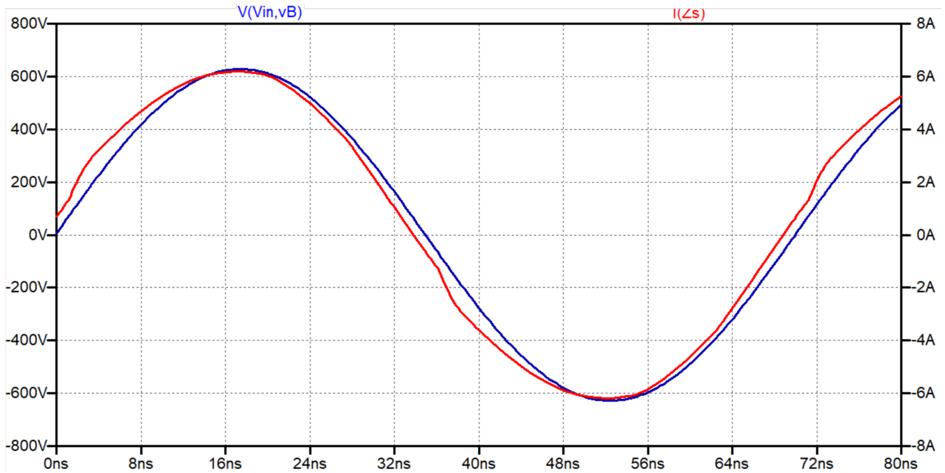

Figure 4-19: Input source current i_{in} and source voltage v_{in}, calculated as $I(Z_s)$ and $V(v(in), vB)$ in the simulations

current i_{in} and source voltage v_{in}, calculated as $I(Z_s)$ and $V(Vin, VB)$ in the simulations.

Impedance Calculation	**Value**
Magnitude of input impedance, $\|z_{in}\|$	50.14Ω
Phase shift $\angle z_{in}$	$5.92°$
Resistive component, $R_{in} = \|z_{in}\|cos(\angle z_{in})$	49.749Ω
Reactive component, $X_{in} = \|z_{in}\|sin(\angle z_{in})$	5.15Ω

Table 4.19: Input impedance zin observed by the source for a loading of $Z_L = 20\Omega$. We are interested in the resistive component of the input imepdance which we express as $R_{in} = Z_{in}$ in this thesis.

Impedance measurements of the CTMN reveal an input impedance z_{in} of $50.14\,\Omega$, with a phase shift of $5.92°$. The resistive input impedance Z_{in} is $49.749\,\Omega$, and the reactive component X_{in} is $5.15\,\Omega$. These values demonstrate that the resistive input impedance Z_{in} observed by the source for a loading of $Z_L = 20\,\Omega$ is close to 50Ω.

4.7 Summary and Discussion

We use the measurement method described in Subsection 4.5.3 to measure the input impedance for our LTSpice simulation models. Observing the results, we notice that adjustments in β were essential when the simulation results did not align with the desired magnitude of the target input resistive impedance $Z_{in} = 50\,\Omega$. Similarly, modifications in f_{sw} were necessary

Test Case	**Ideal** β **(°)**	**Modified** β **(°)**	**Ideal** f_{sw} **(MHz)**	**Modified** f_{sw}**(MHz)**
A	96.66	92.33	13.724	13.124
B	96.66	93.2	12.8721	12.87203
C	96.66	93.13	13.15	13.037
D	119.88	119.88	14.2223	14.2223
E	119.88	121.6	13.3401	13.3849

Table 4.20: Example cases of iterations in switching frequencies and phase control angles.

to address mismatches in the reactive component, as illustrated in Table 4.20. This experimental process, blending theory with hands-on adjustment, highlights the dynamic and adaptable nature of practical impedance matching. It emphasizes the need for an iterative approach, balancing theoretical foundations with practical observations and adjustments to achieve optimal tuning.

Test Case	Z_L (Ω)	z_{in} (Ω)	$\|Z_{in}\|$ (Ω)	$\angle Z_{in}$ (°)	R_{in} (Ω)	X_{in} (Ω)
A	$5 + j0$	49.32+ j5.071	49.58	5.87	49.320	5.071
B	$5 + j10$	49.81- j5.51	50.11	-6.29	49.81	-5.508
C	$5 + j15$	50-j2.82	50.079	-3.23	50	-2.82
D	$20 + j0$	50.068+ j0.06	50.063	0.07	50.064	0.061
E	$20 + j15$	50.01+j1.73	50.010	1.729	50.04	1.98

Table 4.21: Test cases with load impedance Z_L and transformed Z_{in} parameters.

Following a series of informed iterations, we successfully attain a match with the target impedance of50 within an acceptable range, as demonstrated by the load cases in Table 4.21.

As we conclude this chapter, we recognize that the iterative process of tuning β and f_{sw} not only fulfills the technical requirements of the CTMN but also reflects a broader theme of adaptation and refinement in the CTMN design. The next chapter will summarize the thesis findings and outline future work that can build upon this research.

Chapter 5

Conclusion

This thesis has proposed and analyzed a controllable transformation matching network (CTMN), leveraging a controllable switching network for impedance transformation and matching at radio frequencies. The CTMN incorporates a controlled switching network (CSN) whose function is akin to a variable transformer, utilizing phase control to dynamically adjust voltage and current transformations and hence adjust impedance transformation. The controlled switching network is operated in a manner that facilitates zero-voltage switching (ZVS) for active devices, aimed at enhancing response time and enabling high efficiency.

The theoretical framework and mathematical models presented in this thesis offer a comprehensive guide for designing a CTMN. This theoretical foundation is complemented by simulations performed in LTSpice, demonstrating the CTMN's capability to match a broad range of inductive load impedances to a standard 50 Ω input impedance. In particular, the example presented is for a frequency range centered around 13.56 MHz and for input power levels up to 1 kW, suggesting its suitability for radio frequency power applications. However, several limitations and areas for future work have been identified:

1. **Prototype Development:** The current study is based on simulations, and a physical prototype has not been constructed. Future efforts should aim to build and test a prototype to confirm the simulated results in practical settings.

2. **Non-Idealities and Practical Parameters:** The simulations did not account for

second-order non-idealities, which could impact the performance in real-world scenarios. Addressing these discrepancies is crucial for higher-power applications.

3. **Frequency Synchronization:** A significant challenge in practical implementation is synchronizing the switching frequency and phase with the source signal frequency. Future designs need to address this synchronization to ensure optimal performance.

4. **Alternative Phase Control Strategies:** While the current design focuses on symmetrical phase control around π, exploring different timing sequences could offer new ways to achieve ZVS transformations.

5. **Dynamic Control:** In the simulations, iterative changes in the two control parameters β and f_{sw} were used to achieve a match for a given load impedance. In a practical system, the load and input impedances would be measured and a dynamic matching algorithm would be used to achieve real-time matching. Practical methods to accomplish this must be developed, and matching speed and accuracy determined.

In summary, this thesis presents a CTMN design with promising simulation results for dynamic impedance matching. While these results are encouraging, realizing a physical prototype and addressing the noted limitations are essential steps toward practical application in RF systems.

Appendix A

Fourier Series Representation of Transformed Signals

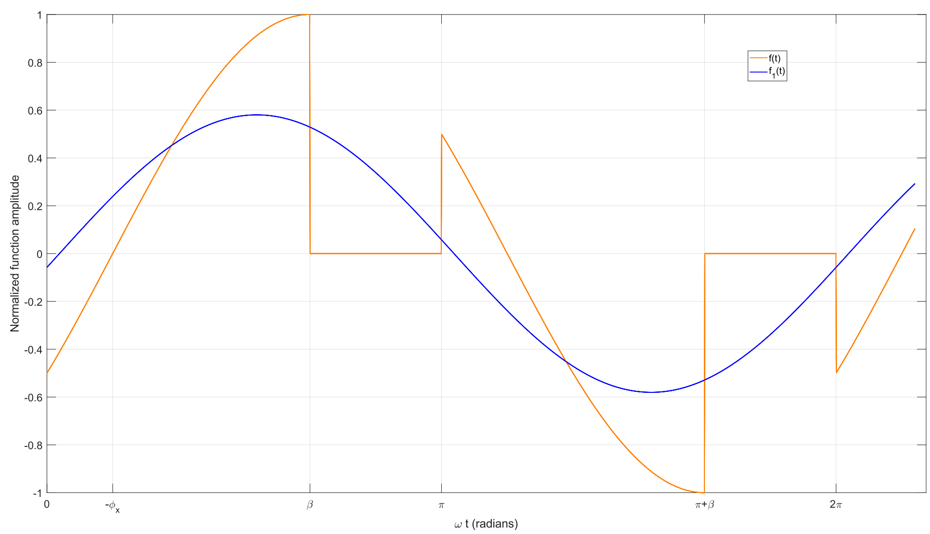

Figure A-1: A 'gated' sinusoidal signal $f(t)$ (orange waveform) and the fundamental component $f_1(t)$ (blue waveform) of the gated signal $f(t)$.The values used for this example plot are $\beta = \frac{2\pi}{3}$ radians and $\phi_x = \frac{\pi}{6}$ radians.

The function $f(t)$ is defined as:

$$f(t) = \sin(\omega t + \phi_x) \tag{A.1}$$

The Fourier series representation of the function is given by:

$$f(t) = a_0 + \sum_{n=1}^{\infty}(a_n \sin n\omega t + b_n \cos n\omega t) \tag{A.2}$$

where,

$$a_0 = \frac{1}{2\pi}\int_0^{2\pi} \sin(\omega t + \phi_x)d(\omega t) \tag{A.3}$$

$$a_n = \frac{2}{2\pi}\int_0^{2\pi} \sin(\omega t + \phi_x)\sin(n\omega t)d(\omega t) \tag{A.4}$$

$$b_n = \frac{2}{T}\int_0^{T} f(t)\sin(n\omega t)d(\Omega t) \tag{A.5}$$

The average value a_0 of the function over one period is calculated as zero, since the integral of a sine function over its period is zero.

To derive the fundamental component of $f(t)$, we need to calculate the fundamental frequency coefficients a_1 and b_1.

The Fourier coefficient a_1 for the fundamental frequency is calculated as:

$$a_1 = \frac{2}{2\pi}\int_0^{2\pi} \sin(\omega t + \phi_x)\sin(\omega t)d(\omega t) \tag{A.6}$$

The function value is 0 from β to π and from $\pi + \beta$ to 2π.

$$a_1 = \frac{1}{\pi}\int_0^{\beta} \sin(\omega t + \phi_x)\sin(\omega t)d(\omega t) + \int_{\pi}^{\pi+\beta} \frac{1}{\pi}\sin(\omega t + \phi_x)\sin(\omega t)d(\omega t) \tag{A.7}$$

Recognizing the half-wave symmetry in the function, the calculation of a_1 can be further simplified:

$$a_1 = 2\,\frac{1}{\pi}\int_0^{\beta} \sin(\omega t + \phi_x)\sin(\omega t)d(\omega t) \tag{A.8}$$

Applying the trigonometric identity $\sin A \sin B = \frac{1}{2}[\cos(A - B) - \cos(A + B)]$, we obtain:

$$\sin(\omega t + \phi_x)\sin(\omega t) = \frac{1}{2}[\cos(\phi_x) - \cos(2\omega t + \phi_x)] \tag{A.9}$$

It simplifies the expression for a_1 as:

$$a_1 = 2\,\frac{1}{\pi}\int_0^{\beta}\frac{1}{2}\left[\cos(\phi_x) - \cos(2\omega t + \phi_x)\right] d(\omega t) \tag{A.10}$$

$$= \frac{1}{\pi}\int_0^{\beta}\left[\cos(\phi_x) - \cos(2\omega t + \phi_x)\right] d(\omega t) \tag{A.11}$$

$$= \frac{1}{\pi}\left[\int_0^{\beta}\cos(\phi_x)\, d(\omega t) - \int_0^{\beta}\cos(2\omega t + \phi_x)\, d(\omega t)\right] \tag{A.12}$$

$$= \frac{1}{\pi}\left[\omega t\Big|_0^{\beta}\cos(\phi_x) - \frac{1}{2}\sin(2\omega t + \phi_x)\Big|_0^{\beta}\right] \tag{A.13}$$

$$= \frac{1}{\pi}\left[\beta\cos(\phi_x) - \frac{1}{2}\sin(2\beta + \phi_x) + \frac{1}{2}\sin(\phi_x)\right] \tag{A.14}$$

$$= \frac{\beta}{\pi}\cos(\phi_x) - \frac{1}{2\pi}[2\cos(\frac{2\beta + 2\phi_x}{2})\sin(\frac{-2\beta}{2})] \tag{A.15}$$

$$a_1 = \frac{\beta}{\pi}\cos(\phi_x) - \frac{1}{\pi}\sin\beta\cos(\beta + \phi_x) \tag{A.16}$$

Similarly, the Fourier coefficient b_1 for the fundamental frequency is determined by:

$$b_1 = \frac{2}{\pi}\int_0^{\beta}\sin(\omega t + \phi_x)\cos(\omega t)d(\omega t) \tag{A.17}$$

Applying the trigonometric identity $\sin A\cos B = \frac{1}{2}[\sin(A+B) + \sin(A-B)]$ simplifies the expression for b_1:

$$b_1 = \frac{1}{\pi}\int_0^{\beta}[\sin(2\omega t + \phi_x) + \sin(\phi_x)]d(\omega t) \tag{A.18}$$

After performing the integration and simplification, the result is:

$$b_1 = \frac{\beta}{\pi}\sin(\phi_x) + \frac{1}{\pi}\sin(\beta)\sin(\phi_x + \beta) \tag{A.19}$$

After deriving the coefficients, we can substitute them back into the fundamental component $f_1(t)$ of the Fourier series representation of $f(t)$. This representation allows us to express the function in terms of its amplitude and phase shift. Fundamental component of $f(t)$

$$f_1(t) = a_1\sin(\omega t) + b_1\cos(\omega t) \tag{A.20}$$

The function $f_1(t)$ can also be expressed in an alternate form with its magnitude and phase:

$$f_1(t) = M\sin(\omega t + \psi) \tag{A.21}$$

$$= M\angle\psi - 90^\circ = Me^{-j\frac{\pi}{2}}e^{j\psi} \tag{A.22}$$

Where the magnitude M and the phase shift ψ are given by:

$$M = \sqrt{a_1^2 + b_1^2} \tag{A.23}$$

$$\psi = \tan^{-1}\left(\frac{b_1}{a_1}\right) \tag{A.24}$$

The expressions for $a_1^2 + b_1^2$ are derived as follows:

$$a_1^2 + b_1^2 = \left[\frac{\beta}{\pi}\cos(\phi_x) - \frac{1}{\pi}\cos(\beta + \phi_x)\sin(\beta)\right]^2 + \left[\frac{\beta}{\pi}\sin(\phi_x) + \frac{1}{\pi}\sin(\phi_x + \beta)\sin(\beta)\right]^2 \tag{A.25}$$

$$= \frac{\beta^2}{\pi^2}\cos^2(\phi_x) + \frac{1}{\pi^2}\cos^2(\beta + \phi_x)\sin^2(\beta) - \frac{2\beta}{\pi^2}\cos(\phi_x)\cos(\beta + \phi_x)\sin(\beta) \tag{A.26}$$

$$= \frac{\beta^2}{\pi^2}\sin^2(\phi_x) + \frac{1}{\pi^2}\sin^2(\phi_x+\beta)\sin^2(\beta) + \frac{2\beta}{\pi^2}\sin(\phi_x)\sin(\phi_x+\beta)\sin(\beta) \tag{A.27}$$

$$= \frac{\beta^2}{\pi^2} + \frac{1}{\pi^2}\sin^2(\beta)[\sin^2(\phi_x+\beta)+\cos^2(\phi_x+\beta)] + \frac{2\beta}{\pi^2}\sin(\beta)[\sin(\phi_x+\beta) - \cos(\phi_x)\cos(\phi_x+\beta)] \tag{A.28}$$

$$= \frac{\beta^2}{\pi^2} + \frac{1}{\pi^2}\sin^2(\beta) + \frac{2\beta}{\pi^2}\sin(\beta)[-\cos(2\phi_x+\beta)] \tag{A.29}$$

Applying the trigonometric identity $\sin A \cos B = \frac{1}{2}[\sin(A+B)+\sin(A-B)]$:

$$= \frac{\beta^2}{\pi^2} + \frac{1}{\pi^2}\sin^2(\beta) - \frac{2\beta}{\pi^2}\sin(\beta)\cos(2\phi_x+\beta) \tag{A.30}$$

$$= \frac{\beta^2}{\pi^2} + \frac{1}{\pi^2}\sin^2(\beta) - \frac{2\beta}{\pi^2}\cdot\frac{1}{2}[\sin(2\phi_x+2\beta)+\sin(-2\phi_x)] \tag{A.31}$$

$$a_1^2 + b_1^2 = \frac{\beta^2}{\pi^2} + \frac{1}{\pi^2}\sin^2(\beta) - \frac{\beta}{\pi^2}[\sin(2\phi_x+2\beta)-\sin(2\phi_x)] \tag{A.32}$$

Replacing Equation (A.32) into Equation (A.23), we can derive $M = \sqrt{a_1^2+b_1^2}$ as the magnitude of the function $f_1(t)$:

$$M = \sqrt{\frac{\beta^2}{\pi^2} + \frac{1}{\pi^2}\sin^2(\beta) - \frac{\beta}{\pi^2}[\sin(2\phi_x+2\beta)-\sin(2\phi_x)]} \tag{A.33}$$

Similarly, ψ is the phase shift of the function $f_1(t)$:

$$\psi = \tan^{-1}\left(\frac{\frac{\beta}{\pi}\sin(\phi_x) + \frac{1}{\pi}\sin(\beta)\sin(\phi_x+\beta)}{\frac{\beta}{\pi}\cos(\phi_x) - \frac{1}{\pi}\sin(\beta)\cos(\phi_x+\beta)}\right) \tag{A.34}$$

$$\psi = \tan^{-1}\left(\frac{\beta\sin(\phi_x) + \sin(\beta)\sin(\phi_x+\beta)}{\beta\cos(\phi_x) - \sin(\beta)\cos(\phi_x+\beta)}\right) \tag{A.35}$$

Hence the Fourier representation of the fundamental component of the function f(t) illustrated in Fig. A-1 is $f_1(t)$ with magnitude M and phase shift ψ:

$$f_1(t) = M\sin(\omega t + \psi) = Me^{-j\frac{\pi}{2}}e^{j\psi} \tag{A.36}$$

$$M = \sqrt{\frac{\beta^2}{\pi^2} + \frac{1}{\pi^2}\sin^2(\beta) - \frac{\beta}{\pi^2}[\sin(2\phi_x + 2\beta) - \sin(2\phi_x)]} \tag{A.37}$$

$$\psi = \tan^{-1}\left(\frac{\beta\sin(\phi_x) + \sin(\beta)\sin(\phi_x + \beta)}{\beta\cos(\phi_x) - \sin(\beta)\cos(\phi_x + \beta)}\right) \tag{A.38}$$

Appendix B

Voltage and Current Transformation Derivations

$$
\begin{aligned}
M_{v1} &= M(\beta, \phi_x)\Big|_{\beta=\pi, \phi_x=0} \\
&= \sqrt{\frac{\pi^2}{\pi^2} + \frac{1}{\pi^2}\sin^2(\pi) - \frac{2\pi}{\pi^2}\sin(\pi)\cos(\pi + 2\cdot 0)} \\
= 1
\end{aligned}
\tag{B.1}
$$

$$
\begin{aligned}
\psi_{v1} &= \psi(\beta, \phi_x) \\
&= \tan^{-1}\left(\frac{\beta\sin(\phi_x) + \sin(\beta)\sin(\beta + \phi_x)}{\beta\cos(\phi_x) - \sin(\beta)\cos(\beta + \phi_x)}\right)
\end{aligned}
\tag{B.2}
$$

$$
\begin{aligned}
M_{v1} &= M(\beta, \phi_x)\Big|_{\beta=\pi, \phi_x=0} \\
&= \sqrt{\frac{0^2}{\pi^2} + \frac{1}{\pi^2}\sin^2(0) - \frac{2\cdot 0}{\pi^2}\sin(0)\cos(0 + 2\cdot 0)} \\
&= \sqrt{0 + 0 - 0} \\
&= 0
\end{aligned}
\tag{B.3}
$$

$$
\begin{aligned}
\psi_{v1} &= \psi(\beta, \phi_x)\Big|_{\beta=0,\phi_x=0} \\
&= \tan^{-1}\left(\frac{0\cdot\sin(0)+\sin(0)\sin(0+0)}{0\cdot\cos(0)-\sin(0)\cos(0+0)}\right) \\
&= \tan^{-1}\left(\frac{0}{0}\right) \\
&= \text{undefined}
\end{aligned} \tag{B.4}
$$

$$
\begin{aligned}
\Rightarrow X_T = -X_2 + \frac{\sqrt{R_2^2+X_2^2}}{N^2}&\frac{\pi}{\sqrt{\beta^2+\sin^2(\beta)-2\beta\sin(\beta)\cos(\beta)}} \quad \frac{1}{M(\tan^{-1}\frac{\beta+\sin(\beta)\sin(\beta)}{\beta-\sin(\beta)\cos(\beta)}-\tan^{-1}(\frac{X_2}{R_2}))} \\
&\times\sin(-\psi(\psi(\beta,0)-\tan^{-1}(\frac{X_2}{R_2})))
\end{aligned} \tag{B.5}
$$

Appendix C

MATLAB Script for Modeling CTMN Control Parameters

This MATLAB script calculates the two control parameters, the phase control angle (β) and switching frequency (f_{sw}), for a user input for a given load resistance R_L and reactance X_L.

```
    % Design of the CTMN
% Author Khandoker Nuzhat Rafa Islam
% MIT Thesis 2024

%% Plotting Fig: 2.11 and A.1 : A ‘gated (transformed signal in this thesis)’ \\
sinusoidal f(t) and its fundamental frequency component f_1(t)
%%Define the parameters
clc
clear
f = 13.56e6; % Frequency in Hz
omega = 2 * pi * f; % Angular frequency in rad/s
beta = 2*pi/3; % Example value for beta
phi_x = -pi/6 % Example value for phi_x

% Time vector from -T to T, where T is the period of the function
```

```
T = 1 / f; % Period of the sine function
t = linspace(0, T*1.1, 2000); % Time vector with 2000 points for a smooth plot
% The sinusoidal function
omega_t = omega * t; % Calculate omega*t

i_1 = sin(omega * t + phi_x);
i_1(omega_t > beta & omega_t < pi) = 0;
i_1(omega_t > pi+beta  & omega_t < 2*pi) =0 ;

plot(omega_t, i_1, 'LineWidth', 1.5, 'Color', [1, 0.5, 0]');
hold on; % Hold on to plot the second function on the same figure
xlabel('\omegat');
%ylabel('Magnitude');
%title('\beta = \pi/2, \phi_x=\pi/4');
grid on;
xticks([0, pi/6, beta, pi, pi+beta, 2*pi]);
xticklabels({'0', '-\phi_{x}', '\beta', '\pi', '\pi+\beta', '2\pi'});

%Drawing the fundamental

%M and beta functions
M = @(beta, phi_x) sqrt((beta.^2 / pi^2) + (1 / pi^2) * \\
sin(beta).^2 - (2 * beta / pi^2) * sin(beta) .* cos(beta + 2 * phi_x));
psi = @(beta, phi_x) atan2(beta * sin(phi_x) + sin(beta) .* \\
sin(beta + phi_x), beta * cos(phi_x) - sin(beta) .* cos(beta + phi_x));

% Calculate M and psi for the given beta and phi_x
M_value = M(beta, phi_x)
psi_value = psi(beta, phi_x)
```

```
% The sinusoidal function using M and psi
f_t = M_value * sin(omega_t + psi_value);

% Plotting
plot(omega_t, f_t, 'LineWidth', 1.5, 'Color', 'blue');
grid on;
xlabel('\omega t (radians)');
ylabel('Normalized function amplitude');
%title('Plot of f(t) using M and psi');
legend( 'f(t)', 'f_1(t)');

%%  Plotting control plots RL/Z0 and Xnet/RL

b = pi*(0.4:0.001:1);

numA = sqrt(b.^2 + sin(b).^2 - 2*b.*sin(b).*cos(b));
denA = sqrt(1+ ((2*b.*sin(b).^2)./(b.^2 - sin(b).^2.*cos(b).^2-sin(b).^4)).^2);
phix = atan2((-sin(b).^2),(b+sin(b).*cos(b)));

RL_Zo = numA./denA/pi.*M(b,phix);
Xnet_RL = (2*b.*sin(b).^2)./(b.^2-sin(b).^2.*cos(b).^2-sin(b).^4);

% Plotting beta vs RL/Z0 plot
figure(1)
clf
plot(180*b/pi,RL_Zo,'LineWidth',2)
ylabelObj = ylabel('$\frac {R_L}{Z_0}$', 'Interpreter', 'latex');
set(ylabelObj, 'FontSize',24 , 'FontWeight', 'bold');
xlabel('$\beta (\circ)$',  'Interpreter', 'latex', 'FontSize', 14, 'FontWeight', 'bold')
set(gca, 'FontSize', 12, 'LineWidth', 1.5) % Set font size and line width for axes
```

```
grid on;
hold on
% Plotting beta vs Xnet/RL plot
figure(2)
clf
plot(180*b/pi,Xnet_RL,'LineWidth',2)
ylabel('$\frac {X_{net}}{R_L}$',  'Interpreter', 'latex', 'FontSize', 24, 'FontWeight',
xlabel('$\beta (^\circ)$',  'Interpreter', 'latex', 'FontSize', 14, 'FontWeight', 'bold'
set(gca, 'FontSize', 12, 'LineWidth', 1.5) % Set font size and line width for axes
grid on;
hold on;

%% User Script for determining phase control angle beta nd switching frequency f_{sw}

% Ask user to insert value for RL and jXL
RL = input('Please enter the value for RL: ');
XL = input('Please enter the value for jXL: ');

% Define constants for Ls and Cs
Ls = 1.41e-06;
Cs = 103.e-12;
% Set a range for beta in radians for calculations
b = pi*(0.4:0.001:1);

% Calculate RL/Z0 vs beta
numA = sqrt(b.^2 + sin(b).^2 - 2.*b.*sin(b).*cos(b));
denA = sqrt(1+ ((2.*b.*sin(b).^2)./(b.^2 - sin(b).^2.*cos(b).^2-sin(b).^4)).^2);
phix = atan2((-sin(b).^2),(b+sin(b).*cos(b)));
RL_Zo = numA./denA/pi.*M(b,phix); % M function needs to be defined
```

```
% Find the beta value where desired RL/Z0 occurs
[~, idx] = min(abs(RL_Zo - RL/50)); % Assuming Z0 = 50 Ohms
beta_desired = b(idx);
% Output that beta value on the user interface

% Find the Xnet/RL ratio that we get at beta = x
Xnet_RL_ratio = (2.*b.*sin(b).^2)./(b.^2-sin(b).^2.*cos(b).^2-sin(b).^4);
Xnet_RL_at_beta = Xnet_RL_ratio(idx);

% Output the Xnet/RL ratio for the user
%fprintf('The corresponding Xnet/RL ratio at beta = %.2f degrees is: %.2f\n', \\
rad2deg(beta_desired), Xnet_RL_at_beta);

% Find value of Xnet = Xnet/RL * RL for that specific beta
Xnet = Xnet_RL_at_beta * RL;
%Output the Xnet value for the user
fprintf('The corresponding Xnet value is: %.6f Ohms\n', Xnet);

% Calculate compensation reactance
Xcomp = Xnet - XL;

% Calculate switching frequency f_sw
f_sw = (Cs .* Xcomp + sqrt((Cs.^2 .* Xcomp.^2) + \\
(4 * Ls * Cs))) / (2 * Ls * Cs) / 2 / pi;

% Output the switching frequency to the user
fprintf('For given RL and XL,')
fprintf('the phase control angle, beta value is: %.2f degrees\n', rad2deg(beta_desired))
fprintf('The switching frequency f_sw is: %.4f MHz\n', f_sw/1e6);
```

```
%%%%% Design of the CTMN

%% Parallel tank design

Vin=314.16;
P=1000;
Z0=50;

f_par=14.238e6; % the higher end of the BW
Qp=7; %finalized value, the lowest Q
Z0=50;

Cp=Qp/2/pi/f_par/Z0 ;
Lp=Z0/2/pi/f_par/Qp  ;


%% Series tank component selection with 5% variations from fc=13.56MHz
f_c=13.56e6;
f_min=f_c+0.05*f_c;
f_max=f_c-0.05*f_c;

Xnet_max=17.352;
Xnet_min=8.95;

XL_max=15; XL_min=0;

Xcomp_min= Xnet_min- XL_max ; %for max load reactance XL=15
Xcomp_max= Xnet_max-0; % for min load reactance XL=0
```

```
%Solving them we get Ls and Cs for a tank resonant frequency of
%f_series=13.207MHz
Ls=1.41e-6;
Cs=103e-12;

f_series= 1/sqrt(Ls*Cs)/2/pi;



%% Frequency Selection (Fig. 4.6 )
%%This plot determines the operating frequency for a given load R+jXL

figure (3)

Xnet=8.9948;
Xcomp= linspace(-6.05, 17.36,100);
XL=Xnet-Xcomp;
Ls= 1.41e-06;
Cs= 103.e-12;
f_sw= (Cs.*Xcomp+sqrt((Cs.^2.*Xcomp.^2)+(4*Ls*Cs)))/(2*Ls*Cs)./2./pi;
plot(XL, f_sw/10e5, 'LineWidth',2, 'Color','r');
hold on;

xlabelObj = xlabel('Load Reactance, $X_L (\Omega)$', 'Interpreter', 'latex');
set(xlabelObj, 'FontSize', 14, 'FontWeight', 'bold');

% Applying LaTeX interpreter to ylabel
ylabelObj = ylabel('Switching Frequency, $f_{sw}$ (MHz)', 'Interpreter', 'latex');
set(ylabelObj, 'FontSize', 24, 'FontWeight', 'bold');

% Setting font size and line width for axes
```

```
set(gca, 'FontSize', 12, 'LineWidth', 1);

Xnet=13.234662;
Xcomp= linspace(-6.05, 17.36,100);
XL=Xnet-Xcomp;
Ls= 1.41e-06;
Cs= 103.e-12;
f_sw= (Cs.*Xcomp+sqrt((Cs.^2.*Xcomp.^2)+(4*Ls*Cs)))/(2*Ls*Cs)./2./pi;
plot(XL, f_sw/10e5, 'LineWidth',2, 'Color','b');
hold on;

Xnet=15.8814;
Xcomp= linspace(-6.05, 17.36,100);
XL=Xnet-Xcomp;
Ls= 1.41e-06;
Cs= 103.e-12;
f_sw= (Cs.*Xcomp+sqrt((Cs.^2.*Xcomp.^2)+(4*Ls*Cs)))/(2*Ls*Cs)./2./pi;
plot(XL, f_sw/10e5, 'LineWidth',2, 'Color','g');
hold on;

Xnet=17.353058;
Xcomp= linspace(-6.05, 17.36,100);
XL=Xnet-Xcomp;
Ls= 1.41e-06;
Cs= 103.e-12;
f_sw= (Cs.*Xcomp+sqrt((Cs.^2.*Xcomp.^2)+(4*Ls*Cs)))/(2*Ls*Cs)./2./pi;
plot(XL, f_sw/10e5, 'LineWidth',2, 'Color','m');

yline(12.88,'Linewidth',2,'Color','c' );
yline(14.238,'Linewidth',2,'Color','k' );
```

```
grid on;
legend('$R_L = 5 \, \Omega$','$R_L = 10 \, \Omega$', \\
'$R_L = 15 \, \Omega$', '$R_L = 20 \, \Omega $', \\
'12.88 MHz', '14.24 MHz',  'Interpreter', 'latex')


%% Smiths Chart Plotting
%%This script shows how to use SmithChart to plot a shaded region
close all
clear all
clc

%%Define impedance region
%Rmin changes the left curve of the yellow shaded region
%Rmax changes the right curve of the yellow shaded region
%Xmin bottom kine of the region
%Xmax top curve of the region
%Npts is the acuuracy of the border of the region
Rmin = 5; Rmax = 20;
Xmin = 0; Xmax = 15;
Npts = 100;

r_bound = [linspace(Rmin,Rmax,Npts),linspace(Rmax,Rmax,Npts),...
          linspace(Rmax,Rmin,Npts),linspace(Rmin,Rmin,Npts)];
x_bound = [linspace(Xmax,Xmax,Npts),linspace(Xmax,Xmin,Npts),...
          linspace(Xmin,Xmin,Npts),linspace(Xmin,Xmax,Npts)];
z_bound = r_bound+1i*x_bound;


%%Plot impedance region on Smith Chart
```

```
gma_bound = (z_bound-50)./(z_bound+50);
plot(0, 0, 'ro', 'MarkerSize', 10, 'MarkerFaceColor', 'r'); % Red dot at center
hold on;
SmithChart(); hold on;


plot(real(gma_bound),imag(gma_bound),'-k',LineWidth=2);
fill(real(gma_bound),imag(gma_bound),'y');
hold off;
chH = get(gca,'Children');
set(gca,'Children',flipud(chH))



%% Transformation Functions
function Mval = M(bt,px)
    % Magnitude function M(beta,phix).
    % bt is beta, px is phix
    Mval = sqrt(bt.^2+sin(bt).^2-2*bt.*sin(bt).*cos(bt+2*px))/pi;
end

function Psival = Psix(bt,px)
    % Phase shift function psi(beta,phix).
    % bt is beta, px is phix
    Psival = atan2((bt.*sin(px)+sin(bt).*sin(bt+px)),(bt.*cos(px)-sin(bt).*cos(bt+px)));
end
```

Appendix D

LTSpice Netlist

D.1 Ideal Model

Schematic

Node Connections

```
Lp vA vB { Z0/(2*pi*fp*Qp)} Rser=1m
RLoad vR vout2 {RL}
S§X 0 vout2 vgatex 0 Qreal
S§Z 0 vout1 vgatez 0 Qreal
vs vin vB SINE(0 {Vin} {f} 0 0 0)
Dz 0 vout1 D
Dx 0 vout2 D
Cz vout1 0 {Coss}
Cx vout2 0 {Coss}
Ls vout1 N001 1.41µ Rser=1m
Dw vout1 vA D
Cw vA vout1 {Coss}
Dy vout2 vB D
Cy vB vout2 {Coss}
```

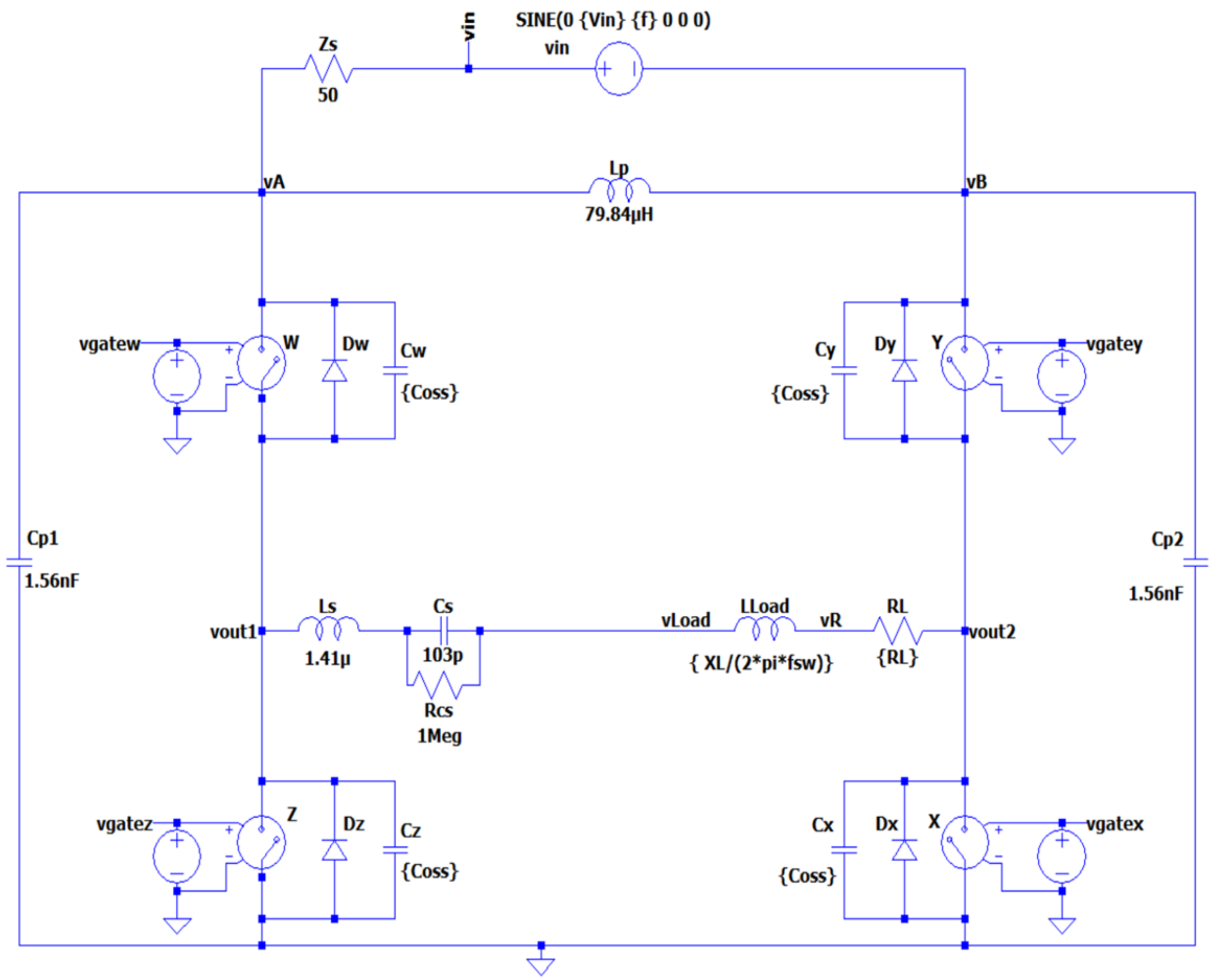

SINE(0 {Vin} {f} 0 0 0)
vin
vin
Zs
50
Lp
79.84μH
vA
vB
vgatew
W
Dw
Cw
{Coss}
Cy
Dy
Y
vgatey
{Coss}
Cp1
1.56nF
Cp2
1.56nF
Ls
1.41μ
Cs
103p
Rcs
1Meg
vout1
vLoad
LLoad
{ XL/(2*pi*fsw)}
vR
RL
{RL}
vout2
vgatez
Z
Dz
Cz
{Coss}
Cx
Dx
X
vgatex
{Coss}

Control Signals

```
Vgatew vgatew 0 PULSE(5 0 {(beta/360*T-0.5*tdead)} {tf} {tr} {((180-beta)/360)*T+tdead}
Vgatey vgatey 0 PULSE(5 0 {(180+beta)/360*T-0.5*tdead} {tf} {tr} \\
{((180-beta)/360)*T+tdead} {T})
Vgatex vgatex 0 PULSE(5 0 {((180)/360*T)} {tf} {tr} {((beta)/360)*T} {T})
Vgatez vgatez 0 PULSE(5 0 0 {tf} {tr} {((beta)/360)*T} {T})
S§W vout1 vA vgatew 0 Qreal
S§Y vout2 vB vgatey 0 Qreal
LLoad vLoad vR { XL/(2*pi*fsw)}
Cp1 vA 0 {Qp/(2*pi*fp*Z0)}
Cp2 vB 0 {Qp/(2*pi*fp*Z0)}
Cs N001 vLoad 103p
R§Zs vin vA 50
Rcs vLoad N001 1Meg
```

Fourier Analysis

```
Fourier Analysis:
.four {f} 1 1 V(vA,vB) FROM STTRIG TO ENDTRIG
.four {f} 1 1 I(Zs) FROM STTRIG TO ENDTRIG
.four {f} 1 1 V(vin,vB) FROM STTRIG TO ENDTRIG
.four {f} 1 1 I(RLoad) FROM STTRIG TO ENDTRIG
.four {f} 1 1 I(Ls) FROM STTRIG TO ENDTRIG
.four {f} 1 1 V(VR,vout2) FROM STTRIG TO ENDTRIG
.four {f} 1 1 V(VLoad,VR) FROM STTRIG TO ENDTRIG
.four {f} 1 1 V(VLoad,Vout2) FROM STTRIG TO ENDTRIG
.four {f} 1 1 V(vout1,VLoad) FROM STTRIG TO ENDTRIG
.four {f} 1 1 V(vout1,VR) FROM STTRIG TO ENDTRIG
.four {f} 1 1 V(vout1,vout2) FROM STTRIG TO ENDTRIG
```

Parameters

```
* .params Z0=50 RL= RL_Z0*Z0 Xnet= Xnet_RL*RL
\n.param Qp=1 T=1/f Vin=632.455 tdead=4n tf=0.1n tr=tf Coss=0.10p f2=14.238Meg\n
\n \n.model Qreal SW(Ron=5m Roff=1Meg Vt=1 Vh=0)
\n.model D D( Ron=5m Roff=1Meg Vfwd=1)\n.tran 0 100u 80u .001u
.meas TRAN P_IN AVG V(vA,vB)*I(Rin) FROM 20/f to 21/f
.meas TRAN P_OUT AVG V(vR,vout2)*I(RLoad) FROM 20/f TO 21/f
.params T= 1/f tdead=0.2n tf=0.01n tr= tf
.params RL=20  XL=0.0001
.params beta=119.95   fsw= 14.2263Meg f= 14.275Meg
.params Z0=50 Qp=7 Vin=628.32 Coss= 0.1p fp=14.3Meg
.model Qreal SW(Ron=5m Roff=1Meg Vt=1 Vh=0)
.model D D( Ron=5m Roff=1Meg Vfwd=1u)
.tran 0 100u 80u .001u
* Vgatew
* Vgatez
* Vgatey
* Vgatex
.backanno
.end
```

D.2 Simulation with Device Non-idealities

Schematic

Node connections:

```
Lp vA vB { Z0/(2*pi*f2*Qp)} Rser=1m
RLoad vR vout2 {RL}
S§X 0 vout2 Vgatex 0 Qreal
```

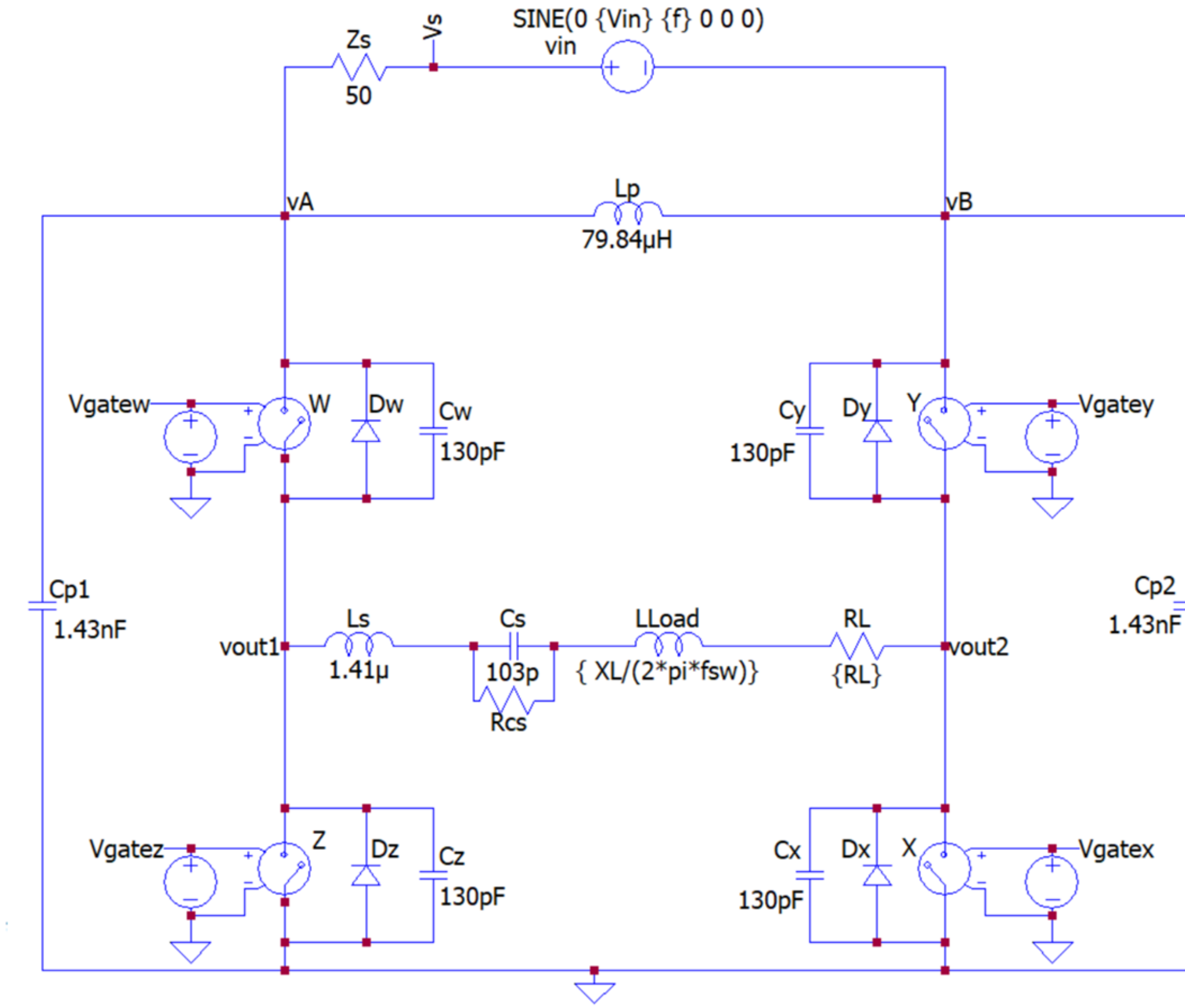
SINE(0 {Vin} {f} 0 0 0)
vin
Zs
50
Vs
Lp
79.84µH
vA
vB
Vgatew
W
Dw
Cw
130pF
Cy
130pF
Dy
Y
Vgatey
Cp1
1.43nF
Cp2
1.43nF
vout1
Ls
1.41µ
Cs
103p
Rcs
LLoad
{ XL/(2*pi*fsw)}
RL
{RL}
vout2
Vgatez
Z
Dz
Cz
130pF
Cx
130pF
Dx
X
Vgatex

```
S§Z 0 vout1 Vgatez 0 Qreal
vs Vin vB SINE(0 {Vin} {f} 0 0 0)
Dz 0 vout1 D
Dx 0 vout2 D
Cz vout1 0 {Coss}
Cx vout2 0 {Coss}
Ls vout1 N001 1.41µ Rser=1m
Dw vout1 vA D
Cw vA vout1 {Coss}
Dy vout2 vB D
Cy vB vout2 {Coss}
```

Control Signals

```
Vgatew Vgatew 0 PULSE(5 0 {(beta/360*T-0.5*tdead)}\\
{tf} {tr} {((180-beta)/360)*T+tdead} {T})
Vgatey Vgatey 0 PULSE(5 0 {(180+beta)/360*T-0.5*tdead} \\
{tf} {tr} {((180-beta)/360)*T+tdead} {T})
Vgatex Vgatex 0 PULSE(5 0 {((180)/360*T)} {tf} {tr} {((beta)/360)*T} {T})
Vgatez Vgatez 0 PULSE(5 0 0 {tf} {tr} {((beta)/360)*T} {T})
S§W vout1 vA Vgatew 0 Qreal
S§Y vout2 vB Vgatey 0 Qreal
LLoad VLoad vR { XL/(2*pi*f)}
Cp1 vA 0 {Cp-Coss}
Cp2 vB 0 {Cp-Coss}
Cs N001 VLoad 103p
R§1 Vin vA 50
Rcs VLoad N001 1Meg
```

Fourier Analysis

```
Fourier Analysis:
.four {f} 1 1 V(vA,vB) FROM STTRIG TO ENDTRIG
.four {f} 1 1 I(1) FROM STTRIG TO ENDTRIG
.four {f} 1 1 V(vin,vB) FROM STTRIG TO ENDTRIG
.four {f} 1 1 I(RLoad) FROM STTRIG TO ENDTRIG
.four {f} 1 1 I(Ls) FROM STTRIG TO ENDTRIG
.four {f} 1 1 V(VR,vout2) FROM STTRIG TO ENDTRIG
.four {f} 1 1 V(VLoad,VR) FROM STTRIG TO ENDTRIG
.four {f} 1 1 V(VLoad,Vout2) FROM STTRIG TO ENDTRIG
.four {f} 1 1 V(vout1,VLoad) FROM STTRIG TO ENDTRIG
.four {f} 1 1 V(vout1,VR) FROM STTRIG TO ENDTRIG
.four {f} 1 1 V(vout1,vout2) FROM STTRIG TO ENDTRIG
.meas TRAN P_IN AVG V(vA,vB)*I(Rin) FROM 50/f TO 51/f
.meas TRAN P_OUT AVG V(vR,vout2)*I(RLoad) FROM 50/f TO 51/f
```

Parameters

```
.params T= 1/f tdead=11n tf=8n tr=7ns
.params beta=119.88  f=14.275Meg
.params Z0=50 Qp=5 Vin=628.32 Coss= 130p f2=14.3Meg
.model Qreal SW(Ron=22m Roff=1Meg Vt=2.5 Vh=-2.5)
.model D D(  Roff=1Meg Vfwd=1.7)
.tran 0 80.2u 80u .001u
* Vgatew
* Vgatez
* Vgatey
* Vgatex
.params RL=20 XL=0.0001n
.param Cp = {Qp/(2*pi*f2*Z0)}
```

```
.backanno

.end
```

Bibliography

[1] T. Murayama, T. Bando, K. Furiya, and T. Nakamura. Method of designing an impedance matching network for wireless power transfer systems. In *JECON 2016 42nd Annual Conference of the IEEE Industrial Electronics Society*, pages 4504–4509, 2016.

[2] B. Regensburger, A. Kumar, S. Sinha, and K. Afridi. High-performance 13.56-mhz large air-gap capacitive wireless power transfer system for electric vehicle charging. In *2018 IEEE 19th Workshop on Control and Modeling for Power Electronics (COMPEL)*, pages 1–4, 2018.

[3] Y. Lim and et al. An adaptive impedance-matching network based on a novel capacitor matrix for wireless power transfer. *IEEE Transactions on Power Electronics*, 29(8): 4403–4413, Aug 2014.

[4] M. K. Kazimierczuk. Rf power amplifiers. John Wiley & Sons, Ltd, 2014.

[5] S. Sohn, J. T. Vaughan, and A. Gopinath. Auto-tuning of the rf transmission line coil for high-fields magnetic resonance imaging (mri) systems. In *2011 IEEE MTT-S International Microwave Symposium*, pages 1–4, June 2011.

[6] A. Abuelhaija, K. Solbach, and A. Buck. Power amplifier for magnetic resonance imaging using unconventional cartesian feedback loop. In *2015 German Microwave Conference*, pages 119–122, March 2015.

[7] F. Raab, P. Asbeck, S. Cripps, P. Kenington, Z. Popovic, N. Pothecary, J. Sevic, and N. Sokal. Power amplifiers and transmitters for rf and microwave. *IEEE Transactions on Microwave Theory and Techniques*, 50(3):814–826, 2002.

[8] Z. Kaczmarczyk. High-efficiency class e, ef2, and e/f3 inverters. *IEEE Trans. Ind. Electron.*, 53(5):1584–1593, Oct 2006.

[9] S. Kee, I. Aoki, A. Hajimiri, and D. Rutledge. The class e/f family of zvs switching amplifiers. *IEEE Trans. Microw. Theory Tech.*, 51(6):1677–1690, Jun 2003.

[10] J. Rivas, Y. Han, O. Leitermann, A. Sagneri, and D. Perreault. A high frequency resonant inverter topology with low voltage stress. *IEEE Trans. Power Electron.*, 23 (4):1759–1771, Jul 2008.

[11] M. K. Kazimierczuk. Rf power amplifiers. John Wiley & Sons, 2008.

[12] N. Sokal. Class-e rf power amplifiers. *QEX*, pages 9–20, Jan./Feb. 2001.

[13] V. Tyler. A new high-efficiency high-power amplifier. *Marconi Review*, 21(130):96–109, 3rd quarter 1958.

[14] K. Honjo. A simple circuit synthesis method for microwave class-f ultrahigh efficiency amplifiers with reactance-compensation circuits. *SolidState Electron.*, 44(8):1477–1482, Aug 2000.

[15] Y. Han, O. Leitermann, D. A. Jackson, J. M. Rivas, and D. J. Perreault. Resistance compression networks for radio-frequency power conversion. *IEEE Transactions on Power Electronics*, 22(1):41–53, Jan 2007.

[16] L. Roslaniec, A. S. Jurkov, A. Al Bastami, and D. J. Perreault. Design of single-switch inverters for variable resistance/load modulation operation. *IEEE Transactions on Power Electronics*, 30(6):3200–3214, June 2015.

[17] D. J. Perreault, J. M. Rivas, and C. R. Sullivan. Gan in switched-mode power amplifiers. In Gaudenzio Meneghesso, Matteo Meneghini, and Enrico Zanoni, editors, *Gallium Nitride Enabled High Frequency and High Efficiency Power Conversion*, pages 181–223. Springer-Verlag, 2018. ISBN 978-3-319-77993-5.

[18] W. D. Braun and D. J. Perreault. A high-frequency inverter for variable-load operation. *IEEE Journal of Emerging and Selected Topics in Power Electronics*, 7(2):706–721, June 2019.

[19] Xin Zan, Khandoker N Rafa Islam, and David J Perreault. Wide-range switched-mode power amplifier architecture. In *2023 IEEE 24th Workshop on Control and Modeling for Power Electronics (COMPEL)*, pages 1–9, 2023. doi: 10.1109/COMPEL52896.2023.10221014.

[20] Yuetao Hou and Khurram K. Afridi. Design of variable-load class-e inverter using laplace based steady-state modeling. In *2022 IEEE Energy Conversion Congress and Exposition (ECCE)*, pages 1–5, 2022. doi: 10.1109/ECCE50734.2022.9947899.

[21] D. J. Perreault. A new architecture for high-frequency variable-load inverters. In *2016 IEEE 17th Workshop on Control and Modeling for Power Electronics (COMPEL)*, pages 1–8, June 2016.

[22] D. Perreault, J. Rivas, Y. Han, and O. Leitermann. Methods and apparatus for resistance compression networks, May 2009. US Patent.

[23] D. Perreault. Transmission-line resistance compression networks and related techniques, September 2014. US Patent.

[24] T. W. Barton, J. M. Gordonson, and D. J. Perreault. Transmission line resistance compression networks and applications to wireless power transfer. *IEEE Journal of Emerging and Selected Topics in Power Electronics*, 3(1):252–260, March 2015.

[25] Anas Al Bastami, Alexander Jurkov, Parker Gould, Mitchell Hsing, Martin Schmidt, Jung-Ik Ha, and David J. Perreault. Dynamic matching system for radio-frequency plasma generation. *IEEE Transactions on Power Electronics*, 33(3):1940–1951, 2018. doi: 10.1109/TPEL.2017.2734678.

[26] D. M. Pozar. *Microwave Engineering*. John Wiley Sons, Inc., 4th edition, 2012.

[27] L. E. Frenzel Jr. *Principles of Electronic Communication Systems*. McGraw-Hill Education, 4th edition, 2016.

[28] M. Brobston, X. Zhu, A. Bui, and G. Hutcheson. Apparatus and method for controlling a tunable matching network in a wireless network. US Patent 8,712,348 B2, 2014.

[29] J. Fu and A. Mortazawi. Improving power amplifier efficiency and linearity using a dynamically controlled tunable matching network. *IEEE Transactions on Microwave Theory and Techniques*, 56(12):3239–3244, 2008.

[30] R. Whatley, T. Ranta, and D. Kelly. Cmos based tunable matching networks for cellular handset applications. In *2011 IEEE MTT-S International Microwave Symposium*, pages 1–4, June 2011.

[31] G. J. J. Winands, A. J. M. Pemen, E. J. M. van Heesch, Z. Liu, and K. Yan. Matching a pulsed power modulator to a corona plasma reactor. In *16th IEEE International Pulsed Power Conference*, volume 1, pages 587–590, June 2007.

[32] Y. Lim, H. Tang, S. Lim, and J. Park. An adaptive impedance-matching network based on a novel capacitor matrix for wireless power transfer. *IEEE Transactions on Power Electronics*, 29(8):4403–4413, August 2014.

[33] H. M. Nemati, C. Fager, U. Gustavsson, R. Jos, and H. Zirath. Design of varactor-based tunable matching networks for dynamic load modulation of high power amplifiers. *IEEE Transactions on Microwave Theory and Techniques*, 57(5):1110–1118, May 2009.

[34] F. Chan Wai Po, E. de Foucauld, D. Morche, P. Vincent, and E. Kerherve. A novel method for synthesizing an automatic matching network and its control unit. *IEEE Transactions on Circuits and Systems I: Regular Papers*, 58(9):2225–2236, September 2011.

[35] S. Banna, A. Agarwal, G. Cunge, M. Darnon, E. Pargon, and O. Joubert. Pulsed high-density plasmas for advanced dry etching processes. *Journal of Vacuum Science & Technology A*, 30(4):040801, 2012.

[36] C.-H. Chang, K.-C. Leou, C.-H. Chen, and C. Lin. Measurements of time resolved rf impedance of a pulsed inductively coupled ar plasma. *Plasma Sources Science and Technology*, 15(3):338–344, apr 2006.

[37] H. Lee, J. Lee, G. Park, Y. Han, Y. Lee, G. Cho, H. Kim, H. Chang, and K. Min. Development of a high-speed impedance measurement system for dual-frequency capacitive-coupled pulsed-plasma. *Review of Scientific Instruments*, 86(8):083505, 2015.

[38] W. Guo and C. A. DeJoseph. Time-resolved current and voltage measurements on a pulsed rf inductively coupled plasma. *Plasma Sources Science and Technology*, 10(1): 43–51, jan 2001.

[39] Y. Nishi and R. Doering, editors. *Handbook of Semiconductor Manufacturing Technology*. CRC Press, Boca Raton, FL, 2nd edition, 2008.

[40] S. K. Kanakasabapathy, L. J. Overzet, V. Midha, and D. Economou. Alternating fluxes of positive and negative ions from an ionion plasma. *Applied Physics Letters*, 78(1): 22–24, 2001.

[41] Alexander S. Jurkov, Aaron Radomski, and David J. Perreault. Tunable matching networks based on phase-switched impedance modulation1. *IEEE Transactions on Power Electronics*, 35(10):10150–10167, 2020. doi: 10.1109/TPEL.2020.2980214.

[42] Anas Al Bastami, Alexander Jurkov, David Otten, Duy T. Nguyen, Aaron Radomski, and David J. Perreault. A 1.5 kw radio-frequency tunable matching network based on phase-switched impedance modulation. *IEEE Open Journal of Power Electronics*, 1: 124–138, 2020. doi: 10.1109/OJPEL.2020.2987782.

[43] Limitation of radiation from industrial, scientific and medical (ism) equipment. Rec. itu-r sm.1056-1, International Telecommunication Union, 2007.

[44] D. Graves. Plasma processing. *IEEE Transactions on Plasma Science*, 22(1):31–42, 1994.

[45] F.-Y. Xiao, Q.-H. Han, and H.-Y. Zhang. The application of advanced pulsed plasma in fin etch loading improvement. In S. U. Engelmann, editor, *Advanced Etch Technology for Nanopatterning VI*, volume 10149, pages 123–126. International Society for Optics and Photonics, SPIE, 2017.

[46] M. Lieberman and A. Lichtenberg. Principles of plasma discharges and materials processing. Wiley-Interscience, Hoboken, N.J., 2005.

[47] I. El-Fayoumi and I. Jones. Measurement of the induced plasma current in a planar coil, low-frequency, rf induction plasma source. *Plasma Sources Science and Technology*, 6 (2):201–211, 1997.

[48] D.J. Perreault and N. Rafa Islam Khandoker. Controllable transformation networks for radio frequency power conversion. World Intellectual Property Organization, Oct 2023. Patent No. WO2023114367A2.

[49] John G. Kassakian, David J. Perreault, George C. Verghese, and Martin F. Schlecht. *Principles of Power Electronics*, chapter 10. Cambridge University Press, 2 edition, 2023. doi: 10.1017/9781009023894.